A universal quantitative method for studying axon guidance and its application to Slit-dependent axon guidance at the developing mouse optic chiasm

Matthew Down

Doctor of Philosophy

Institute for Adaptive and Neural Computation

School of Informatics

University of Edinburgh

2011

Abstract

Healthy pre-natal development of the mammalian visual system requires that retinal ganglion cell (RGC) axons navigate a precise path to their targets in the thalamus and superior colliculus by making a precise series of turns determined by the complex interactions between growth cone and extracellular environment. One important choice point for RGC axons is the crossing of the midline at the optic chiasm, where ipsilateral/contralateral sorting takes place. In this thesis a novel image analysis method using steerable filters for quantifying the gross orientation and turning of axons from a static image (such as from DiI filled axons) is presented. This method was applied to understanding Slit dependent axon guidance at the mouse optic chiasm. It was possible to quantify the differences at the chiasm between the wildtype and various classes of mutants involving heterzygous or homozygous knockout of the Slit1 and the Slit2 genes. Assessment was in terms of the spatial distributions in axon density and axon orientation as derived from DiI labeled RGCs originating from one eye. The animals were assessed at embryonic day 13.5. To my knowledge this is the first quantification of its kind in the field of axon guidance. It was found that there were strong statistical differences from wildtype in both the $Slit1^{-/-};Slit2^{-/-}$ and $Slit1^{+/+};Slit2^{-/-}$ knockouts in terms of both axon density and axon orientation across large extents of the chiasm. In both these knockouts it was found that the changes in axon density were localised to the anterior region of the chiasm, but the changes in axon orientation were spread across almost the entire extent of the chiasm. No other combination of the Slit1 and Slit2 knockouts for which embryos could be generated showed significant differences from wildtype in terms of spatial changes in axon density or axon orientation. No embryos were generated for the $Slit1^{+/-};Slit2^{-/-}$ combination. No changes in the spatial distribution of axon density or axon orientation were found between the $Slit1^{-/-};Slit2^{-/-}$ and $Slit1^{+/+};Slit2^{-/-}$ knockouts, suggesting that in terms of these two quantities, the two phenotypes are indistinguishable. This evidence suggests that the role of Slit2 is more important than the role of Slit1 at the optic chiasm in terms

of axon guidance. In addition, the gradients of mRNA expression of Slit1 and Slit2 were quantified using in situ hybridisation, and these data were used to compare the mRNA gradients with the orientation and turning of axons in both the wildtype and Slit1/Slit2 knockout chiasms. Although this provided a powerful visualisation tool, no simple mathematical relationship was found between the mRNA gradient of Slit1 or Slit2 and the orientation or turning of axons at the optic chiasm. These approaches now provide an important suite of methods for spatial analysis of axon tracts and molecular gradients in axon guidance.

Acknowledgements

Many thanks to Tom Pratt, Dave Price, David Willshaw for their excellent supervision. Chris Conway, Tom Pratt and Kathy Howe for the many hours of help in the laboratory as well as my colleagues in the DTC and DBUG for many useful discussions.

I would also like to thank my girlfriend Louise Seaward and my family for supporting me over the past 3 years.

Declaration

I declare that this thesis was composed by myself, that the work contained herein is my own except where explicitly stated otherwise in the text, and that this work has not been submitted for any other degree or professional qualification except as specified.

(*Matthew Down*)

”Nothing Ventured, Nothing Gained” - Ancient gambling proverb

Table of Contents

Chapter 1

Background

From picking up a mug of tea to enjoying the Grand Prix on a Sunday afternoon, vision is something that greatly enriches our lives. The development of the visual system is a multistage process involving both activity-independent and activity-dependent mechanisms. The activity-independent stage largely coincides with pre-natal development and activity-dependent development with post-natal. This thesis focuses solely on the pre-natal, activity-independent development of the visual system. This is the stage at which the gross wiring of the visual system, unrefined by our experiences of the world around us, is laid down.

My thesis is that mathematical ideas can be used to deepen our understanding of how the nervous system develops, specifically in terms of the wiring of neuronal connections. In this thesis I present a computational method that allows quantification of axons in terms of the direction in which they are travelling and the curvature of their paths. I focus on the model system of the mouse optic chiasm. The development of the optic chiasm is a key choice point in the development of the visual system (Erskine and Herrera (2007)) and has yet to receive extensive mathematical quantification until now. I present an automatic method that allows quantification of both the position and direction of axons in a given image. This now serves as a powerful tool for identifying the precise differences between different phenotypes and the exact location at which

these occur. My hypothesis is that the curvature of axons at the developing mouse optic chiasm is indicative of an underlying guidance force, whatever form this force may specifically take, be it contact induced attraction/repulsion, a diffusible gradient, or morphologically induced changes. I then look at the case of Slit mediated axon guidance and apply the analysis to Slit1 and Slit2 knockout mice. My hypothesis is that these knockouts will exhibit a lack of turning compared to the wildtype mice, and that this can be explained in terms of the mathematically quantified gradients of the guidance molecules Slit1 and Slit2.

In this chapter I expound the background behind my thesis, beginning with the anatomy of the visual pathway, leading through the mechanisms behind axon growth and guidance, a review of the guidance molecules present in the developing mouse visual system and their particular role in shaping its development. I also cover the different existing mathematical models of axon guidance.

1.1 The developing visual pathway

Healthy development of the visual system requires that an ordered connection is formed between the eye and the brain, relaying the information received by the eye to the correct brain areas. It is the role of a single cell type, the retinal ganglion cells (RGC), to bridge the gap between the retina and the thalamus and superior colliculus. Each retinal ganglion cell receives neural activity from thousands of sensory neurons, the photoreceptors, which it in turn relay along the visual pathway (Figure 1.1), for processing in higher brain areas eventually giving visual perception.

During development each RGC is created in the optic fibre layer (OFL) and extends a process guided by its sensory tip, the growth cone (GC), that allows the axon to navigate. In mice neurogenesis of the the first RGCs occurs at embryonic day 10.5 (E10.5) (Robinson and Dreher, 1990). The first stage of the growth cone's journey is to navigate towards the optic disc, where it leaves the retina and enters the optic nerve

at E12 (Dunlop et al., 1997). Here the nerve fibres form a bundle, the outermost fibres originating from the periphery of the retina. The optic nerves from the two eyes meet at the midline on the ventral surface of the developing thalamus, the diencephalon, forming an X-shape known as the optic chiasm. The very first axons reach the optic chiasm at E13 (Dunlop et al., 1997). Some axons cross the midline forming contralateral projections and a lesser number (5% in mice) make a U-turn at the midline and project ipsilaterally. Ipsilaterally projecting RGCs originate exclusively from the ventral temporal crescent of the retina, whereas contralaterally projecting RGCs originate from the entire extent of the retina (Dräger, 1985). Ipsilaterally projecting RGCs are born from E10.5 until E15.5, whereas contralaterally projecting RGCs are born throughout the entire period of RGC genesis (E10.5-E18.5) (Dräger, 1985). After exiting the optic chiasm, RGCs enter the optic tract which continues to follow the surface of the diencephalon, arcing in a dorsal direction until the axons reach their targets in the lateral geniculate nucleus (LGN) and superior colliculus (SC) on the dorsal surface of the diencephalon (Figure 1.1). RGCs first reach these targets at around E14.5 (Robinson and Dreher, 1990), and invade visual centres at E15.5 (Robinson and Dreher, 1990) and RGC neurogenesis ends entirely at E18.5 (Robinson and Dreher, 1990).

1.2 The action of the growth cone in response to molecular gradients

Although I have described the stages of development of the visual pathway, I have not talked about how the growth cone navigates in such a precise manner. In Figure 1.2, we can see the stages through which a growth cone passes in order to interpret and execute the commands of an external signal. In order for a growth cone to navigate it must receive some directional information from the extracellular environment. One such example is the gradient of a guidance cue that can influence the direction in which a growth cone is travelling. Figure 1.2 (1) shows the important parts of a growth cone.

The protrusions radiating from the body of the growth cone are known as the filopodia and the areas in between are the lamellipodia. Receptors are molecules that span the cell membrane and are a cell's means of communicating with the outside world. In the absence of any external input the growth cone will continue to grow in a straight line. As the growth cone moves along, the tubulin polymerises to form microtubules which give structure to the growing axon. However, the growth cone may encounter a gradient of a guidance molecule which will alter the direction in which it is travelling. In Figure 1.2 (2) there are more guidance molecules on the left side of the growth cone than the right. This is a cue for the growth cone to interpret. These molecules bind stochastically to the receptors on the growth cone which typically results in an asymmetric binding pattern due to the underlying asymmetry of the distribution of the guidance molecule (Figure 1.2 (3)). These bound molecules now go on to transduce events that remove F-actin from these filopodia which causes them to retract and the morphology of the growth cone to dramatically change (Figure 1.2 (4)). The growth cone will now continue in a new direction as the result of encountering the gradient of this guidance molecule. In this simplistic scenario I have represented a repulsive guidance molecule. It is easy to see how a molecule that did the opposite and promoted F-actin production in the region of binding could result in an attractive force. In reality, the cast of chemicals involved is far greater in number; but fundamentally the task of interpreting directional cues in the terms of some molecular signal remains the same. I have treated the encounter with a gradient as a discrete event. In reality this whole process is a continuous phenomenon which will be fully described mathematically in the following chapter. In particular I am interested in the behaviour of the growth cone at the optic chiasm. Several detailed studies have looked at this and they shall be reviewed in the next section.

1.3 Time course of growth cone trajectory at the optic chiasm

In the previous section I covered the general principle behind axon navigation, now I shall look at what we know about GC behaviour at our system of choice, the optic chiasm. There is evidence that the GC moves at a constant pace until it reaches the region of the optic chiasm, where GC advance is more intermittent, with a more complex GC morphology at each of these intermittent pauses (Sretavan and Reichardt, 1993; Godement et al., 1994; Mason and Wang, 1997; Mason and Erskine, 2000). In particular, axons projecting ipsilaterally pause for much longer at the midline, where the GC develops a large, complex structure and side branches may occur before turning acutely to project up the ipsilateral optic tract (Sretavan and Reichardt, 1993). These pauses are thought to be in order for the GC to interpret the surrounding environment in a meaningful manner, at key points where it is necessary to integrate the external signal at a given point over an extended period of time. This pausing may also be to do with consolidation of the microtubules in the proximal section of axon. However, the GC continues at roughly the same pace over a scale of 100μm (Mason and Wang, 1997), as can be seen in Figure 1.3 where the position of the GC was recorded at 15min intervals. This information is extremely useful for directing models of axon guidance, and also any information that may be derived from the static axonal morphology regarding the directed route choices the GC must have made at those points, as shall be explained in the next chapter. In addition, notice how there is far more turning of the GC in the region of the optic chiasm than in the optic tract, optic nerve or retina. This gives further impetus to look at quantifying axon turning (again, discussed in the next chapter) at the optic chiasm.

Although we have looked at the mechanism of the GC and its typical behaviour at the midline, the guidance molecules that direct these changes are of great importance in order to understand axon guidance. Many of these guidance cues have already

been identified and are located along the developing visual pathway, in several model animals. In addition to guidance molecules that act directly on the GC to direct orientation, other molecules such as transcription factors pattern the tissue in the correct manner in order for the guidance molecules to be expressed in the correct pattern. As knockouts of these genes also cause defects in the developing visual system, I shall cover some of these key patterning molecules, as well as the key guidance molecules.

1.4 Guidance molecules expressed along the developing visual pathway in mice

The first stage of an RGC axon's journey from the periphery of the retina through the OFL to the optic nerve is thought to be directed by a number of factors to both confine the axons to the OFL and to direct them to the optic disc. A complete picture is not yet apparent, although repulsive guidance molecules Slit1 and Slit2 are both expressed in the retina and knockout of its receptor Robo2 (but not Robo1) result in similar intraretinal guiding errors as those found in Slit mutants (Thompson et al., 2009). These guiding errors are found in the peripheries of the retina in terms of the initial polarity of RGC outgrowth. However, even in these knockouts the axons eventually reach the optic disc and leave the retina suggesting a number of different factors are involved. After reaching the optic disc, healthy axons exit the retina to form the optic nerve, a process which is controlled by the guidance molecule netrin-1 and its receptor DCC (deleted in colorectal carcinoma), which attract axons into the optic nerve. Knockouts of either DCC or netrin-1 result in normal navigation to the optic disc but subsequent failure to exit the retina, resulting in optic nerve hypoplasia (Deiner et al., 1997). In addition, a number of cell adhesion molecules (CAMs) are thought to be involved in the ordered projection of RGC axons to the optic disc. For a complete discussion of intraretinal axon guidance see Bao (2008).

The key molecule confining axons in the optic nerve to a tight bundle is thought

to be Semaphorin (Sema) 5A (Oster et al., 2003). Sema5A protein is expressed in the neuroepithelial cells surrounding retinal axons at both the optic nerve and disc. Sema5A was also found to induce an invariant inhibitory response to axon growth cones in the context of any of the three attractant molecules L1, laminin and netrin-1. Sema5A is the only member of the Semaphorin family expressed in this area. Both the knockout and ectopic injection of Sema5A resulted in severe guidance defects along the optic nerve (Oster et al., 2003).

After guidance along the optic nerve, axons reach the optic chiasm, the point at which axons cross the midline. The chiasm itself forms at an invariant position along the midline. Early in chick embryonic development Sonic Hedgehog (Shh) is expressed along the midline and acts specifically as an inhibitor for RGC axon outgrowth, as shown both in vitro and in vivo (Trousse et al., 2001). Shh can act directly as a guidance molecule collaborating with netrin-1 at the midline to act as a chemoattractant (Charron et al., 2003), but is also a key protein in the hedgehog signalling pathway, which is a key pathway in tissue patterning in early development. Only at the point where axons cross the midline is Shh down-regulated, allowing axons to cross at that point. Shh is thought to repel axons by intra-cellularly decreasing the levels of cAMP in the growth cone through the patched receptor (Trousse et al., 2001). This is in contrast to the retina, where Shh appears to have a dual inhibitory/attractive effect depending on its concentration (Kolpak et al., 2005).

Another gene important for the overall patterning of the developing embryo is the paired-box transcription factor Pax2. During gestation Pax2 is expressed in the mid-hindbrain area and in the developing eye and inner ear. Mutations in this gene cause the brain to develop exencephalically and causes the agenesis of the optic chiasm, resulting in totally ipsilateral projections (Torres et al., 1996). In addition, parts of the pigmented retina enter the optic nerve and the optic fissure fails to close properly resulting in a coloboma. Pax2, however, does not appear to affect other regionally expressed genes such as Wnt-1, En-1 or Pax5. The reason for this agenesis of the

chiasm is thought to be the lack of down-regulation of Shh at the midline. Pax2 and Shh work together to ensure the chiasm forms at an invariant position along the midline. In addition, knocking out the transcription factor FoxG1 also results in RGC misrouting (Pratt et al., 2004). These transcription factors may be acting directly on axons, or indirectly by altering expression of key guidance molecules and receptors (Butler and Tear, 2007).

As well as being expressed in the retinae, Slit1 and Slit2 are expressed in and around the optic chiasm (Erskine et al., 2000). Loss-of-function studies have shown moderate guidance errors in which the optic nerve and tracts appear fairly normal but with large numbers of axons making ectopic midline crossings anterior to the wild-type chiasm (Plump et al., 2002). But this only appears to occur when both Slit1 and Slit2 are knocked out. When only one of the pair is missing the phenotype is not so severe, suggesting Slit1 and Slit2 work in co-operation (Figure 1.4). The slits are interpreted by robo receptors on the growth cone and induce a repellent response in the axon. The slits are thought to implement a fine tuning of axon trajectories around the chiasm, as complete knockout of both genes still results in midline crossing, but the number of aberrant axons increases dramatically. This work is summarised in Figure 1.4.

As well as receptor-ligand pairs of guidance molecules, post-transcriptional factors exist that affect axon guidance, such as the Heparan Sulphate Proteoglycans (HSPG), transmembrane proteins that are found on the growth cone and modulate the effectiveness of receptor-ligand interactions indirectly (Holt and Dickson, 2005). Knocking out HS polymerising enzyme EXT1 reveals midline guidance defects (Inatani et al., 2003), and knocking out sulphate group specific polymerising enzymes Hs6st1 and Hs2st reveal distinct guidance defects at the midline (Pratt et al., 2006; Conway et al., 2011).

I have now covered some of the key factors directing axon growth along the developing visual pathway. However, it is not just the regionalisation of the optic nerves, chiasm and tracts that are important in creating a healthy visual system, axons must

also be sorted at the midline to either project across the midline (contralaterally) or to turn at the midline to project ipsilaterally. Ipsilaterally projecting axons originate exclusively from the ventro-temporal crescent (VTC) whereas contralaterally projecting axons may arise from anywhere in the retina. So the axons must also make the correct exit choice from the chiasm. In addition, two further choices exist: to project ectopically along the contralateral optic nerve or to travel back along the optic nerve towards the eye from which the RGC originated.

The molecular mechanism behind ipsilaterally projecting axons involves ephrinB2/EphB1 signalling. The receptor for ephrinB2, EphB1, is expressed exclusively by ipsilaterally projecting axons. In addition ephrinB2 is expressed in a distinctive line directly along the midline of the chiasm, and EphB1 null mice show significantly fewer ipsilateral projections (Williams et al., 2003). See Figure 1.5.

The molecular mechanisms guiding contralateral projections are less well known. So far only two molecules have been implicated with contralateral projections. The first is the cell adhesion molecule Nr-CAM, which is expressed by axons that project contralaterally and is critical for normal navigation of late-born RGC axons originating from the VTC (Williams et al., 2006). Blocking Nr-CAM increases the ipsilateral projection and reduces neurite outgrowth on chiasm cells in a manner that is dependent upon both the age of the axons and the region from which they originate. In addition Sema3d is expressed along the midline in zebrafish and is thought to guide axons across the midline (Sakai and Halloran, 2006). Sema3d knockdown induced aberrant ipsilateral projections, and time-lapse microscopy showed that overexpression of Sema3d causes growth cone stalling at the midline making it less favourable for RGC's to enter. This suggests that Sema3d must be present in the correct balance to allow contralateral axons to project correctly. On top of this, knockouts of Heparan Sulphate 6 Sulphotransferase 1 (Hs6st1) (Pratt et al., 2006) result in a high number of axons travelling down the opposite optic nerve. A computational model of contralateral axon guidance has shown that Hs6st1 may play a key role in channelling axons

together as they leave the optic chiasm and enter the optic tracts (Down, 2007).

For a full discussion of molecular mechanisms of axon guidance, see Dickson (2002) and Wen and Zheng (2006), and specifically in the visual system: Erskine and Herrera (2007).

In this thesis I am particularly interested in the precise role that Slit1 and Slit2 play in axon guidance at the mouse optic chiasm. In the next section I talk in depth about the biochemical properties of these molecules.

1.5 The Slit-Robo interaction

In the above section I briefly covered the role of Slit1 and Slit2 at the optic chiasm. I shall now go into further detail and describe exactly what is known about the Slit family of ligands and their receptors, the Robo family, both in terms of fundamental molecular properties and also in terms of their function in model organisms.

The molecule Slit was identified in Drosophila, and was found to contain multi-domain leucine-rich repeat (LRR) and be secreted from the cell as a glycoprotein. Slit was initially found to be expressed along the Drosophila midline (Rothberg et al., 1988) and sequenced in Rothberg and Artavanis-Tsakonas (1992). The mammalian homologue is a family of molecules containing three members, Slit1-3. Slits are ligands for the Robo receptors (Kidd et al., 1999) which are members of the immunoglobulin superfamily, a large group of transmembrane proteins. The Slit-Robo interaction is mediated by the second LRR domain of Slit and the two N-terminal Ig domains of Robo. The molecular interaction between the Slit2 active domain and the corresponding domain in Robo1 is described in Morlot et al. (2007) and can be seen in Figure 1.6.

After Slit binds to Robo it is thought that this induces a conformational change in the shape of the cytosolic domain of the protein which then goes on to signal further downstream processes that alter the cytoskeletal structure of the growth cone. It

has been shown that Slit interaction with Robo recruits the SH3-SH2 adaptor protein Dreadlocks (Dock) and the p21-activated serine-threonine kinase (Pak) which in turn increase Rac1 activity (Fan et al., 2003). Rac1 is an important cytoskeletal protein and loss of function of Dock, Pak or Rac partially disrupts Robo repulsion (Fan et al., 2003), although the exact details of these downstream interactions are yet to be fully understood.

In addition to being implicated with several areas of axon guidance in the CNS Dickson (2002), the Slit-Robo interaction has been found to be important in the development of the lungs, kidney, several areas of cell migration as well as the study of brain tumours (Ypsilanti et al., 2010).

During development Robo1 and Robo2 are expressed in and around the optic chiasm, as well as being expressed in the developing retina (Erskine et al., 2000). Unlike invertebrates such as *Drosophila* (Seeger et al., 1993), Robo is present in the navigating growth cones prior to midline crossing, suggesting quite a different role for the Robo receptor in the developing mammallian brain.

1.6 Axon guidance in vitro

I have described how axons navigate in vivo, taking particular attention to describe the model system of choice: the optic chiasm. Another important area of research is directed to the artificial manipulation of axons outside of the living organism, in vitro. The purpose of studying axon navigation in vitro is to investigate fundamental properties of growth cone function in an isolated, strictly controlled environment. I shall now give a brief overview of the techniques used in this area of research.

The most common in vitro assay is the pipette assay, that is used to show if a candidate molecule acts as a guidance factor, first used by Ming et al. (1999). The pipette assay consists of purifying the protein of the candidate molecule and injecting it into a Petri dish containing cultured axons, at an angle of 45° to the direction of a

given axon's growth. The axon may then (a) remain unaffected, (b) turn away from the pipette or (c) turn towards the pipette. These three scenarios represent a neutral cue, a repulsive cue and and an attractive cue respectively. A quantitative analysis of the exact form of gradient created by this kind of assay was determined by Pujic et al. (2008). In addition to this technique a more refined approach is presented in Rosoff et al. (2004), that uses a machine to print a pattern of the chosen substrate onto a collagen gel, allowing for much more precise patterning. This technique has been put to great use to show that one possible mechanism for allowing the growth cone to interpret extracellular cues is through modulating its growth rate depending on if it's heading up or heading down the gradient (Mortimer et al., 2010). Another popular in vitro assay is to cover latex beads with a guidance factor and determine the respective number of axons that contact these beads as opposed to control, uncoated beads. Yet another approach is to transfect Cos7 cells with your ligand of choice, and perform a similar choice assay as before. This method was used by Pratt et al. (2006) to successfully show that Hs6st1 is required for Slit2 avoidance by RGC axons in vitro.

1.7 Models of axon guidance

In this section I review the number of different attempts to provide insight into axon guidance using mathematical and computational modelling.

One of the first papers to look closely at the mathematical behaviour of the growth cone was Buettner (1995), who developed a phenomenological model of filopodia dynamics, based on time lapse images of the growth cone. These tracings are shown in Figure 1.7. From these images it was possible to estimate the mean initiation rate of filopodia, and the time for the filopodia to reach maximum length. These data were found to follow a Poisson distribution. She also proved the equality of the rates of filopodial extension and retraction as well as the circularly uniform distribution of filopodial initiation around the main body of the growth cone. This demonstrates an

interesting way of modelling a system, by initially quantifying a phenomena, looking for structure in the data and then developing a phenomenological model from that. The most impressive thing about this work is that it doesn not rely on any assumptions for the validity of the findings, yet manages to make insights into many aspects of filopodial dynamics.

Another early approach attempting to understand growth cone behaviour was to create a model in terms of forces applied by the growth cone on the proximal section of neurite, made by Van Veen and Van Pelt (1994). A number of differential equations were used to model the finite rate at which microtubules can be polymerised from tubulin, as a means of limiting growth cone motility. Another similar, but more abstract model, also added equations to look at branching of the growth cone to form tree-like neurons (Guo-Hua Li and Wang, 1995).

Goodhill (1997) developed a theory of signal transduction from gradients of guidance cue. By looking at the mathematical form of the 2D gradient formed from a point source of diffusible molecule and comparing this gradient with the size of the growth cone, Goodhill (1997) showed the minimum signal to noise ratio required for a typical GC to detect. These theoretical calculations greatly complement the in vitro work that has been done using point sources of guidance cue. However, measuring the gradients of guidance molecules in vivo accurately enough to test these predictions has so far proved too difficult and the description of gradients in vivo as typically being exponential is not supported by experimental evidence.

Inspired by work done in chemotaxis of leukocytes (Berg and Purcell, 1977), small bacteria that can detect and ”swim” up a molecular gradient, Goodhill and Urbach (1999) used a similar mathematical formalisation to derive an equivalent model for the growth cone.

A more complex model of the growth cone is detailed in Goodhill et al. (2004). They present a reductionist model of the growth cone, simulating each receptor explicitly in terms of its position on the growth cone and its bound/unbound state, which

demonstrated interesting properties of growth cone behaviour such as stochastic growth, and desensitisation of the growth cone due to bound receptor saturation. These ideas were then abstracted into a Bayesian model of growth cone behaviour (Mortimer et al., 2009).

More recently Krottje and van Ooyen (2007) developed an impressive simulation framework for precisely modelling the trajectories of the growth cone, including many features such as a non-uniform mesh for modelling the positions of guidance molecules, and several algorithms optimised for efficient simulation of molecular diffusion.

1.8 Applications of models to data

At present there still appears to be a large weighting towards theoretical publications of axon guidance over experimental papers that use these models. In addition, theoretical papers tend not to directly include axon guidance data in their models. An exception is the model due to Buettner (1995), a pioneering phenomenological model of GC behaviour and Goodhill (2003), which draws together the large body of work looking at axon guidance at the midline of Drosophila in the absence of the different robo receptors. In this he provides a set of constraints that must be satisfied by models in order to avoid contradicting biological data. This study looked at the distance of the various axon tracts from the midline in response to knockouts of slits and robos, in one dimension only.

Like any area of science it is imperative to continue to build on previous successes. Although there have been many interesting computational models of axon guidance, the combination of experimental data and model has so far proved less successful. One of the major difficulties is in quantifying axon guidance data for comparison with modelling work. This is due to the difficulties in quantifying histological images which are often highly complex and are computationally difficult to abstract features from.

Also, the scope for directly combining experimental data and theoretical analysis into a phenomenological model such as seen in Buettner (1995) is great, and in this thesis I aim to continue this emerging area of axon guidance research.

1.9 Chapter summary

In this chapter I have looked at what we already know about axon guidance in general, the roles of different molecules along the developing visual pathway, and in particular why the optic chiasm is interesting to look at. I explain a need for improved computational techniques to analyse histological data accurately and automatically. I have also covered the various computational approaches that have already greatly contributed to the field. In the next section I will show how my approach will attempt to fit in and complement the current literature.

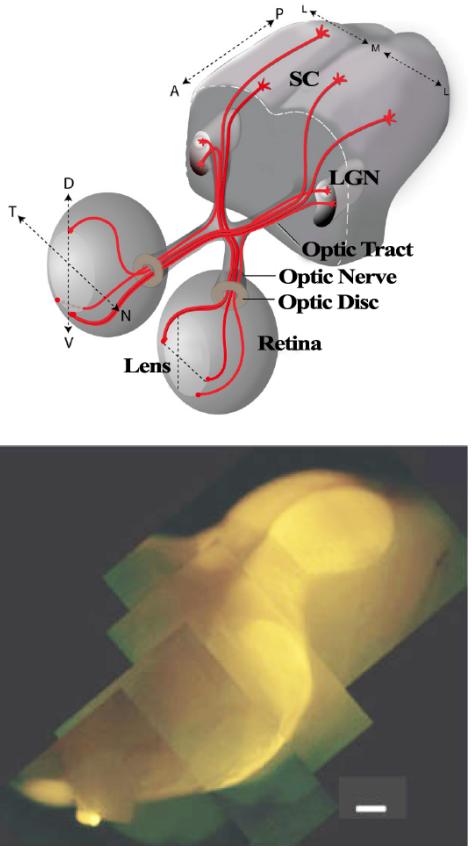

Figure 1.1: (a) A schematic of the mouse visual pathway, similar scale and perspective to (b). D (dorsal), V (ventral), N (nasal), T (temporal), A (anterior), P (posterior), M (medial), L (lateral), SC (Superior Colliculus), LGN (Lateral Geniculate Nucleus). (Erskine and Herrera (2007)). (b) A wholemount preparation of the mouse retinofugal pathway visualised by injecting DiI into both eyes and removing the cortex and eyes. Scale bar = 1mm (Plas et al., 2005).

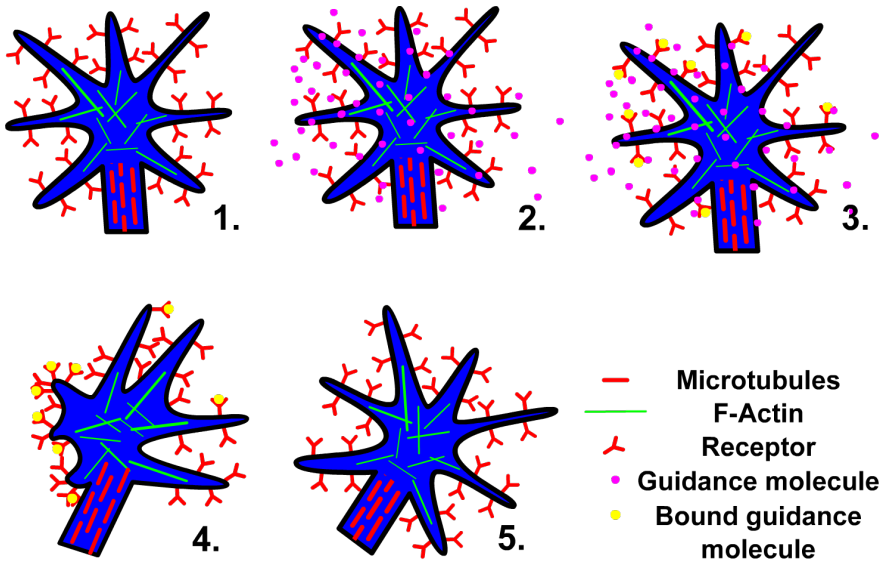

Figure 1.2: The stages of molecular gradient induced repulsive growth cone turning. 1) The growth cone in the absence of any external cues will continue in a straight line. Tubulin gets polymerised to form microtubules, giving the axon its structure. 2) The growth cone encounters a gradient of repulsive guidance molecules. 3) These molecules bind stochastically to the receptors asymmetrically due to the molecular concentration being higher on one side. 4) This results in retraction of filopodia from one side of the growth cone. 5) The growth cone now travels in a new direction

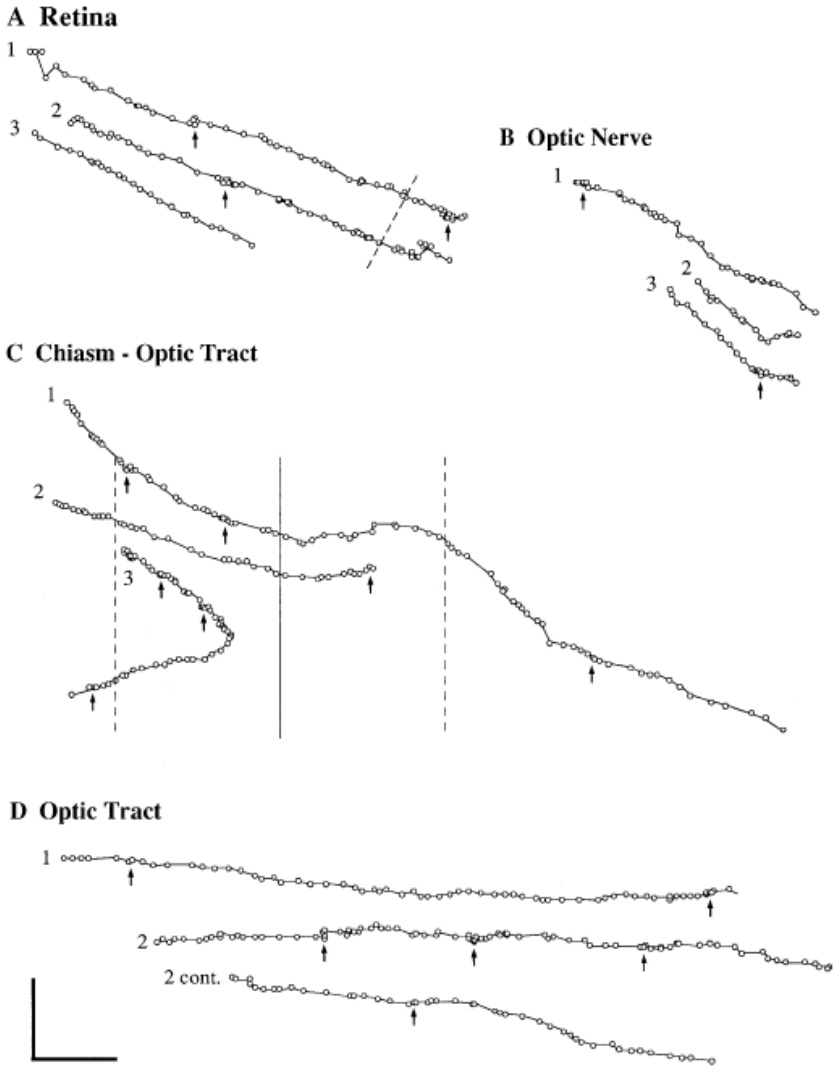

Figure 1.3: This shows how the position of the GC changes over time (moving from left to right) in a whole-mount time lapse video recording from the optic chiasm. Dashed lines are indicative of the edges of the chiasm. Solid line is the midline. The circles represent the position of the GC at 15 min intervals, arrows highlight pauses in the movement of the GC. Scale bars 100 μm. Mason and Wang (1997)

.

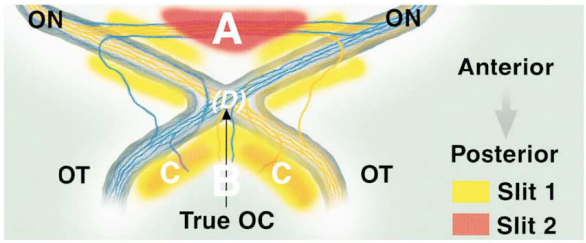

Genetic Background	A Ectopic Chiasm	B Anterior-Posterior Midline Wandering	C Ventrolateral Wandering	D Ventral-Dorsal Midline Wandering
Slit1 -/-	-	+	-	-
Slit2 -/-	-	-	-	-
Slit1 -/- ; Slit2 +/-	-	+	-	-
Slit1 +/- ; Slit2 -/-	++	NA	NA	NA
Slit1 -/- ; Slit2-/-	++++	+	+	+

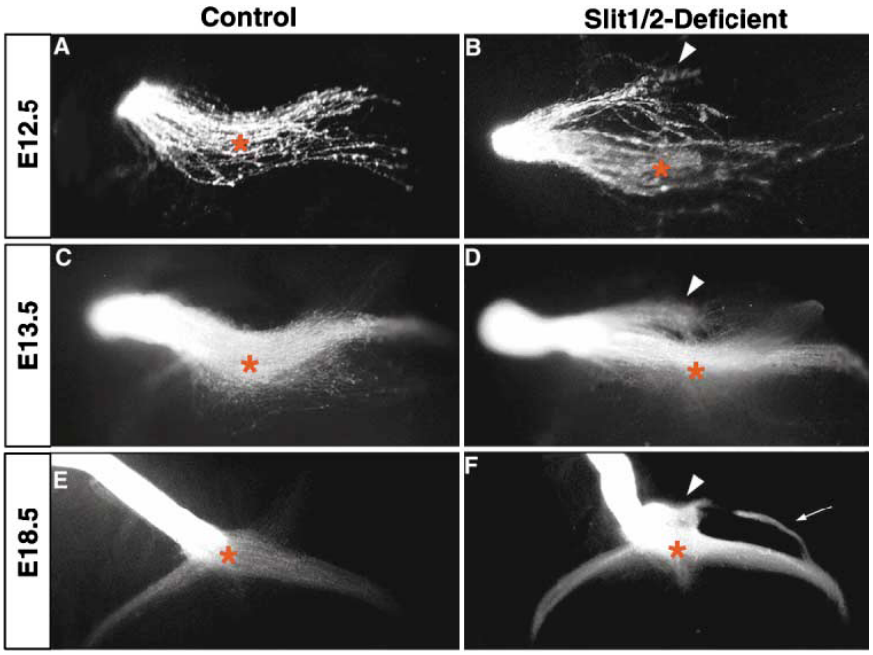

Figure 1.4: (a) A schematic of the expression of Slit1 and Slit2, and a summary of the knockout phenotypes of these molecules (Plump et al., 2002). (b) DiI images of the optic chiasm after homozygous knockout of both Slit1 and Slit2 at ages E12.5, E13.5 and E18.5 respectively (right column), compared with wildtype (left column). Arrows indicate formation of ectopic chiasm, asterix indicates position of wildtype chiasm (Plump et al., 2002).

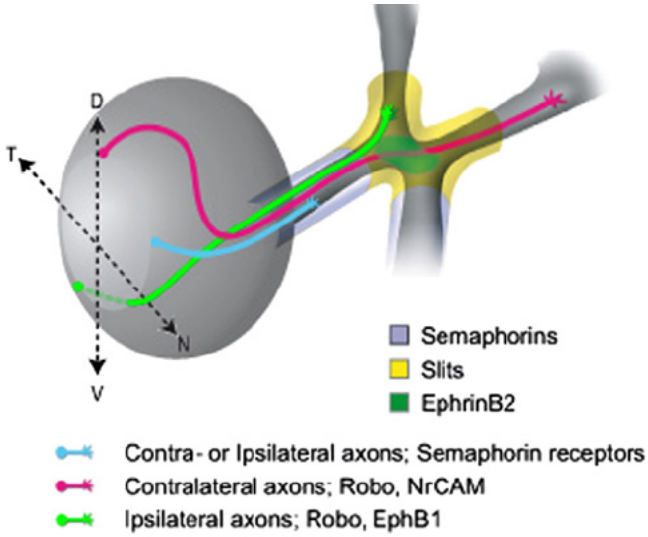

Figure 1.5: Schematic diagram of key guidance molecules expressed in and around the chiasm, as well as the axon trajectories. (Erskine and Herrera (2007))

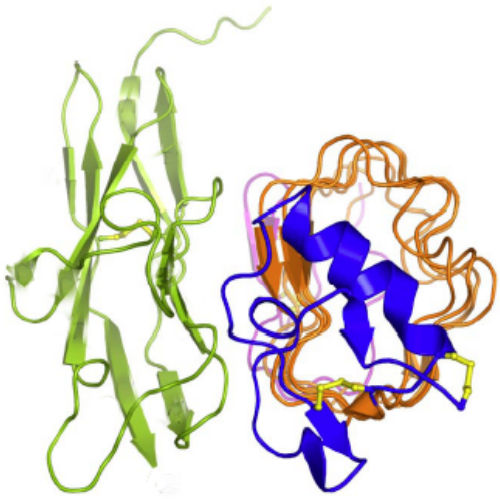

Figure 1.6: The binding of the Robo1 Ig1 domain (green) to the Slit2 D2 N- and C-terminal caps (purple and blue respectively) (Morlot et al. (2007)).

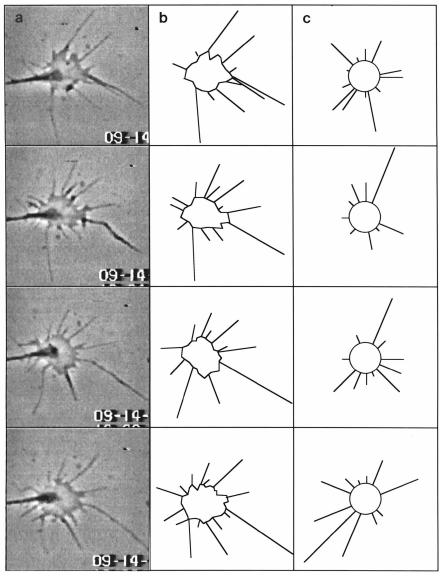

Figure 1.7: Modelling the dynamics of filopodial extension and retraction. 1st column: Time lapse video frames of a rat superior cervical ganglion growth cone (GC). 2nd Column: tracing of the lamellipodial region and filopodia. 3rd Column: A simulated GC using the same filopodial dynamics as measured from the GC on the left (Buettner, 1995).

Chapter 2

A phenomenological model of axon trajectories

In this chapter I talk about my attempts to look at how axon guidance can be understood mathematically, and how the current approaches may be supplemented with a more phenomenological approach. This chapter is in parts somewhat conceptual, but the hope is that this chapter provides interesting discussion, even if it is not of itself a complete theory.

2.1 Axon guidance phenomena

The initial thinking motivating this thesis was that instead of focusing on reductionist models, it might be possible instead to observe the trajectories taken by the growth cone and derive some kind of statistical model based on the nature of their movement. Such a model would be analogous to the phenomenological model of filopodial dynamics developed by Buettner (1995), but instead of statistically modelling the phenomena of filopodial dynamics, the velocity of the growth cone (GC) would be statistically modelled. These properties are an abstraction of a much richer set of more fundamental phenomena (various molecular pathways etc.), yet the final trajectory of the axon is

the principle goal of GC navigation. The hope is that as well as providing additional fundamental insight into GC behaviour, it would also allow insight into the relationship between GC dynamics (in terms of position and direction) and the environment that directs these dynamics (such as the gradient of a guidance cue etc.) and build a statistical model of the relationship between the two.

This model could possibly be derived from time-lapse microscopy which would give the exact position and direction of the growth cone at any point. Alternatively it might be more practical to look at the form of the section of axon proximal to the GC in a static image, from which it would be possible to infer the previous position and orientation of the GC by assuming that the section of axon proximal to the GC is representative of the history of the recent behaviour of the GC. Alternatively, it might be found that the axons are laid down in a bundle and instead of being able to trace the trajectory of a single axon, it would only be possible to measure the overall mean direction that the axons are travelling in. In each of these three cases we have a wealth of information regarding the phenomena of laying down an axon trajectory and it ought to be possible to build a statistical model from these data.

This approach is intended to have two goals. The first is to allow a means to quantify the behaviour of the growth cone, even though we may only be observing a single snapshot in time. The second is as a means of comparison between axon trajectories of different genotypes in order to reveal novel phenotypes and infer some function for that gene.

There's nothing particularly revolutionary about attempting to gain insight into the nature of axon guidance by studying the form of the axon trajectory. What I aim to do differently here is to look at how these trajectories can be understood and related to one another mathematically. In the next few sections I talk about how different experimental approaches in axon guidance can be used to form such a phenomenological model.

2.1.1 Growth cone time-lapse data

I begin by defining some of the mathematical notation I shall use to describe the course of a GC over time. The benefit of going to the length of reviewing the way a curve can be represented in space is that I can then take advantage of standard mathematics describing abstract properties of such curves, allowing me to focus on important properties of the trajectory that are of scientific interest, such as the variability in direction over a short portion of the axon, or the amount of turning the growth cone might be making at a certain point.

First I present a standard equation that is used to represent curves in space. This curve represents the position of a GC over time:

$$\mathbf{r}(t) = x(t)\mathbf{i} + y(t)\mathbf{j} + z(t)\mathbf{k} \tag{2.1}$$

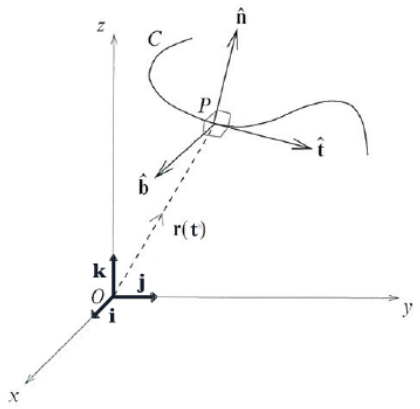

Figure 2.1: Mathematical representation of a curve in 3-dimensions. $\hat{\mathbf{t}}$ is the direction of the curve at point P, $\hat{\mathbf{n}}$ the direction of the curvature, and $\hat{\mathbf{b}}$ is the direction of the torsion.

Here, $\mathbf{r}(t)$ represent the position of the growth cone, which changes according to the variable, t (time). As this equation represents the position of the GC in 3-D, three functions ($x(t)$, $y(t)$ and $z(t)$) are needed in order to describe its path in space. These three functions each describe the position of the GC with respect to the three independent unit-vectors (vectors of length 1) $\mathbf{i}$, $\mathbf{j}$ and $\mathbf{k}$, which are parallel to the x-axis, y-axis and z-axis respectively (shown in Figure 2.1). Ideally it would be possible

to find the functional form of the trajectories as this allows much deeper mathematical analysis, by allowing the use of standard analytical techniques. For example a circular trajectory would be described by:

$$x(t) = \sin(t) \tag{2.2}$$

$$y(t) = \cos(t) \tag{2.3}$$

$$z(t) = 0 \tag{2.4}$$

However, such simple functions do not normally describe the path of a GC accurately and instead some kind of approximation is needed in order to find some functions that do represent the path of a GC. For example, from time-lapse microscopy, a discrete set of observations of the position of the GC would be obtained (as shown in two dimensions in e.g. Mason and Wang (1997)). For n observations in time, the following set would result:

$$\{\{t_1, x_1, y_1\}, ..., \{t_n, x_n, y_n\}\} \tag{2.5}$$

These points map out a curve, which could be connected using straight line segments as was done in the original paper (See Figure 1.3), but in order to accurately represent the trajectory of the GC it may be useful to represent these points using a continuous function. Hermite interpolation is an alternative method which estimates the curve connecting two points, whilst ensuring these segments are joined together smoothly. That is to say that the functions themselves are continuous as is the gradient along the length of the function (only the first of these two criteria is true for straight line interpolation). If straight line interpolation is used then properties such as the amount of turning (curvature) at any point would be misestimated.

Although we may know the position of the GC at any point in time, an estimate of the direction the GC is heading needs to be determined from the knowledge of its position alone (I'm assuming here that we are not explicitly observing the morphology

of the GC itself, just tracking its position). This is not as simple as it sounds as the GC may stay in approximately the same spot, yet be searching out a number of directions. For the purpose of this formalisation I shall take the direction of the GC to be at a tangent to the curve $\mathbf{r}$. I shall denote the GC direction by: $\hat{\mathbf{t}}$ (see Figure 2.1), defined as:

$$\hat{\mathbf{t}} = \frac{d\mathbf{r}}{dt} \tag{2.6}$$

This is simply the instantaneously direction of the GC, which has a direction and a magnitude, but for the purposes of this we'll consider just the direction the GC is travelling in. However, what we are particularly interested in quantifying is the curvature of the trajectory at any given point. This indicates GC turning which is the result of some external guiding force imparting route finding information onto the GC. The magnitude of the curvature is defined as the absolute rate of change in direction:

$$\kappa = \left| \frac{d\hat{\mathbf{t}}}{dt} \right| = \left| \frac{d^2\hat{\mathbf{r}}}{dt^2} \right| \tag{2.7}$$

The higher the value of κ, the greater the magnitude of the curvature at that point along the trajectory, i.e. the tighter the turn being made by the GC. The inverse of the curvature is the radius of curvature, defined as: $\rho = 1/\kappa$, which is the size of the turning circle being made at that point by the GC. Like the velocity of the GC, the curvature ($\mathbf{g}$) also has a direction, which is perpendicular to the velocity (i.e. proportional to the unit vector $\hat{\mathbf{n}}$, shown in Figure 2.1), and is defined as:

$$\mathbf{g} = \kappa\hat{\mathbf{n}} = \frac{d\hat{\mathbf{t}}}{dt} \tag{2.8}$$

In three dimensions, $\kappa\hat{\mathbf{n}}$ will always be in the same plane as the GC is currently moving in. An intuitive way of thinking of $\mathbf{g}$ is as of the direction in which the GC is turning and the bigger $\mathbf{g}$ is, the faster the GC is turning in that direction.

A third vector now exists ($\hat{\mathbf{b}}$ in Figure 2.1) which is perpendicular to both the velocity and curvature, the rate of change of this is known as the torsion, with magnitude

τ and direction $\hat{\mathbf{n}}$ (i.e. parallel to the curvature), defined as:

$$\frac{d\hat{\mathbf{b}}}{dt} = \tau\hat{\mathbf{n}} \tag{2.9}$$

The magnitude of the torsion of a curve at any point is an indication of the degree to which the trajectory at that point is leaving the plane it is currently in. An axon whose trajectory remains within a single plane would have a τ of zero, whereas a corkscrewing axon trajectory would have a higher τ. The biological significance of this value is less clear than for the case of the curvature, but it may be useful for distinguishing between mutant phenotypes.

2.1.2 Static image of growth cone and axon

An alternative to measuring the position of the GC over time using time-lapse microscopy is to take a static image of the GC and proximal section of axon and assume that this section of axon represents the history of the GC's position and direction using a method similar to the one above. Instead, the equations for the position of the GC would not be parameterised with the variable of time (t), as above, but of length (l), measured along the axon (as shown in Figure 2.2):

$$\mathbf{r}(l) = x(l)\mathbf{i} + y(l)\mathbf{j} + z(l)\mathbf{k} \tag{2.10}$$

The other equations would have the exact analogies as this, except that t would be replaced with l. Typically measuring the 3D form of an axon would be achieved using a fluorescent dye and scanning confocal microscopy. The axon tracing would again give a discrete set of points, which could be used to fit to a curve, perhaps using Hermite interpolation again. Here I define the tip of axon to be at position $\mathbf{r}(L)$ and the axon proximal to this point would be defined to be at position $\mathbf{r}(L-l)$. As this is a destructive snapshot (as opposed to a number of continuous observations), the length of axon for $l > L$ will remain unknown. For sections of axon close to the GC, it is

a reasonable assumption to say that this represents the history of the direction of the GC, but for sections of axon laid down a period of time ago, this assumption may be compromised. This is due to the fact that tissue growth may distort the axon, and give a false impression of what the GC was doing at that point. Additionally, the GC sometimes searches several directions before deciding on an eventual direction to travel in, so this section of axon immediately proximal to the GC may not be indicative of the "decision" of the direction of travel GC has chosen, merely indicative of an intermediate phase. However, the relation between the path the GC took and the eventual morphology of a neuron is an important consideration, although beyond the scope of what we are attempting here, but a series of destructive observations may at least shed some light onto this phenomena.

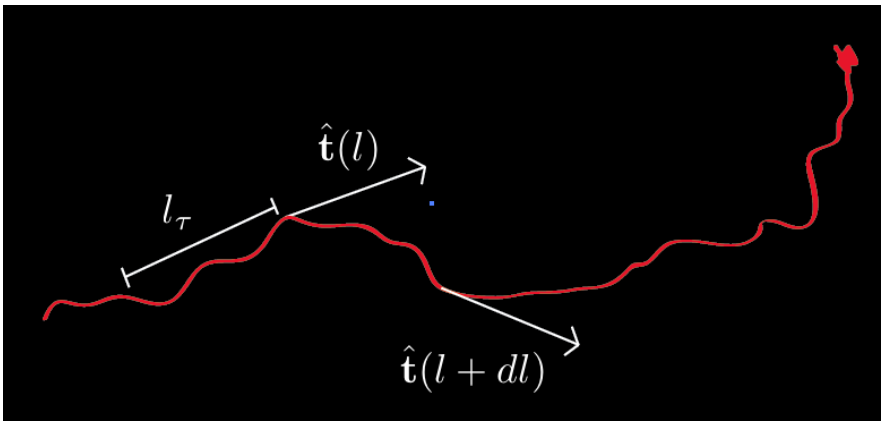

Figure 2.2: The proximal section of axon from the GC represents the history of the GC direction. By measuring the tangent $\hat{\mathbf{t}}$ to the axon we reveal the GC direction at that point. However, due to the stochastic nature of axon navigation it might be necessary to integrate this value over a distance l_τ

2.1.3 Smoothing out the noise along a growing length of axon

Due to the stochastic manner in which the GC appears to move over short distances, and the subsequent twists in the proximal section of axon laid down behind it, in order to gain a meaningful estimate of the direction of growth at a single point, I should

take the average direction along a length of the axon proximal to the exact point at observation. The reason to do this is two-fold. The first is to average out the noise, the second is the causality of signal transduction. The GC can only make directed route choices based on information received prior to the present. Speaking in spatial terms, this is the area the GC passed through prior to its current position. The simple linear average, for the continuous form of the axon trajectory, works out as an integral:

$$< \hat{\mathbf{t}}(l_0) >= \frac{\int_{l_0-l_\tau}^{l_0} \hat{\mathbf{t}}(l).\mathrm{d}l}{l_\tau} \tag{2.11}$$

$< \hat{\mathbf{t}}(l_0) >$ is defined as the average direction of the GC at position l_0, the position the average direction is being assessed, and l_τ is the proximal length over which the averaging takes place. However, I postulate that a non-linear averaging may be more appropriate. This is because (i) signal transduction does not have an immediate effect and (ii) its effects only last for a limited time (Figure 2.3).

$$f(l) = le^{-l/k} \tag{2.12}$$

Where k is the natural length of the integration distance, and l is the distance proximal to the GC. Notice equation 2.12 tends to zero both as $l \to 0$ and $l \to \infty$, avoiding the discontinuities of the linear averaging method. In order to estimate the weighted average of the position along the growth cone at a point l_0, we need to calculate:

$$< \hat{\mathbf{t}}(l_0) >= \frac{\int_0^{l_0} f(l-l_0)\hat{\mathbf{t}}(l)\mathrm{d}l}{\int_0^{l_0} f(l).\mathrm{d}l} \tag{2.13}$$

Typically one may expect k to be a function of the dissociation constant of the ligand-receptor pair in question. A guidance molecule with a large dissociation constant may be attached to the GC for a long period of time and one with a small dissociation constant would detach almost as soon as it has bound the receptor. Another factor would be the speed of the internal signal transduction. If this were to be a lengthy series of steps then the GC would be reacting to an external signal some minutes after it

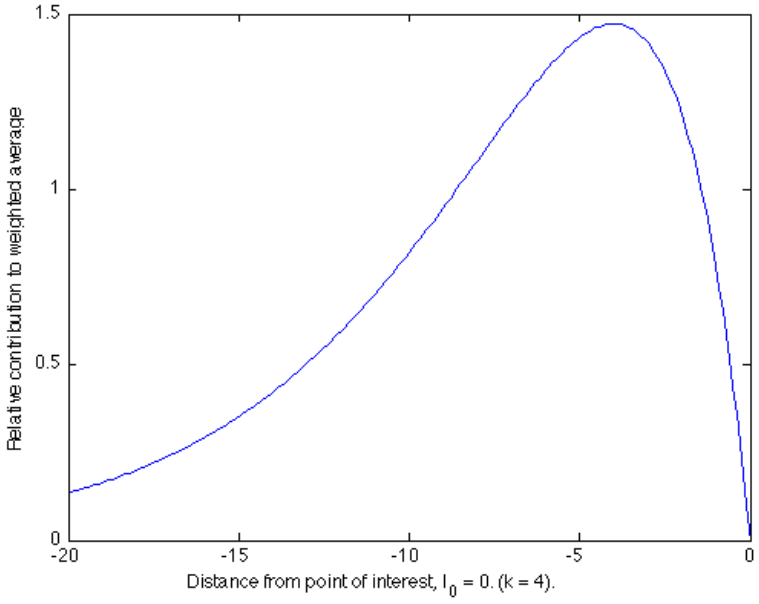

Figure 2.3: This plot represent a plausible weighting for the integration of an external signal over the proximal section of axon, the GC is at l = 0. The initial rise from $l = 0$ to $l = -5$ is due to the causality of signal transduction, and the subsequent fall off due to the ”memory” of the GC depleting and ”forgetting” what the gradient was a long time ago.

was detected by the receptors. However, cell signalling can take place very rapidly, but perhaps slow signal transduction may be beneficial for averaging external noise. Both these factor would affect the integration distance, k, of the GC.

In both the cases of the time-lapse microscopy and the static "snapshot" images, I have adapted the standard mathematical formalisation for analysing these data in a phenomenological manner. These simple quantitative methods now demonstrate the kind of approach that could allow greater insight into the response of the GC to the surrounding environment. Once the behaviour of the GC has been understood in terms of these quantities such as curvature, it is possible to relate this quantification to the mechanisms thought to be directing the changes in direction. I shall discuss this in the next section.

2.1.4 Relating the curvature of the growth cone trajectory to the gradient of a guidance molecule

If we suppose initially that this external cue comes in the form of a molecular gradient, we could presume that the turning of the growth cone is a result of a causal relation between the detection of such a cue and the act of turning. Suppose the gradient is derived from a function telling us the amount of guidance molecule at all relevant points in 3D (denoted by $\psi(x,y,z)$), which would be determined histologically. The gradient in vector notation is written as $\nabla\psi$, which is a vector field. At each point in 3D there will be an arrow indicating the direction and magnitude of steepest ascent (or descent) of the gradient of the molecule in question.

In the previous section the direction of the growth cone was taken to be a weighted average over the proximal section of axon. In the same way, the input it receives from the gradient should also be calculated as a weighted sum over the same area.

In the simplest scenario the component of the gradient $\nabla\psi$ perpendicular to the direction of travel (In vector notation this component is written as $(\nabla\psi).\hat{\mathbf{n}}$) is proportional to the curvature of the axon (Figure 2.4). This proportionality rule can be written

as:

$$\mathbf{g} \propto \int_0^{l_0} (\nabla\psi).\hat{\mathbf{n}}\mathrm{d}l \tag{2.14}$$

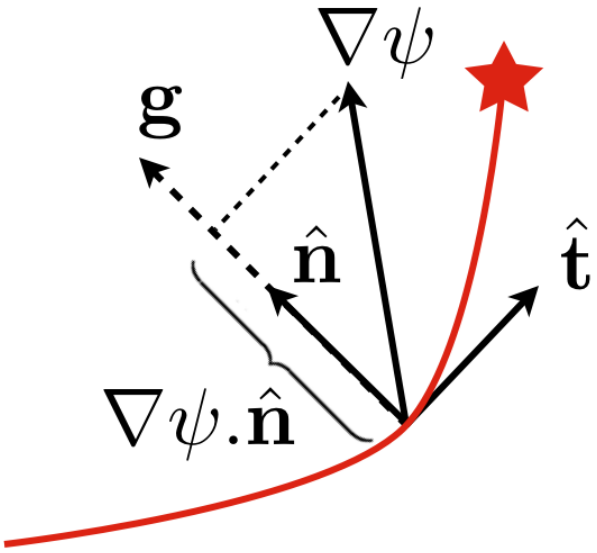

Figure 2.4: This schematic diagram shows the relationship between the relevant vectors on the axon. $\hat{\mathbf{t}}$ is the direction of curve, $\hat{\mathbf{n}}$ is the unit vector perpendicular to the direction, $\mathbf{g}$ is the curvature, and $\nabla\psi$

Again, I have integrated over a distance l_0 to account for the causality of signal transduction. In reality the GC may be subject to a number (n) of guidance molecules which for now we will define as being $\{\psi_1, ..., \psi_n\}$, in which case the response of the GC may be the integration of many of these cues:

$$\mathbf{g} = \int_0^{l_0} \sum_{i=0}^{n} [\alpha_i(\nabla\psi_i).\hat{\mathbf{n}}]\mathrm{d}l \tag{2.15}$$

The constants α_i denote the strength of each guidance molecule. Although, α_i may be a function of the internal state of the GC, which could be included in the model at a later date.

In the next section I shall look at the equivalent formalisation for the case of a bundle of axons. The only difference here is that instead of each axon being a fully

traceable object, only the local orientation can be determined. This means that both the gradient and the axon orientations constitute an extended vector field.

2.1.5 Derived vector field axon tract modelling

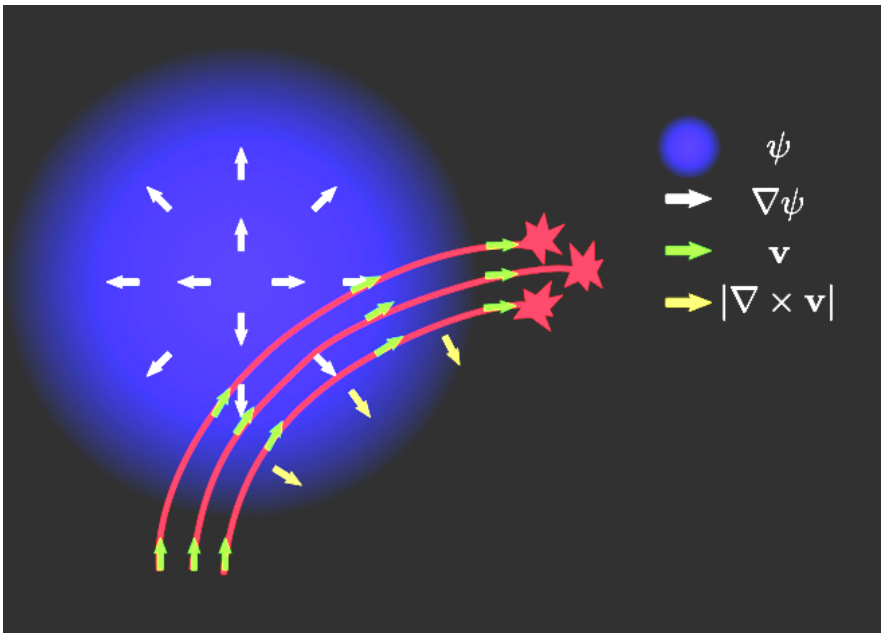

Figure 2.5: This image represents the different vector fields that can be measured in the developing embryo. Blue indicates the expression level of a molecular guidance cue, the white arrows its gradient. Green is the orientation of the axons are going and yellow their net curvature

After developing an algorithm that attempted to automatically trace axons, it was found that such explicit tracing was impossible for DiI filled axons, in many cases due to the overlapping trajectories. However, it was possible to determine the local orientation of axons within the bundle. This means that the mathematical formalisation has to be altered to accommodate this.

Figure 2.5 shows the schematic relationship between the gradient of a guidance cue and the net trajectory of axons passing through the region. A repulsive cue is shown, with the axons curving away from the region as a result. Now that I am dealing with a vector field, not fully traceable axons, the net curvature can still be measured. This

quantity is known as the curl of a vector field and is represented by $|\nabla \times \mathbf{v}|$, where $\mathbf{v}$ is the vector field of axon orientations. In axon guidance the curl represents the amount of turning at a given point, similar to the curvature in the previous section. Again, I use $\hat{\mathbf{n}}$ to represent the unit vector perpendicular to the direction of travel.

As in the previous section, I postulate that the curvature of the axons is proportional to the component of the gradient perpendicular to the axon direction. This leads me to formulate a simple equation relating the trajectories of the axons with the gradient:

$$|\nabla \times \mathbf{v}| \propto \nabla\psi.\hat{\mathbf{n}} \tag{2.16}$$

And equally for several guidance cues:

$$C = |\nabla \times \mathbf{v}|\hat{\mathbf{n}} = \sum_{i=0}^{n} \alpha_i(\nabla\psi_i.\hat{\mathbf{n}})\hat{\mathbf{n}} \tag{2.17}$$

This is the vector field version of equation 2.15. What is typically observed in vivo is the change in curvature when one particular guidance molecule is knocked out:

$$C_{+/+} - C_{-/-} = \alpha(\nabla\psi.\hat{\mathbf{n}})\hat{\mathbf{n}} \tag{2.18}$$

where α is the constant of proportionality for that guidance cue. Note that these equations only apply for axon tracts where axons tend to move in one reasonably consistent bunch. However, this is typically not a problem as this is often what is seen during development. In particular, the optic chiasm is composed of a number of axons travelling in roughly the same direction.

The advantage of formulating the equations in this form is that we now only need to measure the gross flow of axons across the region of interest rather than to explicitly trace each individual axon. In the next chapter I describe how this can be achieved automatically.

2.2 Chapter Summary

In this chapter we have seen how it may be possible to use time-lapse data and traces of individual axons to infer some properties relating to the behaviour of the GC. I then postulated how the GC may integrate the extracellular signal over some length prior to a given point, and discuss possible forms of the equations for this spatial integration. I then showed how to calculate the curvature of the axon trajectory, which is a key (and currently overlooked) indication of the turning behaviour of the GC in response to the extracellular environment. The curvature was postulated to be the result of a linear sum of guidance cues. The same formalisation was developed for both individually traced axons and bundles of axons.

The overall intention of this chapter was to describe a new way of looking at quantifying GC behaviour, and interpreting the axonal curves in a meaningful mathematical manner. The manner in which these features of the trajectory relate to corresponding factors such as the gradient is unknown, although the simplest form this relationship may take has been described mathematically too. This relationship is investigated in the following chapters. It is hoped that this new approach can reveal the full richness of axon guidance data.

Chapter 3

Axon tracing, quantification and analysis

In this chapter I cover the process of obtaining the data required, with a view to interpreting the results based on the mathematical formulations in the previous chapter. The key quantity to measure is the snapshot trajectory of the growing axon (in the mathematical formalisation described in the previous section). Standard protocols were followed as much as possible in order to minimise the amount of trial and error in the lab, and focus on the novel mathematical/computational side of the project. This chapter covers the extensive attempts to automatically trace axons computationally as both individual fibres and as a population, in a manner that gives insight into mechanisms of axon guidance.

3.1 Tracing axons using DiI

Mouse embryos 13.5 embryonic days old (E13.5) were used for the DiI experiments, following the standard protocol to label the visual pathway (see Appendix B). This age was chosen as typically it was found to be the stage at which the first axons crossed the midline (Dunlop et al., 1997), and therefore for the purpose of the computational

analysis justifying the assumptions made in the previous section regarding the direction of the axon representing the history of the GC direction. Figure 3.1 is a sample image of axons crossing the midline.

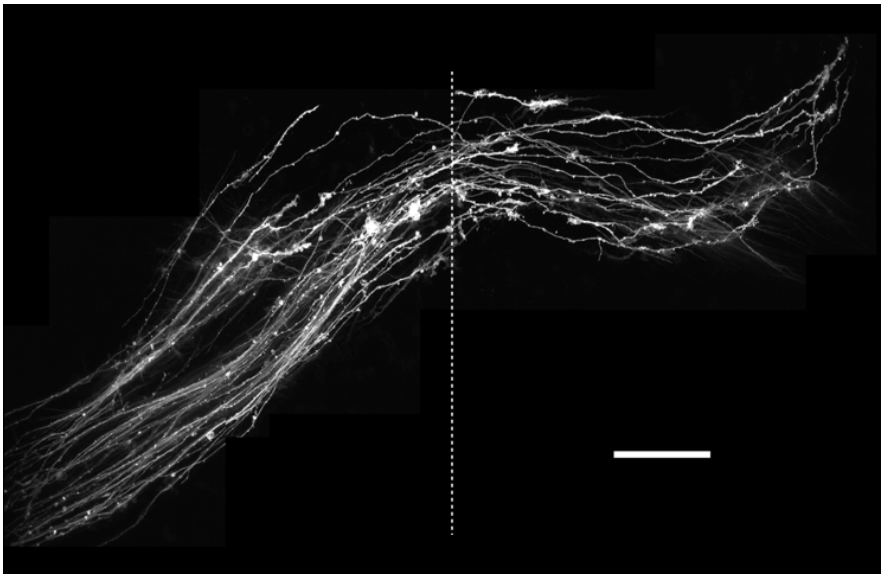

Figure 3.1: Typical image of axons crossing the midline, scale bar 100μm. Dashed line represents the midline. DiI was injected into the right eye (bottom left, off image).

3.2 Automatic axon detection

In order to determine the presence and directions of axons at different points across the image, it is desirable to implement a method that allows this to be done automatically. Several such image analysis techniques exist for performing such a task. The most common technique is to use Gabor patches (Gabor, 1946), which were used initially and shall be described first. After using Gabor patches, I moved to using steerable filters (Freeman and Adelson, 1991) which are a far more efficient way of filtering an image, and shall be described in the section after.

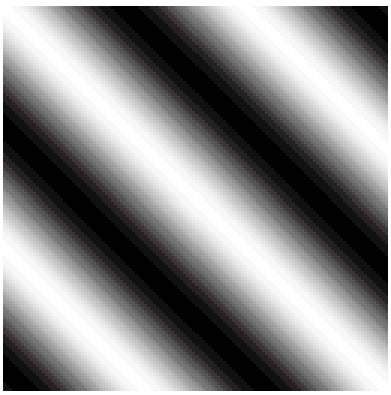

(a) The oriented sinusoidal component of a Gabor patch, $s(x,y)$.

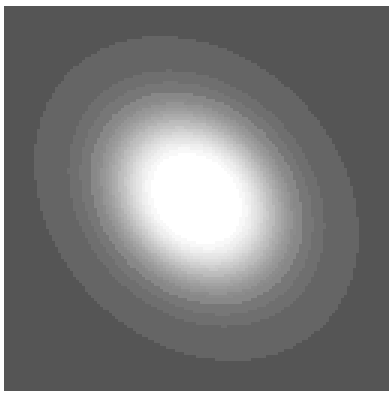

(b) The Gaussian component of a Gabor patch, $w(x,y)$

Figure 3.2: The components making up a Gabor patch

3.2.1 Axon detection using Gabor patches

Gabor patches are a class of 2D functions that are the result of multiplying two other functions together:

$$g(x,y) = s(x,y)w(x,y) \tag{3.1}$$

The form of these two components is illustrated in Figure 3.2, and the multiplication of them to form a Gabor patch in Figure 3.3. This example is oriented at an angle of -45° and is positive along its principal axis and negative along the flanks of the principal axis.

By changing properties of the component functions, the exact form of the Gabor patch can be altered. The form of the Gabor patch shown in Figure 3.3 is the result of choosing the frequency of the sinusoidal component to have a certain frequency (F_0), and the Gaussian component to have a certain radius (a) (see equations 3.2 and 3.3), that is dependent on the width of the axon, L. This now gives a Gabor patch whose width is approximately the same as that of an axon which, as we shall see later, makes it ideal for detecting axons in an image. F_0, a and L are related by:

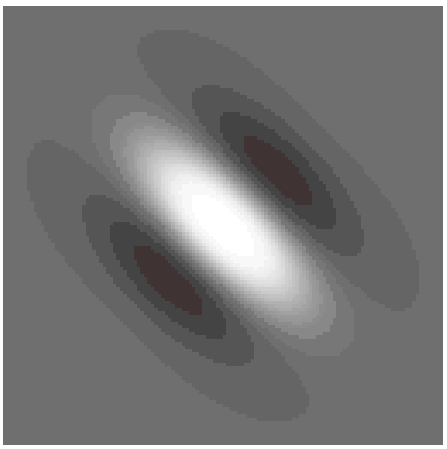

Figure 3.3: An example of a Gabor patch of 45 degree orientation. Formed from the product of $s(x,y)$ and $w(x,y)$, shown in Figure 3.2.

$$F_0 = 1/2L \tag{3.2}$$

$$a = \sqrt{\frac{32F_0^2}{\pi^3}} \tag{3.3}$$

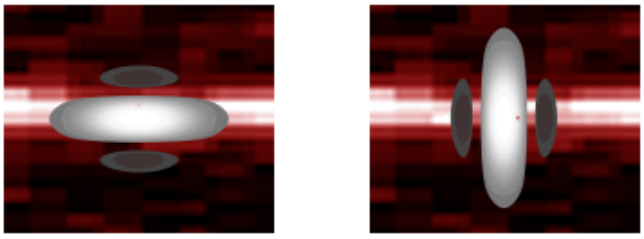

Figure 3.4: In (a) the bright parts (positive pixels) of the Gabor patch align with the bright parts of the axon (high pixel values), and the dark parts (negative pixels) of the Gabor patch align with the dark parts of the image (low pixel values). So this fit has a high score overall. In (b) the opposite is true as has a low score overall, hence the method determines the axon at this point to be at an angle of 0°.

The next step is to use this function as a filter on a test image containing a section of axon (Figure 3.5a), the mathematical term for this is to convolve this function with the image - overlay the patch at every position of the image and multiply and sum the overlapping pixels. The points at which this overlaying of the function gave the

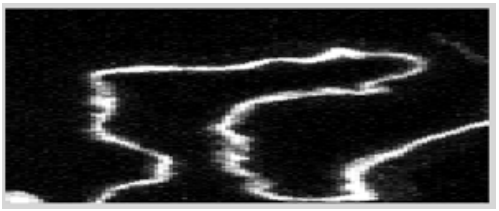

(a) Test image with a short section of axon in it

(b) The response from a -45° Gabor patch

Figure 3.5: A Gabor patch of -45°, and width 5px was convolved with the test image on the left (test image courtesy of Adrianna Teriakidis). On the right we have applied a threshold at 50% of the maximum response. As we see this has highlighted the parts of the axon that are at 45 degrees.

highest values coincides with the centre of any axon that was at a similar orientation as the patch (schematically shown in figure 3.4). Upon thresholding the response from the Gabor patch, it can be seen that the method has successfully picked out sections of the image that contain axon at an angle of -45°, the same orientation as the Gabor patch (Figure 3.5b).

Although this is a good example of how Gabor patches can be used to localise sections of axon of a given direction, what we really wish to know is: ”at what points in an image are there axons and what is their orientation?”, instead of just picking out one direction. For this I use a bank of filters, with different orientations, to convolve with the image. I can use their collective responses to determine the exact orientation of the axon at any point. Figure 3.6 shows what that filter bank may look like. The more filters used the more accurate the estimate of the orientation at any point in the image.

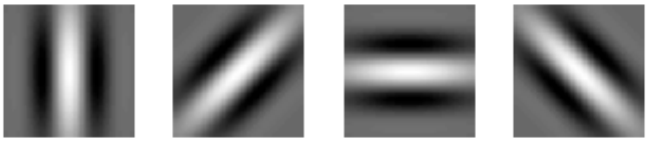

Figure 3.6: A Gabor filter bank with four orientations, spanning 180°.

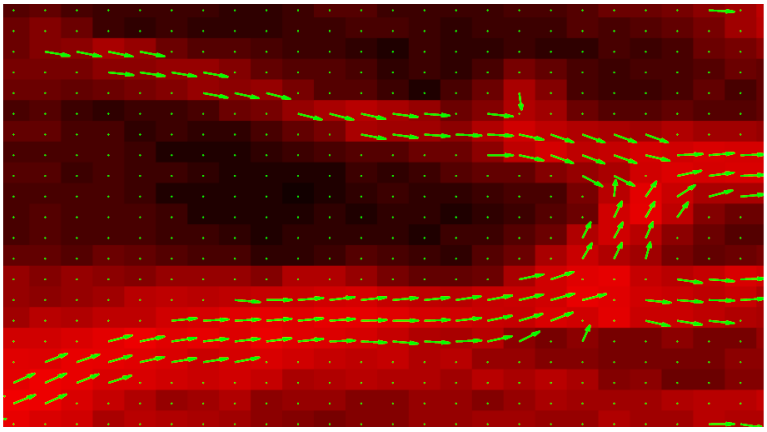

Figure 3.7: The result of filtering for the maximum orientation using a bank of filters of width 3 pixels and thresholding at 50% of the maximum response.

In Figure 3.7, this method manages to pick out both the location of axons in the image and also their orientation. The end of the arrow to which the arrowhead is applied is chosen arbitrarily for illustration purposes, although here we do know that the DiI was injected from the left-hand side of the image so the direction of the arrow will largely point in a distal direction. This arrowhead convention is used throughout the thesis. The reason that there may be several arrows across the width of an axon is that the image is thresholded for the best fit of the Gabor patch at any point in the image, and so even if the Gabor patch is slightly off the centre of an axon, it will still give a value above threshold. In fact, a portion of the image that has an axon of high contrast would give a higher Gabor response across its width than an axon of poor contrast elsewhere in the image. This brings up two issues. Firstly, wider axons (or bundles of overlapping axons) may be represented by proportionately too many arrows and secondly a global threshold may not be appropriate when the contrast of the axons varies so much across the image. In order to overcome this issue a method is needed to keep only the arrows that lie on the central axis of the axon, which I tackle in the next section.

3.2.2 Non-maximum suppression - finding the centres of the axons

An alternative to using a single global threshold across the image is to use non-maximum suppression. The aim is to find all points on the image that are above a certain (loose) threshold and also lie on a ridge with respect to the intensity landscape of the image. Ridge maxima are found by considering each point in the image (here marked with a black circle in Figure 3.8). If the two flanking pixels (determined from the orientation at the point of consideration, shown in white (Figure 3.8)), are lower in intensity than the current one, then the point encircled in black is a ridge maximum. Notice how the points immediately in front or behind the point of consideration must be ignored (marked blue in Figure 3.8), else only the highest points of intensity are picked out. It was found that this algorithm successfully picked out the centres of the axons, as can be seen in Figure 3.9.

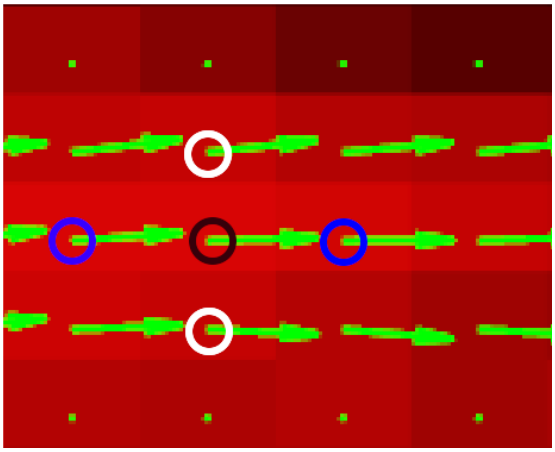

Figure 3.8: The black arrow is tested to see if it is on a ridge. Ignoring points ahead and behind on the ridge (blue), the black point is considered to be on a ridge if its intensity is greater than both the white points.

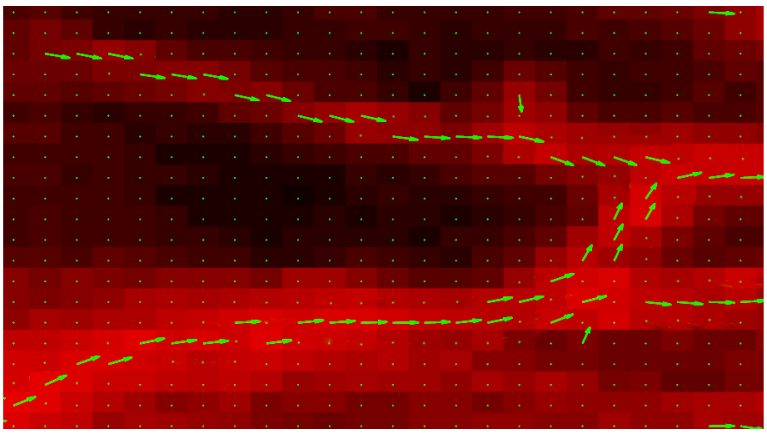

Figure 3.9: The result of removing the arrows not on a ridge maximum

3.3 3D Gabor patches as a means of tracing axons in 3-Dimensions

After getting the 2D Gabor patches to pick out the axons successfully and their intrinsic orientation in a 2D image, the next step was to extend the method to 3D, in order to extract all possible value from 3D confocal stacks. The form of the 3D Gabor patch is the same as the 2D, except that it is rotated around its principal axis illustrated in Figure 3.10.

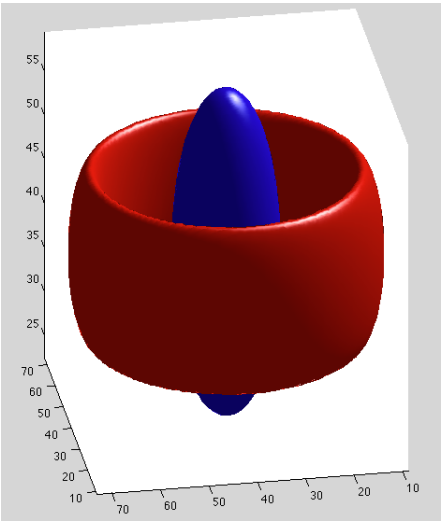

Figure 3.10: A 3-Dimensional Gabor Patch. The blue isosurface represents all points at intensity $+0.5$ and, the red isosurface points at intensity -0.1. $L = 20$, $\theta = 0$, $\phi = 0$.

Instead of rotating the function around though one angle, there now are two angles though which the function can rotate, θ and ϕ. Due to the symmetry, the function has to be rotated through each angle by 180° in order to cover all orientations.

After implementing this method on test data, the filters managed to detect the direction of the fibres with a good degree of accuracy (data not shown). However, two issues were run into when applying the 3D Gabor patches to real data. Firstly it was found that the time taken to convolve the images with the Gabor patches in 3D was significantly longer than for the 2D case due to the higher number of orientations that needed to be filtered and the increased time of 3D convolutions. This increase in computational time hampered the optimisation of the 3D Gabor patch with respect to the free parameters, which was required as the constraint in Equation 3.3 did not give the same quality of results in 3D as it did in 2D. Instead the parameters had to be optimised for a small section of the stack in order to give satisfactory results. However, these local optimisation parameters rarely worked for other areas of the confocal stack. Secondly, there was poor resolution in the z-direction (due to the optical limitation of the microscope) which introduced inaccuracies in terms of Gabor patch alignment that were not present in 2D. This resulted in a method that worked well in some situations, but was not ultimately robust enough. Instead, a more efficient and robust method was sought after, so I turned my attention to steerable filters.

3.4 Steerable filters as a method of axon detection

The theory of steerable filters was laid down by Freeman and Adelson (1991) and describes an efficient and flexible framework for designing a set of oriented filters. This section is more mathematical than the previous section and may be skipped. The take-home message in this section is that computational time is dramatically reduced, whilst still having the same effect as using Gabor patches.

The idea is that the steerable filters are of a class of oriented functions, that can be

combined to give any angle of filter. Gaussian derivatives are an example of steerable filters which I shall describe now, strongly following the first section of Freeman and Adelson (1991). The Gaussian is defined as:

$$G(x,y) = e^{-(x^2+y^2)} \tag{3.4}$$

This is an isotropic function, with no orientation. However, its derivatives in x and y have distinct directions that I shall define as being at 0° and of 90°, respectively.

$$G_1^{0^\circ} = \frac{\partial}{\partial x} e^{-(x^2+y^2)} = -2xe^{-(x^2+y^2)} \tag{3.5}$$

$$G_1^{90^\circ} = \frac{\partial}{\partial y} e^{-(x^2+y^2)} = -2ye^{-(x^2+y^2)} \tag{3.6}$$

Directly combing these two functions yields the same filter but at 45°:

$$\frac{1}{\sqrt{2}} G_1^{0^\circ} + \frac{1}{\sqrt{2}} G_1^{90^\circ} = G_1^{45^\circ} \tag{3.7}$$

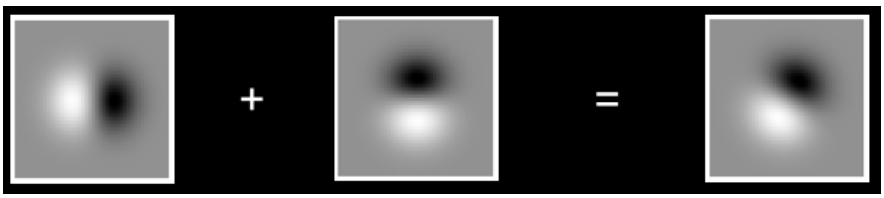

Figure 3.11: An example of the linear sum of two oriented spatial functions resulting in the same function at a different orientation. Illustration of the calculation: $\frac{1}{\sqrt{2}} G_1^{0^\circ} + \frac{1}{\sqrt{2}} G_1^{90^\circ} = G_1^{45^\circ}$.

This calculation is illustrated in Figure 3.11. In order to generate a Gaussian derivative of any arbitrary orientation the following formula is used:

$$G_1^{\theta} = \cos(\theta) G_1^{0^\circ} + \sin(\theta) G_1^{90^\circ} \tag{3.8}$$

We can now use these filters in the same way as the Gabor patches, and convolve (denoted by $*$) them with an image I, giving a response at each orientation R:

$$R_1^{0^\circ} = G_1^{0^\circ} * I \tag{3.9}$$

$$R_1^{90^\circ} = G_1^{90^\circ} * I \tag{3.10}$$

The response at any angle is:

$$R_1^{\theta} = \cos\theta R_1^{0^\circ} + \sin\theta R_1^{90^\circ} \tag{3.11}$$

At a given point (x_0, y_0), we may wish to know the orientation (θ) that yields the maximum response, which would be indicative of the underlying features of the image being at that orientation also.

We need to find the maximum the expression: $a\cos\theta + b\sin\theta$, where a and b are now constants, this expression has two turning points, at $\theta = \pm\arctan(a/b)$. Note that this gives us the analytical solution for the angle giving the maximum response. There's no need to appeal to interpolation as in the Gabor case. In addition the Gaussian derivatives are all $x-y$ separable, (i.e. $G(x,y)$ can be written $f(x) * g(y)$) which means that the convolution can be performed:

$$R_1^{0^\circ} = G_1^{0^\circ} * I = (f_1^{0^\circ} * (g_1^{0^\circ} * I)) \tag{3.12}$$

Successive convolutions of the image with 1D vectors are carried out, resulting in highly efficient filtering. If, as before, the Gabor patch was 20×20, this would result in a filter of 400 pixels being calculated at 8 different orientations resulting in 3200 calculations for each pixel in the image. The first derivative Gaussian steerable filter requires only 20×2 calculations (80) for each pixel in the image. A 40-fold increase in computing speed.

At present these filters act as edge detectors. To obtain filters that can detect axons, I can use the second derivative of a Gaussian, this has the form:

$$G_2^{0^\circ} = \frac{\partial^2}{\partial x^2} e^{k(x^2+y^2)} = (2k^2x^2 - k)e^{-k(x^2+y^2)} \tag{3.13}$$

This form is very similar to the Gabor patch (see Figure 3.12) but with the greater efficiency in convolution and accuracy in determining the optimum angle. We now require three basis functions to steer these second Gaussian derivatives. The full equation is:

$$G_2^{\theta} = \cos^2\theta G_{2a} - 2\cos\theta\sin\theta G_{2b} + \sin^2\theta G_{2c} \tag{3.14}$$

Where

$$G_{2a} = 0.9213(2x^2-1)e^{-(x^2+y^2)} \tag{3.15}$$

$$G_{2b} = 1.843xye^{-(x^2+y^2)} \tag{3.16}$$

$$G_{2c} = 0.9213(2y^2-1)e^{-(x^2+y^2)} \tag{3.17}$$

with normalisation constants included. Note that G_{2b} is $x-y$ separable, so it is possible to gain efficiencies in the convolution process as in the case of the 1D Gaussian derivative.

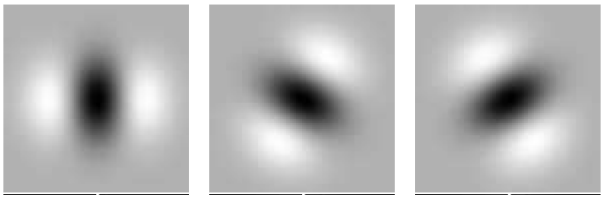

Figure 3.12: 2nd derivative Gaussians at 90°, ±30° respectively.

3.4.1 3D steerable filters for orientation determination in confocal stacks

To extend this now to 3D, it is necessary to to use 3D Gaussian Derivatives. The 3D Gaussian is defined as:

$$g(x,y,z) = e^{-k(x^2+y^2+z^2)} \tag{3.18}$$

Here k defines the width of the Gaussian. The derivative of this function in, say, x and y is:

$$g_{xy} = \frac{\partial}{\partial \mathrm{x}}\frac{\partial}{\partial \mathrm{y}} g(x,y,z) \tag{3.19}$$

$$= 4xye^{-k(x^2+y^2+z^2)} \tag{3.20}$$

Similarly this notation will be used to denote derivatives along other axes (i.e. g_{xz} etc.).

We need to find a combination of these derivatives that have the correct form to trace an axon in 3D. We require a function that looks like the 3D Gabor patch in the previous section, but has all the attractive properties of steerability. We refer to Aguet et al. (2005) for inspiration, as they have developed a form of 3D steerable filter that can detect both surfaces and filaments from 3D data sets. They use the following particular choice of 3D Gaussian derivatives:

$$h(x,y,z) = (g_{xx} + g_{yy} + g_{zz}) - (\alpha + 1)g_{xx}(\theta,\phi) \tag{3.21}$$

The notation $g_{xx}(\theta,\phi)$ represents the 3D 2nd derivative Gaussian in x, with orientation (θ,ϕ). Taking α to be $2/3$ gives a curve detector and $\alpha = 4$ a surface detector. Isosurface projections of both these functions are shown in Figure 3.13.

The implementation of these filters on test data was achieved in MATLAB. The test data generated was a discrete 3D function whose pixel intensity values fell off as an exponential function of the distance to concentric helices passing through the cube. The function for a helix, parameterised by the variable t, is:

$$x = a\sin(t) \tag{3.22}$$

$$y = a\cos(t) \tag{3.23}$$

$$z = bt \tag{3.24}$$

Figure 3.13: 3D steerable filters, as described in Aguet et al. (2005) and Equation 3.21, α is taken to be $2/3$ and 4 respectively

where a is the radius of the helix and b is its slope. Concentric helices were generated, providing test data with many different orientations (see figure 3.14). This gave satisfactory results upon choosing the correct value of k for the Gaussian. It was important to tune this parameter to be comparable with the width of the axons being detected; too large and the filter was not selective enough, too small and the response of the filter was lower than the surrounding blank space. This was actually found to be a major problem when applying the filters to confocal data. The spatial integral of equation 3.21 was found to be negative overall. Ideally the function integral should be zero, meaning that blank space would give a response of zero, directly between axons would give a negative response and a positive response would only occur when directly on the axons. Although this caused only a minor problem on test data, when applying this to confocal data difficulties were encountered. With the added noise surrounding the axons, it was found that instead of the filters giving the highest response along the centre of an axon, they were responding highest in the blank space around the axon, simply because this gave a near zero response, compared to the massively negative responses elsewhere, due to the negativity of the function's integral.

In order to get around this problem the form of the filters was reformulated to give:

$$h(x,y,z) = kg - (g_{xx} + g_{yy} + g_{zz}) + g_{xx}(\theta,\phi) \tag{3.25}$$

This is very similar in form to the previous function, but is different in the sense that the outer negative region is less negative than was found in the previous example, giving an overall integral that is positive and close to zero, which is ideal. When this is applied to test data, much more consistent results are seen, and the choice of k is not as critical to achieving good results. This is important for real data where axon diameter can typical vary by a factor of 4 or 5 in the samples, although these may be bundles of axons. In any case, I would still wish to track the orientation of these bundles.

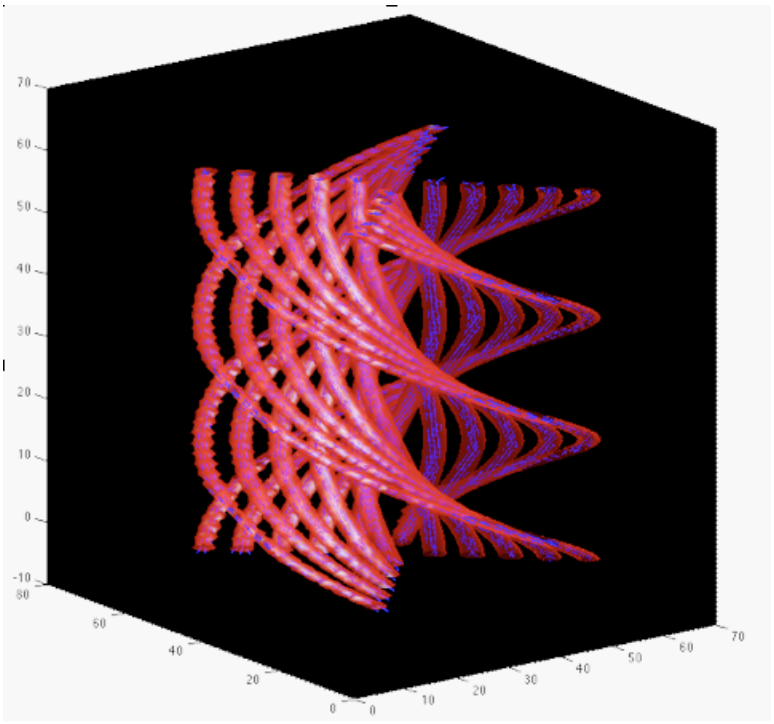

Figure 3.14: 3D steerable filters of the form in equation 3.25 applied to test data. Resulting vector field was simply thresholded to track the centre of each axon.

However, despite repeated attempts at optimising this procedure for real 3D confocal data, both in terms of filter width and thresholding criteria (data not shown), it was not possible to get automatic consistently good results. Although a small part of the image may be traced well after optimisation, the same parameters gave bad re-

sults elsewhere in the image, not to mention other data samples entirely. This was both frustrating and counter-intuitive as I had expected the utilisation of the full 3D data to give more evidence, not less, as to the direction the axons were going in. This was a real problem in terms of what I was trying to do. After careful re-evaluation and analysing the algorithm thoroughly and also taking into account the difficulty in obtaining the corresponding 3D gradients of expression patterns, it was decided that the project would stick to focussing on 2D data, and using the 2D Gaussian derivative functions instead. This is still a novel approach and at a future date, it would still be possible to apply the same ideas to 3D again.

3.5 Applying 2D steerable filters to DiI traced axons

Returning now to 2D, the 2nd derivative Gaussian steerable filters are applied to DiI filled axons in 2D. After extensive optimisation the final version of the algorithm is as follows:

- Filter with 2D 2nd derivative Gaussian filters, with $k = 1.8\mu$m
- Find vectors at each point corresponding with maximum filter response
- Non-maximum suppression using the ridge maximum algorithm described earlier
- Threshold the image based on pixel intensity (I) and filter response (R) at each pixel under the condition: $I > 2 \times \text{median}(I)$ and $R > 2 \times \text{median}(R)$
- Smooth with a Gaussian filter $k = 29.25\mu$m
- Calculate the curl of the smoothed directional vector field

As shown in the example application in Figure 3.15, the algorithm has for the first time provided a method that can determine both the vector field representing the orientation of axons in a given image and also the curl of the vector field that represents

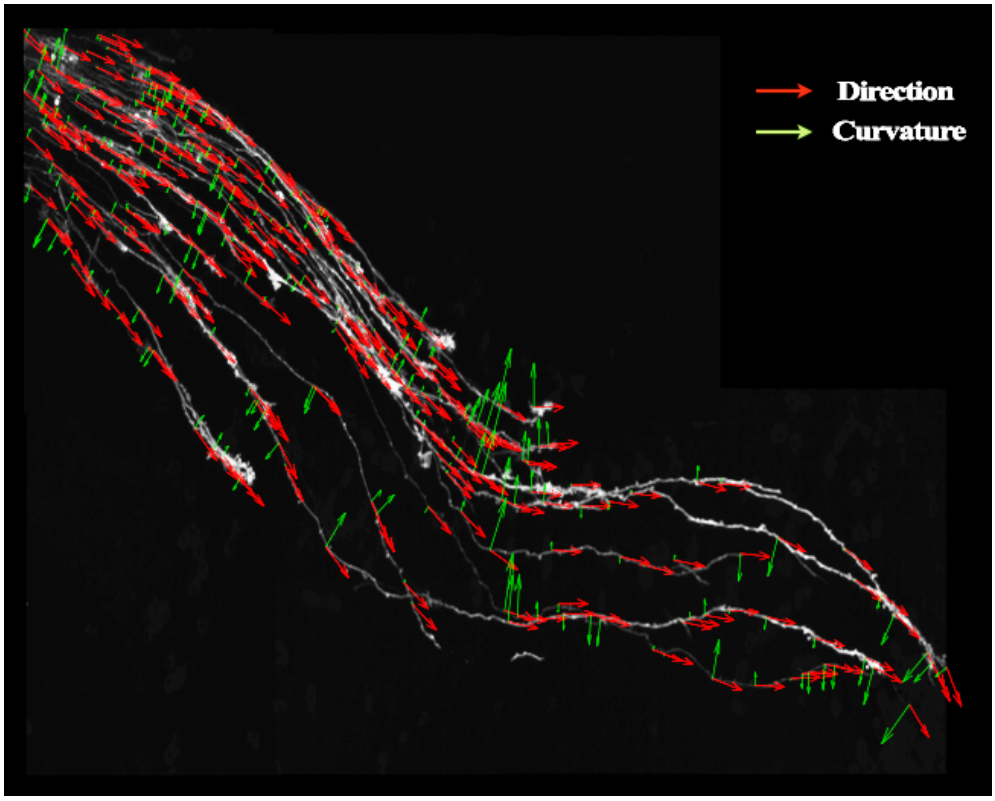

Figure 3.15: The application of 2D steerable filters to DiI filled axons at the optic chiasm. Red arrows represent the axon direction, green the axon curvature. For illustration, only a subset of arrows have been visualised.

the curvature of axons (how much they're turning). Notice that the direction vectors (red arrows in figure 3.15) have a constant magnitude, but the curvature has both direction and length. The direction indicates the direction the axons are turning at that point and the magnitude of the vector indicates the amount by which they are turning. Large arrows indicate that there must be a very strong force inducing the axons to turn, whereas a small arrow is indicative of the axon only making a slight turn. These quantities are very important to understand for the field of axon guidance and this is the first algorithm designed that can automatically quantify them.

3.6 Aligning the chiasm images to a universal set of co-ordinates

In order to compare the multiple images obtained, it was necessary to find a way of aligning and scaling the images such that they can be meaningfully compared. The method I used was to choose two landmarks in the tissue (in this case the centre of each of the eyes), and rotate and scale the images, placing them on a grid that was defined as having the origin (0,0) at the centre of the left eye and the right eye being at (1,0), with the positive x-axis point in the anterior direction. This alignment scheme is summarised in figure 3.16.

In order to align our confocal images to this universal co-ordinate system, first the points are shifted relative to the position of the confocal image in relation to the brightfield. I define the position of the points in the original image to be $(x_{\text{local}}, y_{\text{local}})$, and the two landmarks to be $(x_{\text{LE}}, y_{\text{LE}})$ for the left eye, and $(x_{\text{RE}}, y_{\text{RE}})$ for the right eye. I also need to know the position of the downscaled confocal image in relation to the brightfield images. I define the position of the confocal image to be $(x_{\text{CF}}, y_{\text{CF}})$. Finally, the distance between the points is shrunk due to the different powers of the confocal and brightfield microscopes, giving a scale difference of 9.55 in the case of the 40X confocal images, or a scale difference of 4.78 for the 20X images, for the 40X images:

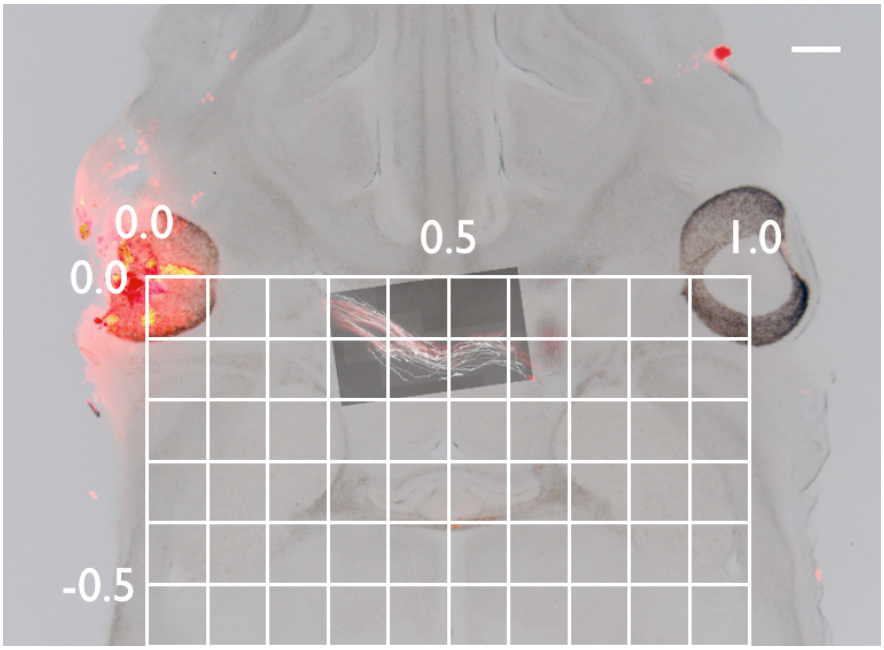

Figure 3.16: Overlay alignment image, demonstrating the universal grid system. Two images were taken at 2.5x magnification and overlaid at 50% opacity in Photoshop. The high-power confocal image was downscaled and aligned with the brightfield images. scale bar 200μm

$$x_{\text{new}} \rightarrow x_{\text{local}}/9.55 + x_{\text{CF}} - x_{\text{LE}} \tag{3.26}$$

$$y_{\text{new}} \rightarrow y_{\text{local}}/9.55 + y_{\text{CF}} - y_{\text{LE}} \tag{3.27}$$

This now puts the confocal data points into the frame of reference of the brightfield images. However, I still need to rotate and re-scale the image such that it conforms to the grid in image 3.16. I calculate the x-distance between the two eye co-ordinates as being Δx and between the y-co-ordinates as being Δy, which allows us to calculate the angle of rotation (θ) by using: $\tan(\Delta x/\Delta y)$, and the inter-eye distance (D) using Pythagorus theorem. I then apply the spatial transformations:

$$x_{\text{new}} = (x_{\text{local}}\cos(\theta) + y_{\text{local}}\sin\theta)/D \tag{3.28}$$

$$y_{\text{new}} = (-x_{\text{local}}\sin(\theta) + y_{\text{local}}\cos\theta)/D \tag{3.29}$$

For any vector fields we may have calculated in the frame of reference of the confocal image, the position of these vectors change as above, but in addition, the angles must also be adjusted, so $\phi \rightarrow \phi - \theta$.

3.7 Chapter Summary

In this section I have detailed the experimental methodology used to image developing axons at the optic chiasm as well the extensive work done in creating an automatic tracing method in order to quantify the axon behaviour in a meaningful manner. In addition I have showed that on both test data and confocal data that this method gives the quality of tracing that we need. I now have a powerful tool which could be put to many quantification tasks in axon guidance. In the next chapter I show how this tool can now be used to investigate axon guidance phenomena at the mouse optic chiasm, in particular, looking at Slit-dependent axon guidance.

Chapter 4

Results: A quantification of Slit-Dependent axon guidance at the mouse optic chiasm

In this chapter I shall describe the application of my algorithm to studying the precise spatial differences in axon behaviour at the optic chiasm in the absence of either/both Slit1 and Slit2. This adds to the extensive work already done on Slit-dependent axon guidance at the optic chiasm (Erskine et al., 2000; Plump et al., 2002; Conway et al., 2011). These spatial differences were tested for statistical significance using false discovery rate (FDR) to control for false positives. This resulted in revealing novel differences between Slit1 and Slit2 knockouts in terms of both axon density, and axon orientation.

4.1 Obtaining Slit1/Slit2 knockouts

58 embryos were obtained, genotyped (See Appendix B), injected with DiI and their chiasm imaged as described in the previous chapter. The following table shows the different numbers of each genotype that were gathered:

		Slit 1		
		+/+	+/-	-/-
Slit2	+/+	9	9	11
	+/-	8	3	9
	-/-	5	0	4

Table 4.1: This table summarises the number of embryos generated for each genotype. All possible genotypes were generated with the exception of $Slit1^{+/-};Slit2^{-/-}$.

All genotypes were generated with the exception of $Slit1^{+/-};Slit2^{-/-}$. Figures 4.2 to 4.9 show the raw confocal images with the algorithm applied and the vector fields overlaid (only a random subset of arrows shown for clarity). As seen from visual inspection, the algorithm has been successful at tracing the gross direction of the axon bundle, with only a few areas where axons were missed. An example of this has been highlighted in Figure 4.5. In addition the curvature appears to have been estimated accurately all areas where axons were identified. Given that the same thresholding method was used for each of these images, the algorithm is remarkably robust, which is of great importance when biological variability can be so high. I will now describe each genotype in turn.

4.1.1 $Slit1^{+/+};Slit2^{+/+}$

As can be seen in Figure 4.2 there is large variability in the number of axons that have reached the midline by E13.5 for wildtype embryos. For example, in image A it can be seen that in this sample relatively few axons have reached the midline and that the distance between axons is much higher than in some of the other images such as images E and F where far more axons have crossed the midline. This low density of axons in image A has allowed the algorithm to identify individual axons, or at the very least small bundles of axons. It would be possible to extend the algorithm to connect

the arrows together in order to estimate the exact trajectories of the axons, whereas this would not be possible for images E and F for example.

It appears that image F has a small number of misrouted axons entering a region anterior (highlighted by box). This may be due to some misdirection that occurs in a random subset of wildtype embryos, or an indication that this embryo was at a more advanced stage in development than the other wildtype embryos, or it may be the result of a genotyping error. However, the algorithm appears to have missed the majority of axons in this region and therefore will not be included in later statistical analysis.

Notice that Images E and F have a band along the middle where there is no dye. This is due to the chiasm being split over two physical sections as a result of the tissue cutting process.

4.1.2 $Slit1^{+/+};Slit2^{+/-}$

Figure 4.3 shows the traced DiI images for embryos of genotype $Slit1^{+/+};Slit2^{+/-}$. It can be seen that the algorithm has worked well on this set of data too. The exception is image D where some spurious, unattached axons have been identified (highlighted with box), these may be from axon tracts other than the optic nerve that have entered the palne of section from a different route. In image C the curvature appears to have been overestimated (highlighted by box) as a result of the discontinuity caused by aligning two images.

Compared with wildtype the number of axons reaching the midline appears to be increased and there are no cases where we see so few axons that they can be individually identified as we did for wildtype. However the majority of wildtype embryos had large numbers of axons crossing the midline too, so perhaps this difference is down to biological variability.

4.1.3 $Slit1^{+/+};Slit2^{-/-}$

Figure 4.4 shows the result of the complete knock out of Slit2 on the formation of the optic chiasm. In contrast to the wildtype embryos the chiasm looks much more symmetrical with respect to the anterior-posterior axis, with far more axons crossing the midline at a position anterior to the wildtype crossing point. The chiasm appears to have the shape of a horizontal hourglass as opposed to the wildtype where it is more the shape of an arch.

4.1.4 $Slit1^{+/-};Slit2^{+/+}$

In Figure 4.5 we can see the images of the optic chiasm for the heterozygous knockout of Slit1. Again the tracings appeared to have been successful, with only a few axons missed in image C. The optic chiasm appears largely very similar to wildtype with the exception of figure B where the axons appear to be entering a completely different region away from the normal position of the chiasm and are approaching the midline at a point dramatically posterior.

4.1.5 $Slit1^{+/-};Slit2^{+/-}$

Figure 4.6 shows the only three embryos that were generated for this $Slit1^{+/-};Slit2^{+/-}$ genotype. In each of these images the chiasm appears very similar to wildtype. Image A appears to be another example of a chiasm with relatively few axons crossing the midline. These axons then appears to branch out after crossing the midline in a way that others embryos chiasm do not. In image C, it appears that an artefact has been generated along the midline leading to the curvature and direction at some points being inaccurately assessed (highlighted by box).

4.1.6 $Slit1^{-/-};Slit2^{+/+}$

Figure 4.7 shows the data for the embryos of genotype $Slit1^{-/-};Slit2^{+/+}$. As you can see there is again variability as to the number of axons at the optic chiasm. Overall the algorithm has worked well with the exception of image I which has a large number of spurious arrows away from the axons. These appear to have arisen from high background noise which have resulted in false positive identification of axons. The source of this noise is unknown.

Overall these data look very similar to wildtype with the exception of image F which appears to have a number of axons taking a wider turn prior to crossing the midline which is not apparent in other samples. However this effect appears to only be present in this sample.

4.1.7 $Slit1^{-/-};Slit2^{+/-}$

Figure 4.8 shows the images for embryos of genotype $Slit1^{-/-};Slit2^{+/-}$. These samples appears to exhibit large variability in the shape of the optic chiasm. For example the width of the chiasm in F appears to be several times wider than in H. Again it is unknown if this is the result of an age related change and the chiasm in H is a number of hours behind F in terms of development. This is possible as the age range of these embryos is: E13.5 $\pm$ 0.25 days. Overall the algorithm appears to have worked well for these data.

4.1.8 $Slit1^{-/-};Slit2^{-/-}$

Figure 4.9 shows the DiI images of the chiasm for the double mutants. These data show by far the biggest changes from wildtype with large numbers of axons going completely astray, but only in a posterior direction. The main bulk of the chiasm appears to have moved in an anterior direction also. Again biological variability is high as image A appears very different from the other three in terms of the number of

axons in total and the percentage of wayward axons. However, this again may be due to this chiasm being earlier in development

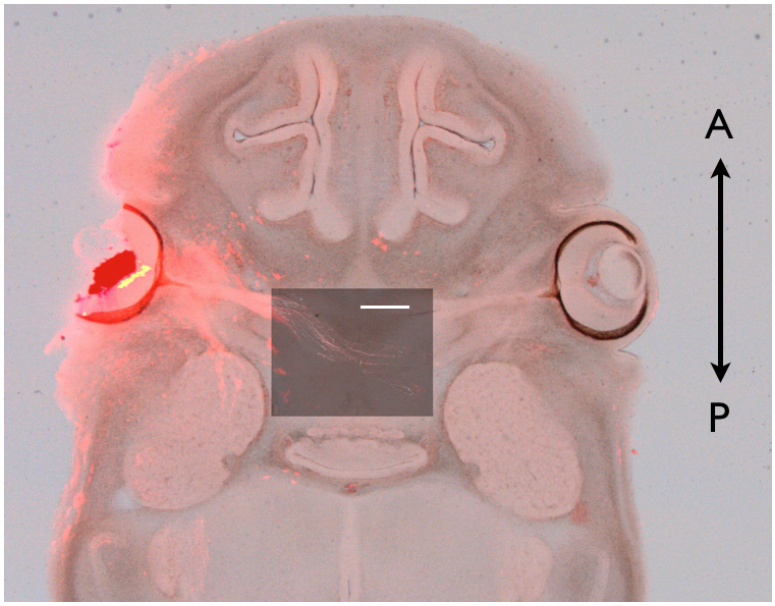

Figure 4.1: In all the following images and analysis the perspective above shall be used, with the dye injecting into the right eye. Scale bar 200μm, A = Anterior, P = Posterior.

4.2 Visual inspection of the directional vector fields on a universal grid

I have now summarised what can be seen from the raw images overlaid with the direction and curvature vector fields. These images were hard to compare because they were not aligned to the same axis. As described in the previous chapter it is possible to translate and rotate the vector fields onto a universal grid so that the directions and curvatures of the chiasms of the same genotype can easily be compared. This allows us to further examine variability between samples of the same genotype and to allow a visual comparison between the vector fields of different genotypes. The results are shown in Figure 4.10.

Looking at the extent of the direction vector fields, the cases of $Slit1^{+/+}$;$Slit2^{+/+}$,

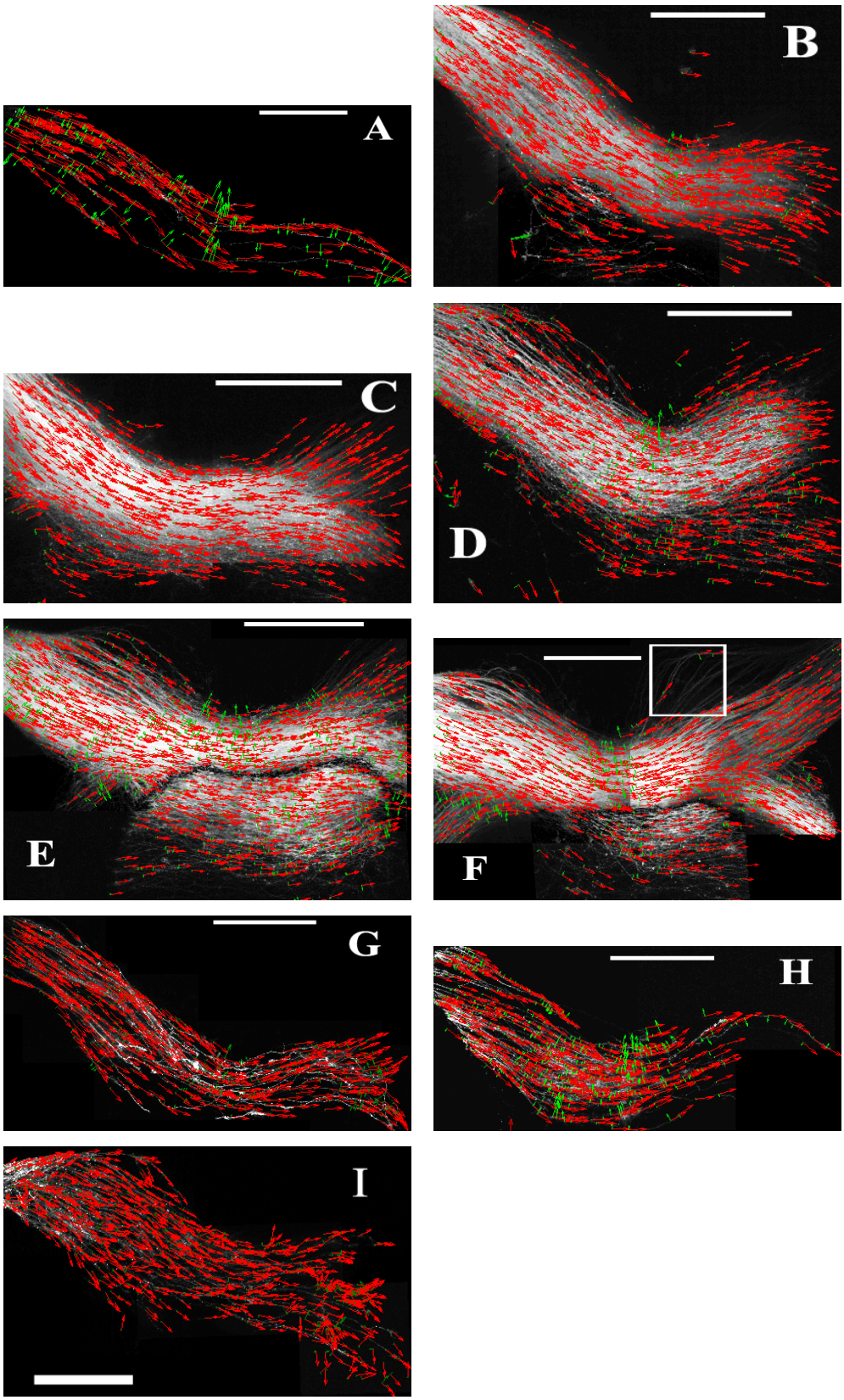

Figure 4.2: DiI staining of RGC axons crossing the optic chiasm with direction vector field (red) and curvature vector field (green) overlaid for mouse of genotype: $Slit1^{+/+};Slit2^{+/+}$. Each image from a different embryo. Scale bar $200\mu m$.

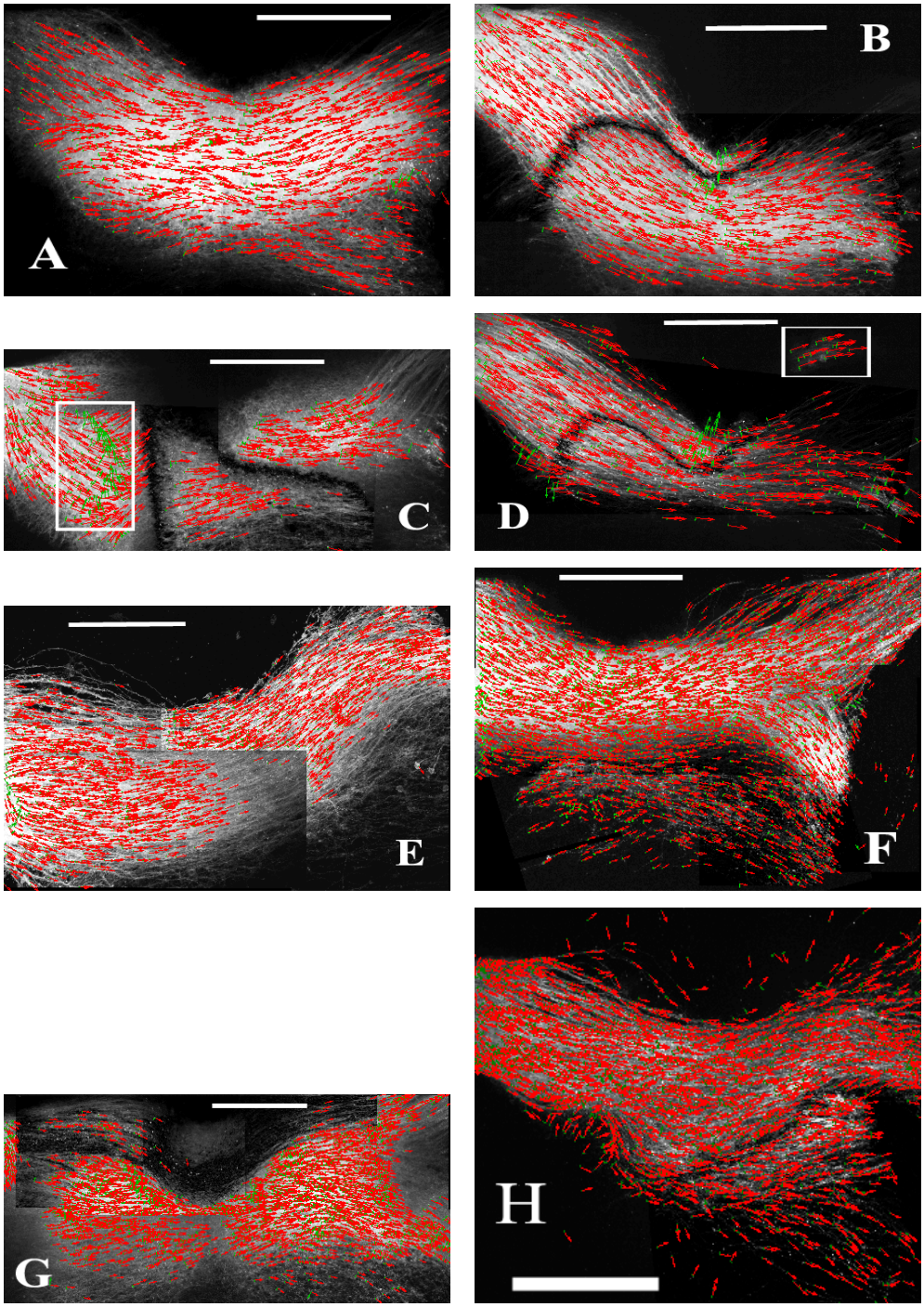

Figure 4.3: DiI staining of RGC axons crossing the optic chiasm with direction vector field (red) and curvature vector field (green) overlaid for mouse of genotype: $Slit1^{+/+};Slit2^{+/-}$. Each image from a different embryo. Scale bar $200\mu m$.

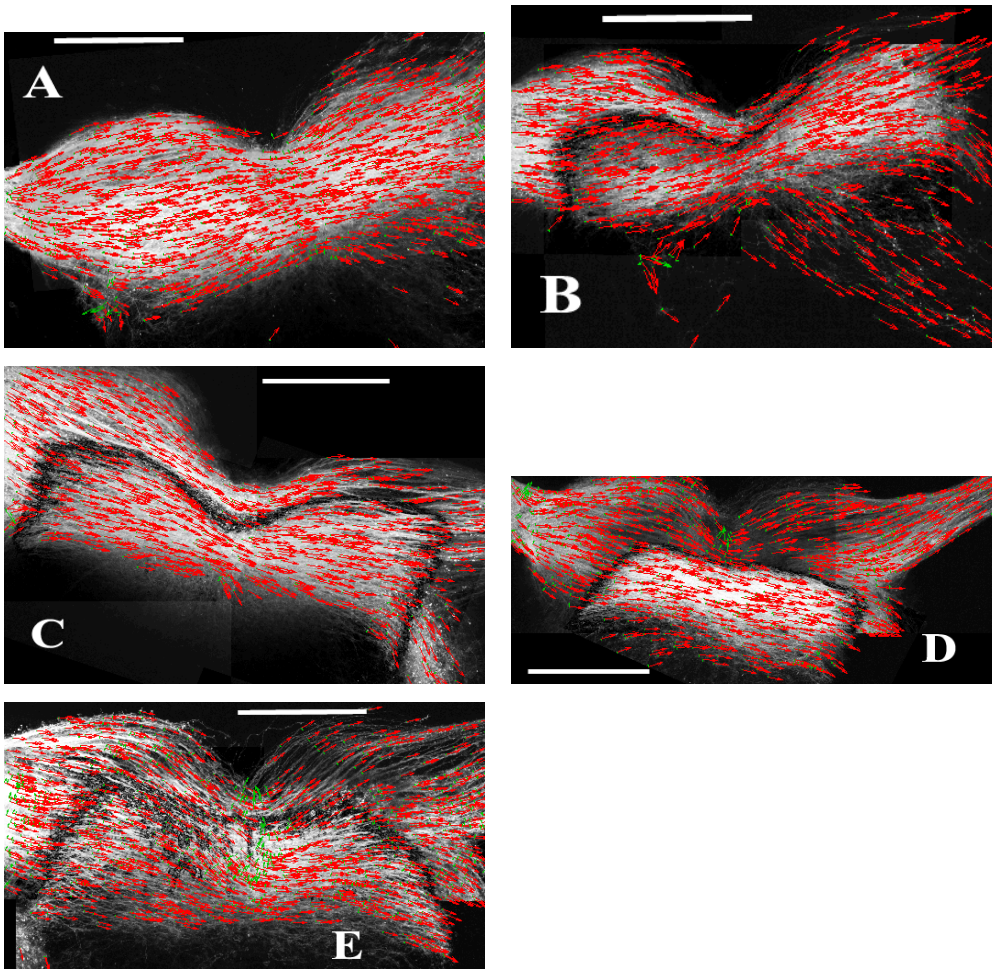

Figure 4.4: DiI staining of RGC axons crossing the optic chiasm with direction vector field (red) and curvature vector field (green) overlaid for mouse of genotype: $Slit1^{+/+};Slit2^{-/-}$. Each image from a different embryo. Scale bar $200\mu m$.

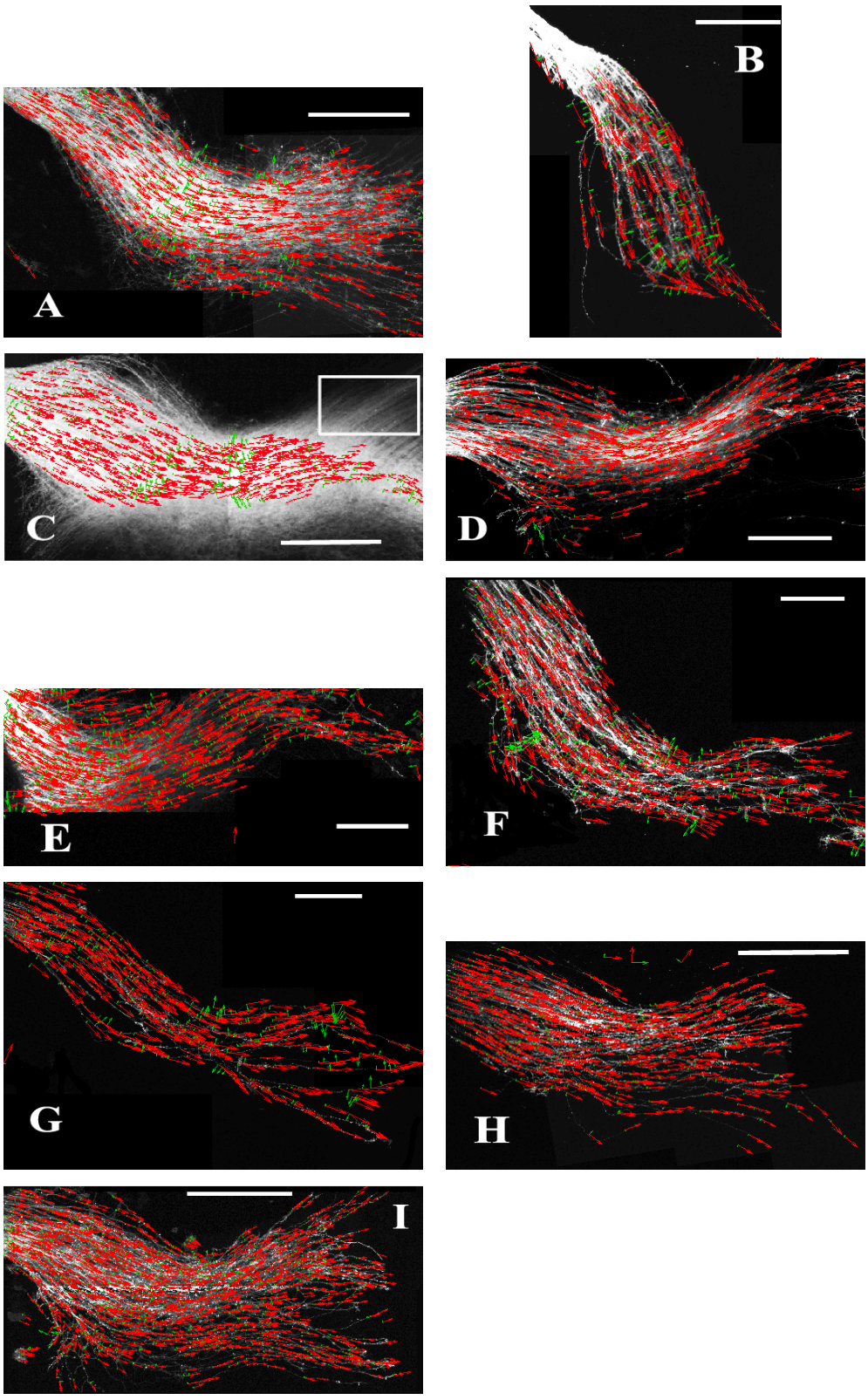

Figure 4.5: DiI staining of RGC axons crossing the optic chiasm with direction vector field (red) and curvature vector field (green) overlaid for mouse of genotype: $Slit1^{+/-};Slit2^{+/+}$. Region of interest highlighted by white box indicates one of the few areas where the algorithm failed to identify the axons. Each image from a different embryo. Scale bar $200\mu m$.

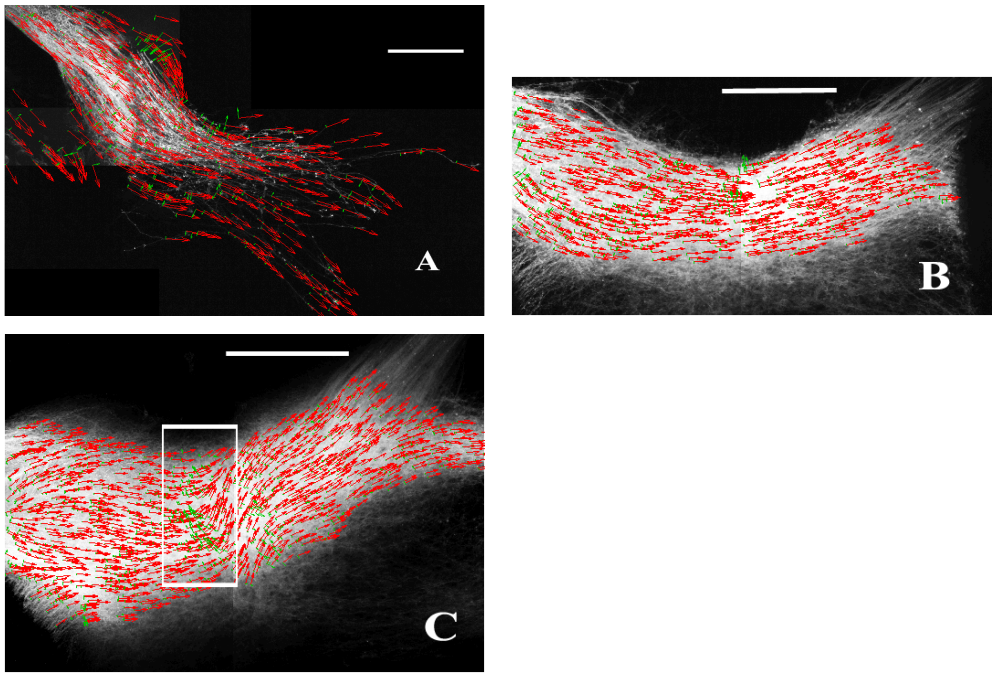

Figure 4.6: DiI staining of RGC axons crossing the optic chiasm with direction vector field (red) and curvature vector field (green) overlaid for mouse of genotype: $Slit1^{+/-};Slit2^{+/-}$. Each image from a different embryo. Scale bar $200\mu m$.

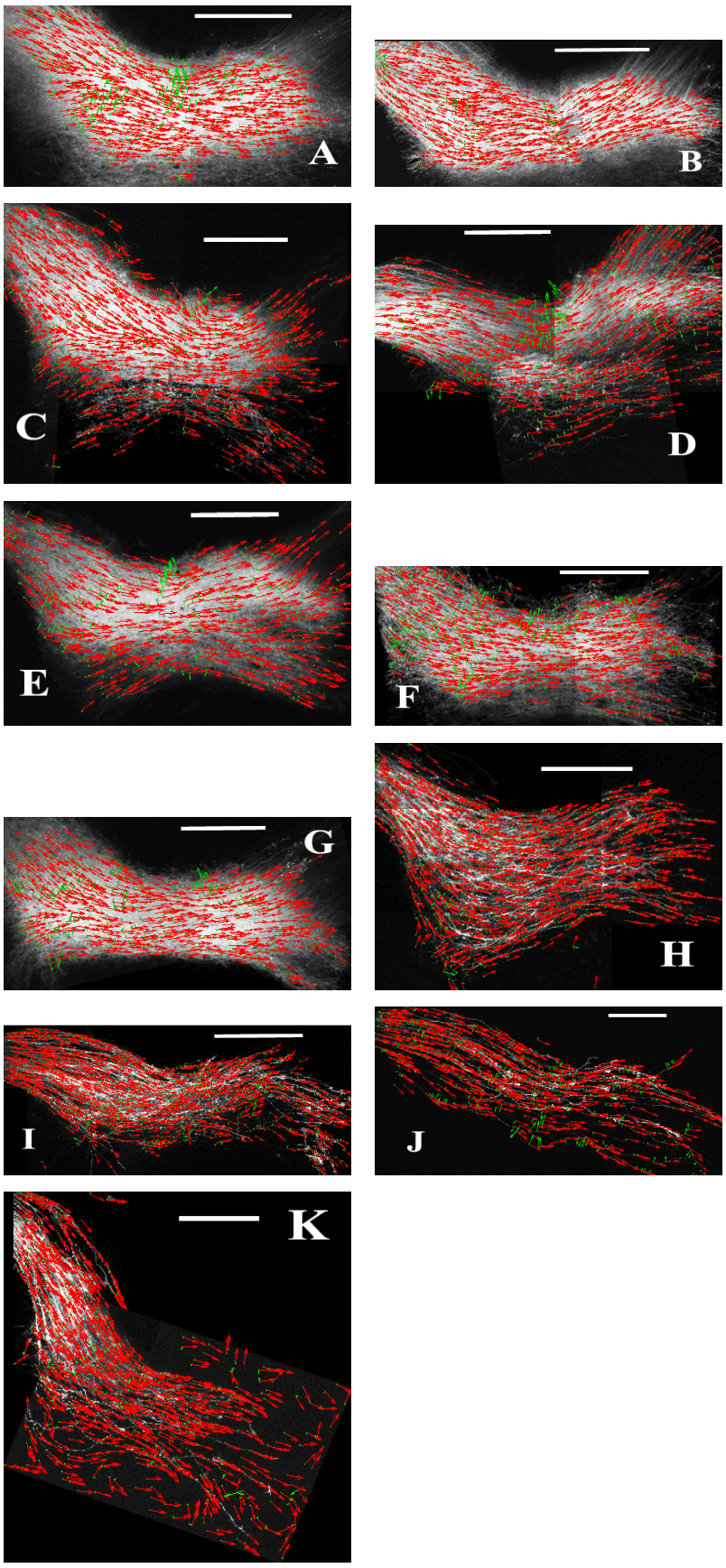

Figure 4.7: DiI staining of RGC axons crossing the optic chiasm with direction vector field (red) and curvature vector field (green) overlaid for mouse of genotype: $Slit1^{-/-};Slit2^{+/+}$. Each image from a different embryo. Scale bar $200\mu m$.

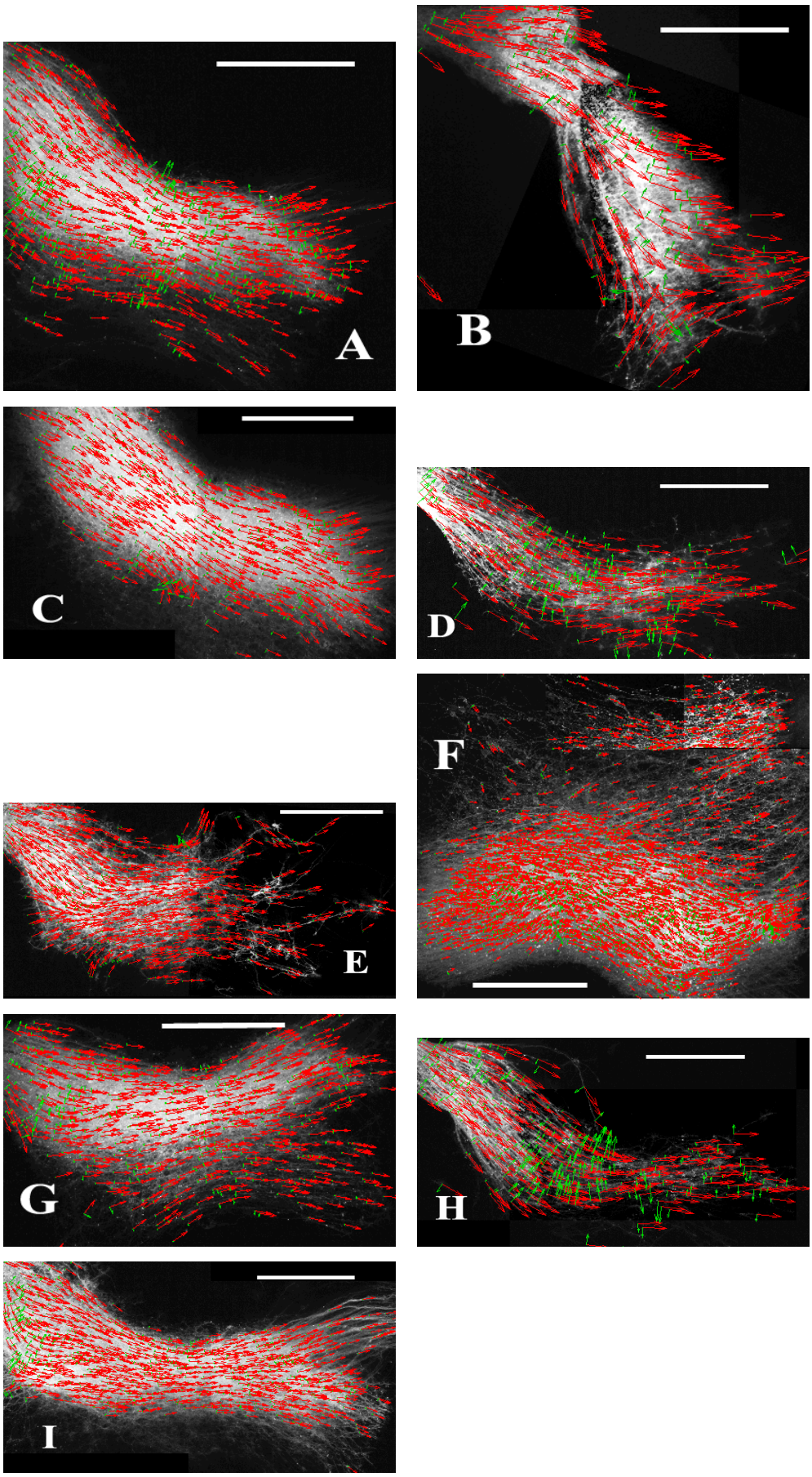

Figure 4.8: DiI staining of RGC axons crossing the optic chiasm with direction vector field (red) and curvature vector field (green) overlaid for mouse of genotype: $Slit1^{-/-}; Slit2^{+/-}$. Each image from a different embryo. Scale bar $200\mu m$.

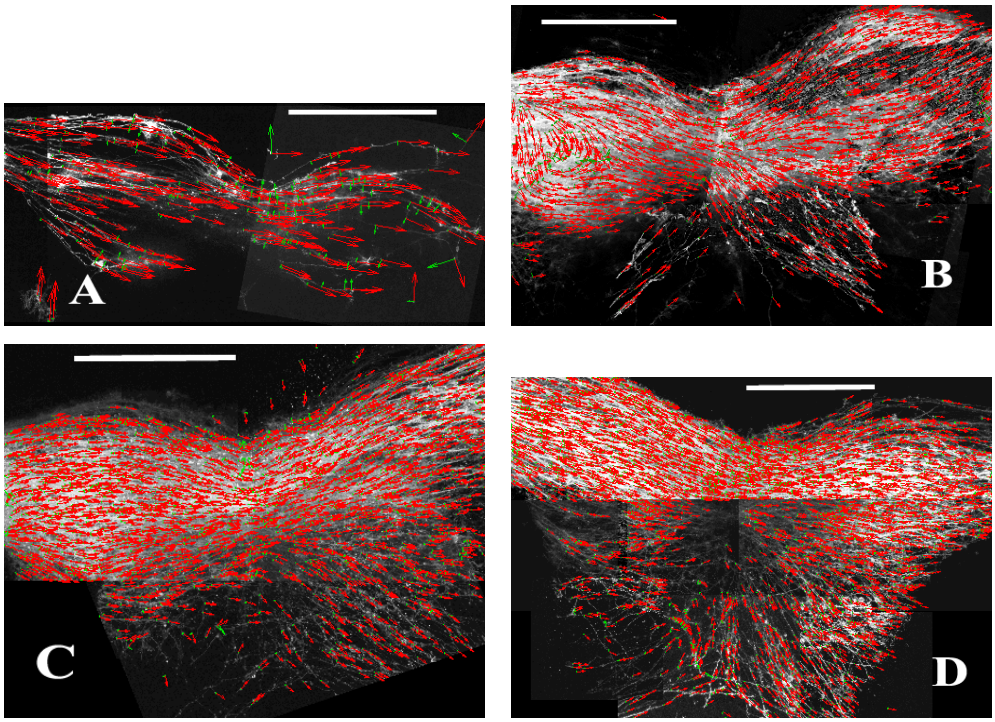

Figure 4.9: DiI staining of RGC axons the optic chiasm with direction vector field (red) and curvature vector field (green) overlaid for mouse of genotype: $Slit1^{-/-};Slit2^{-/-}$. Each image from a different embryo. Scale bar $200\mu m$.

$Slit1^{+/-};Slit2^{+/+}$ and $Slit1^{+/+};Slit2^{+/-}$ (Figure 4.10A, B and D) look remarkably similar, suggesting that the removal of just one copy of either gene has little effect on the overall phenotype at the chiasm. The $Slit1^{-/-};Slit2^{+/-}$ (Figure 4.10 F) chiasm also appears very similar to wildtype despite the complete removal of Slit1 and partial removal of Slit2. The $Slit1^{-/-};Slit2^{+/+}$ (Figure 4.10C) chiasm appears to have more axons entering the area around (0.45, -0.25) than in wildtype, although this only appears to have happened in a couple of samples. It is hard to draw any conclusions from the $Slit1^{+/-};Slit2^{+/-}$ (Figure 4.10E) as I only obtained three samples for this genotype, and only two samples appear to have successfully been analysed by the algorithm. By far the most dramatic changes seem to come from the complete removal of Slit2 i.e. $Slit1^{+/+};Slit2^{-/-}$, $Slit1^{-/-};Slit2^{-/-}$ (Figures 4.10G and H). In both these cases the bundle at the midline appears to have shifted in the anterior direction, in comparison with the wildtype. In the case of $Slit1^{+/+};Slit2^{-/-}$ there almost appears to be a contraction of the bundle at the midline, forming a hour-glass shape. But in the double mutant $Slit1^{-/-};Slit2^{-/-}$ there are large numbers of axons wandering in a posterior direction. These observations agree with what was found in Erskine et al. (2000) and Plump et al. (2002), with the exception that the single knockout of Slit2 does appear quite different form wildtype, which was not previously observed. This demonstrates the power of using this algorithm to visually compare different genotypes by aligning them to the same grid, something that was not previously possible.

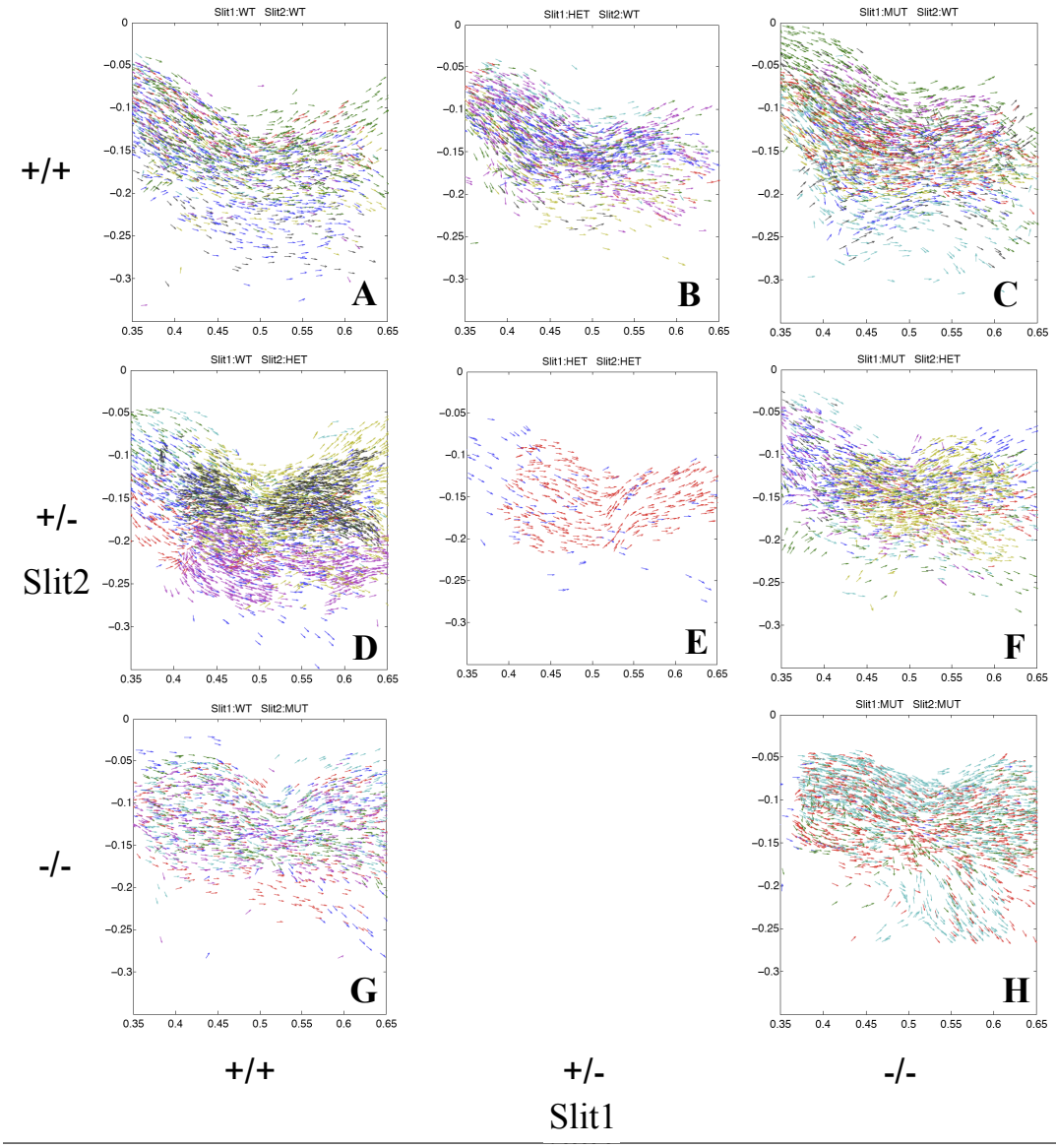

Figure 4.10: Overlaying the directional vector fields, each sample represented with a different colour. Axes set to universal co-ordinates (left eye at (0,0), right eye at (1,0)).

4.3 Looking for statistical differences between genotypes

Now that visual inspection of the different genotypes has identified several differences, it is possible to statistically quantify the differences seen. There are two principle criteria that I use to assess the differences between the images. As the algorithm can detect both the presence and direction of axons I look at these differences from wild-type across the chiasm for each knockout, in terms of both direction and axon number. In order to do this the chiasm is split into a 32×32 grid, and these differences will be compared at each point using a students t-test. However, because this will generate multiple hypotheses, the number of false positives would need to be controlled. Typically Bonferroni correction would be used (Dunn, 1961), which controls for false positives by dividing the level of significance required by the number of hypothesis tests carried out. For n tests, each test would pass at the 5% level if it's p-value is less than $0.05/n$. This method is often too harsh with a large number of hypotheses (here we have over 900). A common method when dealing with spatial data is to use a method known as FDR, which stands for "false discovery rate". It is a method for controlling the false discovery rate and shall be described in the next section.

4.3.1 False Discovery Rate reduction

False discovery rate (FDR) control is a statistical method used to control for multiple comparisons when hypothesis testing (Benjamini and Hochberg, 1995), and limits the proportion of acceptable false positives (type I errors) to some value, α. Suppose there are m hypothesis tests. The following table represents all the possible outcomes.

	no. declared non-significant	no. declared significant	total
no. true null hypotheses	U	V	m_0
no. false null hypotheses	T	S	$m - m_0$
Total	$m - R$	R	m

m_0 is the number of true null hypotheses, $m - m_0$ is the number of false null hypotheses, U is the number of true negatives, V is the number of false positives, T is the number of false negatives, S is the number of true positives. If m hypotheses $(H_1, ..., H_m)$, of which m_0 are true null hypotheses, the expected (denoted by $E[x]$), or mean, false discovery rate is:

$$\mathrm{E}\left[\frac{V}{V+S}\right] = \mathrm{E}\left[\frac{V}{R}\right] \leq \alpha \tag{4.1}$$

We ensure this is limited to α by listing the p-values for each hypothesis $(H_1, ..., H_m)$, in sequential order:

$$P_1 \leq P_2 \leq ... \leq P_m \tag{4.2}$$

We then find the largest value of k for which:

$$P_k \leq \frac{k}{m}\alpha \tag{4.3}$$

is true. We then reject (declare positive) all hypotheses up to that value (i.e. $H_1, ..., H_k$). This ensures that on average the true value of α will have a mean of:

$$\frac{\alpha(m+1)}{2m} \tag{4.4}$$

When m is large this tends to $\alpha/2$. For a full proof of this see Benjamini and Hochberg (1995). It is found that this method for detecting false positives is slightly less conservative that Bonferroni, but has greater power than familywise error rate (FWER) (Hochberg and Tamhane (1987)). It has been tried and tested in areas such as

microarray analysis, and is a standard tool in analysing spatial data in geography and climate change, which statistically has strong parallels with what we are attempting to achieve here.

In all following statistical tests α is taken to be 0.05.

4.4 Comparing knockout phenotypes with WT phenotypes

In this section I first go though the differences in the axon number/density between genotypes and then the differences in the axon direction. I leave a full discussion of the biological significance of these results until the next chapter when I include the in situ data and analysis.

4.4.1 Comparing axon density between genotypes

Although the algorithm was able to pick out the centres of the axons, due to resolution issues it may not have been possible to distinguish between a small bundle of axons and one large axon. Perhaps more abstract terminology should be used, such as "Axon Density". In any case, statistical differences in this quantity between genotypes are investigated.

The initial observation that the chiasm appeared to have moved to a more anterior position in the double knockout ($Slit1^{-/-};Slit2^{-/-}$) was found to be true when applying the statistical analysis (Figure 4.11), which shows a large area of statistical difference from wildtype in this area. The number of axons posterior to this point appear not to differ between the two, suggesting that the result seen is an overall shift of the optic chiasm, as opposed to an overall spreading out of the axon bundle.

The phenotype in the absence of only Slit2 is very similar to the double knockout (figure 4.12). Again, there are significantly more axons in the area posterior to the

wildtype chiasm, but the area over which this spreads is more contained than in the double knockout. This suggests that perhaps Slit2 is a more important guidance factor at the optic chiasm than Slit1. This is supported in Figure 4.13, which shows that the Slit1 knockout exhibits no statistical difference from the wildtype chiasm with respect to axon density across the image. When we compare the single Slit2 knockout $Slit1^{+/+};Slit2^{-/-}$ with the double knockout $Slit1^{-/-};Slit2^{-/-}$, we find no statistical significance with respect to the axon density. This suggests that the two phenotypes with respect to axon density across the image are indistinguishable from each other and that Slit1 has a much smaller role in directing axon guidance at the mouse optic chiasm.

4.4.2 Comparing axon orientation between genotypes

Looking now at the differences between the directions of axons across the image between genotypes, in figure 4.11, we see that the $Slit1^{-/-};Slit2^{-/-}$ posterior portion of the chiasm contains axons that are similar in number to wildtype, yet travelling in a different direction. This suggests a directional influence; although this region is no more attractive/unattractive to enter for the axons, there is still a guiding defect from the missing Slits. As was seen for axon density, there is a similar if slightly reduced phenotype in the single Slit2 knockout over the double knockout (Figure 4.12). Again, there is little difference between the $Slit1^{+/+};Slit2^{-/-}$ and $Slit1^{-/-};Slit2^{-/-}$ with respect to axon direction. With the single Slit1 knockout, although the number of axons does not differ from the wildtype significantly, there is a region (again posterior to the WT chiasm), where the angle does differ from WT significantly (figure 4.13), this suggests both that Slit1 has less impact at the chiasm than Slit2, but also that its influence on the axon bundle at the chiasm is more subtle.

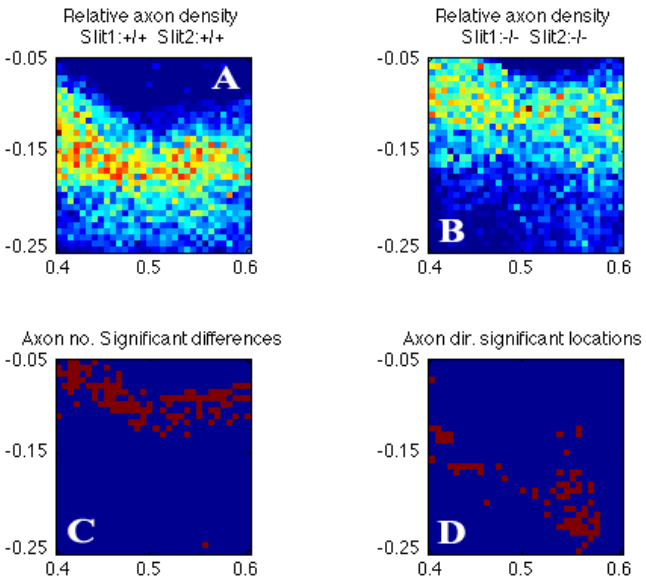

Figure 4.11: Comparing the $Slit1^{+/+};Slit2^{+/+}$ with the $Slit1^{-/-};Slit2^{-/-}$ phenotypes. Red indicates significance at that location, in lower two panels ($\alpha = 0.05$). There is a significant difference in the overall axon density in the anterior part of the image. There is a significant difference in the axon direction around the edges of the image.

4.5 Chapter Summary

In this chapter I have shown that my novel method can be used be applied to real data and successfully reveal the corresponding direction and curvature vector fields accurately. In addition I have shown how the complementary FDR method can be used to establish precise differences between genotypes at the mouse optic chiasm.

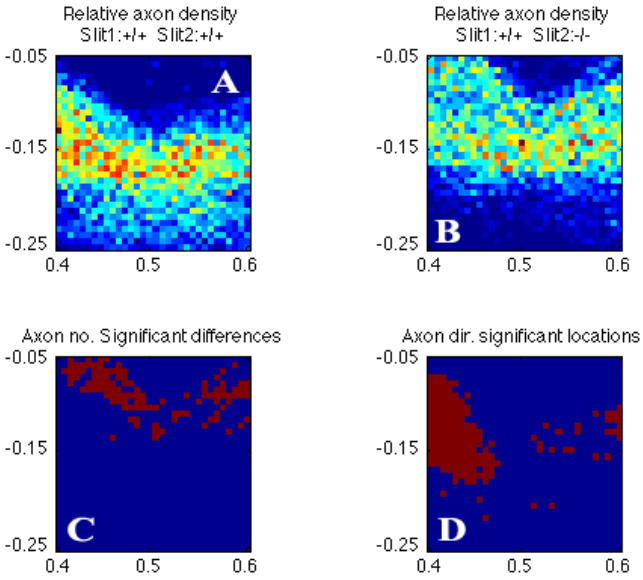

Figure 4.12: Comparing the $Slit1^{+/+};Slit2^{+/+}$ with the $Slit1^{+/+};Slit2^{-/-}$ phenotypes. Red indicates significance at that location, in lower two panels ($\alpha = 0.05$). There is a significant difference in the overall relative number of axon in the anterior part of the image, but to a lesser extent that the double knockout. There is a significant difference in the axon direction around the edges of the image, but again to a lesser extent.

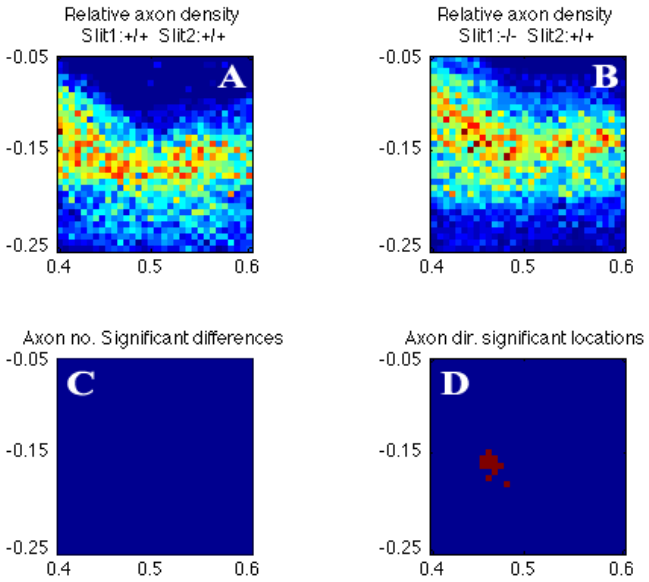

Figure 4.13: Comparing the $Slit1^{+/+};Slit2^{+/+}$ with the $Slit1^{-/-};Slit2^{+/+}$ phenotypes. Red indicates significance at that location, in lower two panels ($\alpha = 0.05$). No significant difference from the wildtype to the Slit1 mutant anywhere in the image. There is also only a small region of the image that is significantly different in terms of the axon directions.

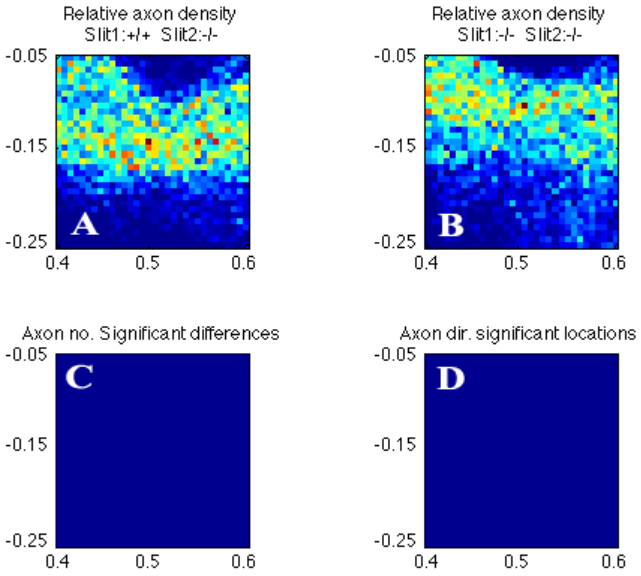

Figure 4.14: Comparing the $Slit1^{+/+};Slit2^{-/-}$ with the $Slit1^{-/-};Slit2^{-/-}$ phenotypes. Red indicates significance at that location, in lower two panels ($\alpha = 0.05$). There is no difference between the single $Slit2^{-/-}$ the double knockout, $Slit1^{-/-};Slit2^{-/-}$, indicating that Slit2 plays more of a role in guiding axons at the optic chiasm that Slit1.

Chapter 5

Comparing the gradient of Slit1 and Slit2 with axonal behaviour

In this chapter I look at how the gradients of Slit1 and Slit2 relate to the vector field of axon direction and curvature. In particular I test the hypothesis that the gradients of Slit1 and Slit2 are consistently proportional to the change in axon curvature of the knockouts from wildtype.

5.1 Results: In Situ Hybridisation

The initial aim of this project was to determine the 3 dimensional gradient of Slit1 and Slit2. In order to achieve this I tried several different methods. These methods included fluorescent in situ hybridisation (FISH) and anti-GFP immunohistochemistry on wax sections. However, these all failed to work sufficiently for the purposes of gradient quantification. In line with the 2D work in axon tracing, the 2D gradient of Slit1 and Slit2 was instead sought after. In order to obtain this I used colormetric in situ hybridisation (protocol shown in Appendix B), which is far more reliable than FISH.

A number of in situs were performed successfully using the colormetric method, although a few had to be rejected due to imperfections, such as asymmetric staining

and tissue damage. It was key to use the best samples as the imperfections would be falsely included in the quantification. In total I acquired 3 samples of each genotype. Whilst the Slit1 expression was always confined to one of the two 150μm sections that made up the optic chiasm, in each of the Slit2 in situs, expression spread over both sections. This may be due to the randomness of the level at which the cutting starts, although this probably indicates that at this stage in development the Slit2 expression pervades a larger area; both at the chiasm itself and the surrounding tissue through which the Slit proteins may diffuse.

5.1.1 Viewing the raw data

In all of the data shown in Figures 5.1 and 5.2, there is no saturation at the chiasm and little background staining. These images were then aligned and scaled to a universal grid as mentioned in the previous chapter and the overlapping image was used to calculate the gradient, as I discuss in the next section.

However, when you compare the plane of section of these in situs with those in Erskine et al. (2000), it is possible that the sections I have taken are above the actual optic chiasm. However, as the slits are secreted diffusible proteins, it is assumed that high levels of slit mRNA expression above the chiasm will result in high concentrations of the slit protein at the chiasm itself, via diffusion along radial glial cells.

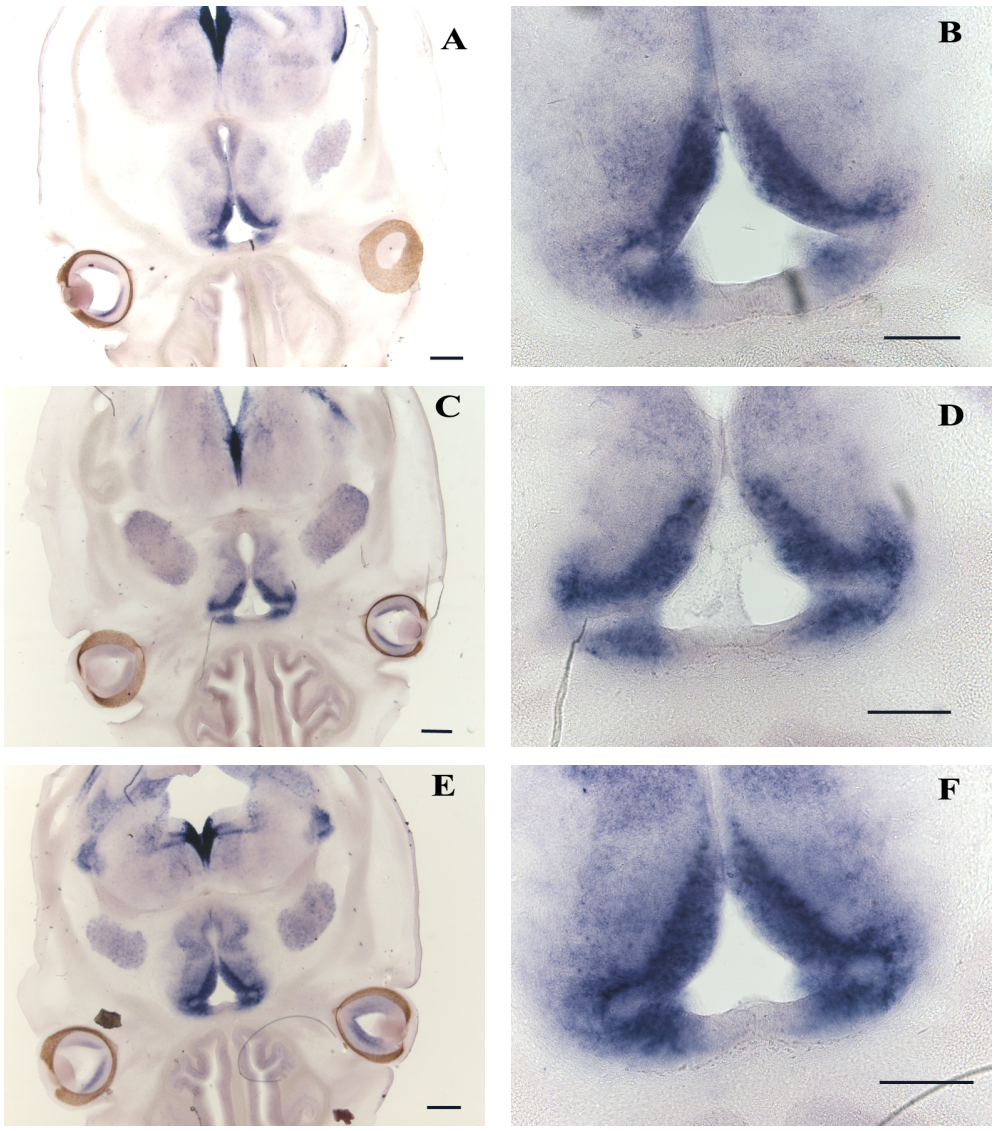

Figure 5.1: Colormetric in situ hybridisation for Slit1 on E13.5 horizontal sections. A,C and E are form different embryos imaged at 2.5X magnification, B, D and F their 10X magnification counterparts respectively. Scale bar $200\mu m$.

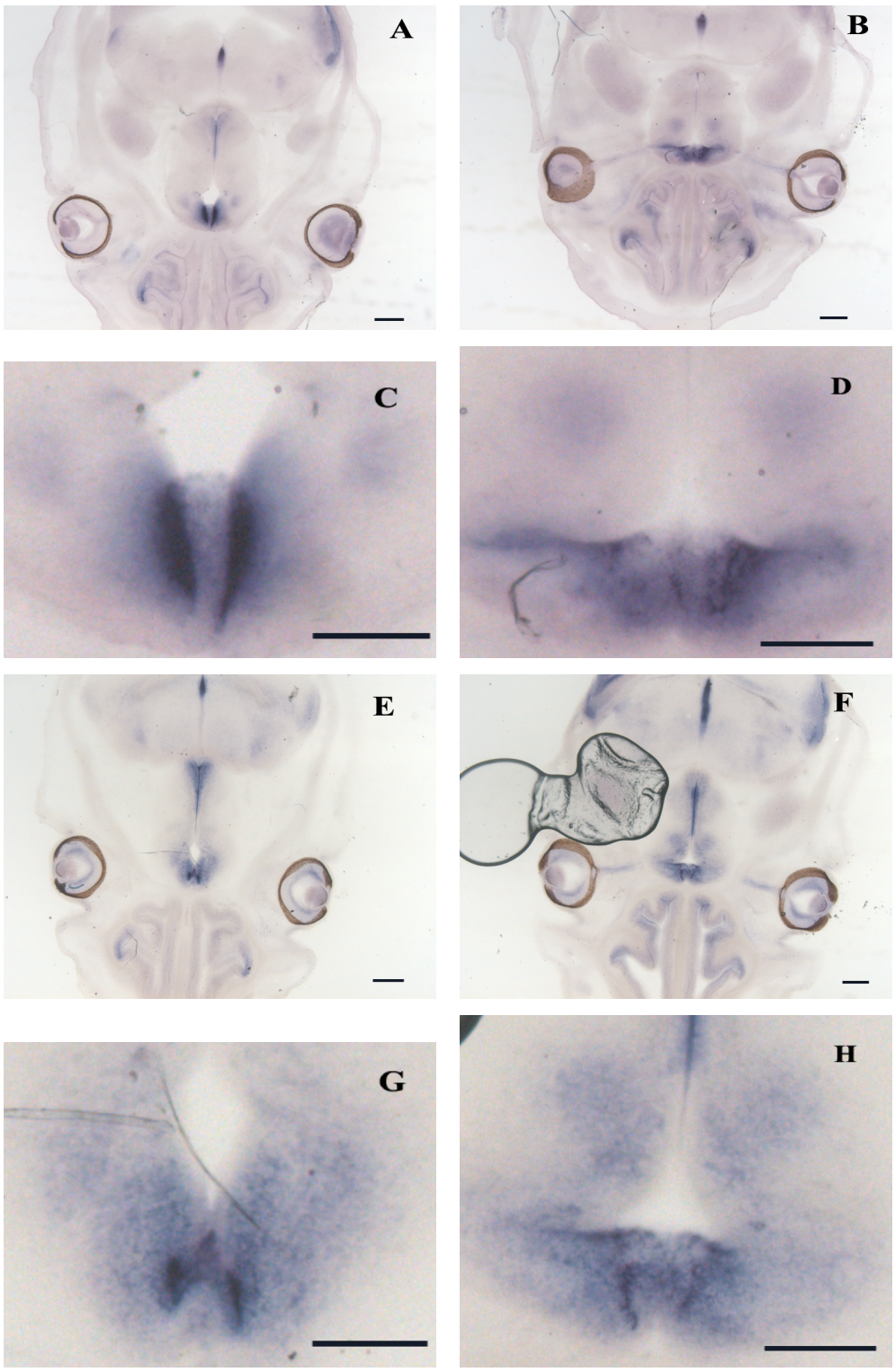

Figure 5.2: Colormetric in situ hybridisation for Slit2 on E13.5 horizontal sections. A and B are from the same embryo and represent the dorsal and ventral sections of the chiasm, imaged at 2.5X. C and D are their 10X counterparts respectively. E and F are again from the same embryo and represent the dorsal and ventral sections of the chiasm, imaged at 2.5X. G and H are their 10X counterparts respectively. Scale bar $200\mu m$.

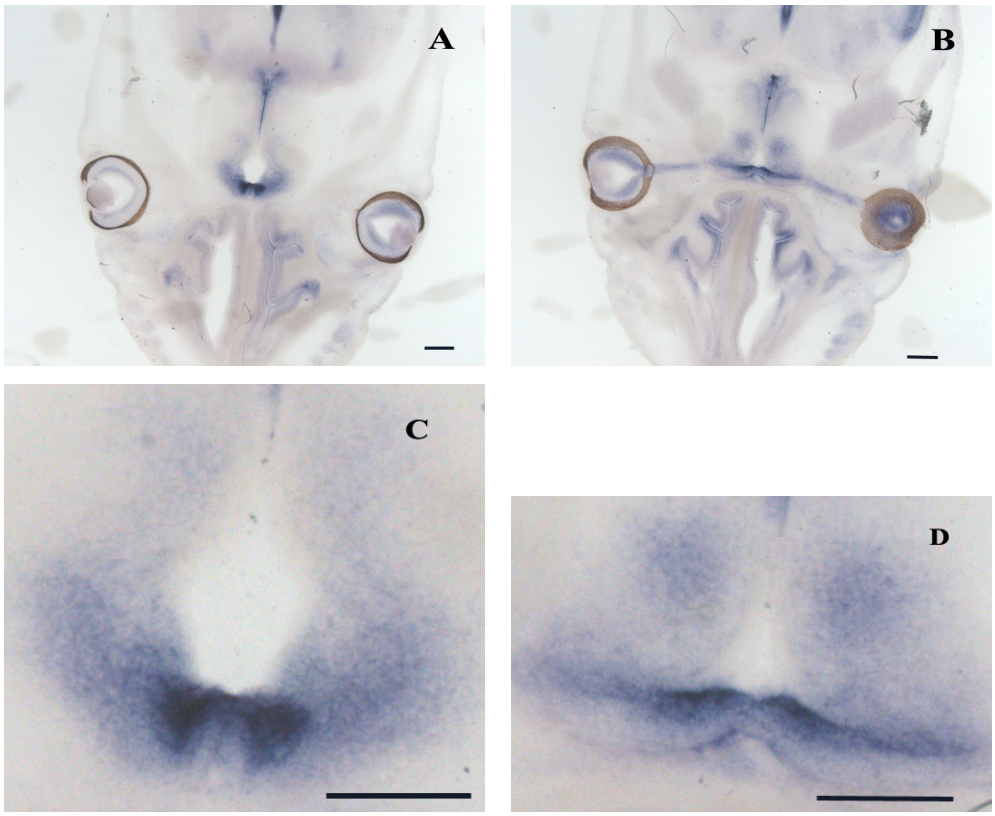

Figure 5.3: Colormetric In Situ hybridisation for Slit2 on E13.5 horizontal sections (continued). A and B are from the same embryo and represent the dorsal and ventral sections of the chiasm, imaged at 2.5X. C and D are their 10X counterparts respectively. Scale bar $200\mu m$.

5.1.2 Calculating the gradient from the combined in situ images.

Using the combined in situ images, I used MATLAB to smooth out the images using a Gaussian filter of radius 30μm and then to calculate the gradient vector field. This vector field was aligned to the same universal grid as in the previous chapter, shown in Figure 5.4. Recall that the convention of the universal grid is that positive along the y-axis is anterior and negative is posterior; along the x-axis 0.5 represents the midline. Notice how the original images have been down-sampled in order to allow the gradient to be viewed with greater clarity. There is a low amount of overlap in the two expression patterns meaning that the gradient of each guidance cue may be pointing in different directions at the same point in the chiasm (Figure 5.4), which gives further indication that the slits may be working in chorus but not in unison to achieve the observed directional influence at the optic chiasm.

Below the raw data in Figure 5.4, I have plotted the circular histogram of the gradient directions. The directions of the gradient of Slit2 mainly point in the posterior direction, with very few arrows pointing in the opposite direction, whereas the distribution of the gradient in the case of Slit1 is much more uniform over the full 360°.

5.2 Mean angular trends across the optic chiasm

In this section I investigate if their is a consistent relationship between the direction axons are oriented and the direction of the mRNA gradients of Slit1 and Slit2 across the chiasm, as well as comparing the axon curvatures with the slit mRNA gradients.

At each point in the chiasm I compare the angle of the mean gradient vector with the angle of the axon direction/curvature and average this value across the whole chiasm. I have several estimates for this mean value based on each of the embryos used in the DiI tracing experiments. These estimates can be combined to see if there is a consistent relationship from embryo to embryo and statistical tests can be applied. Although this is a global metric (based on all points in the chiasm), it is derived from the local relation-

ship between the mRNA gradient vector fields (arrows) and axon direction/curvature vector fields. The result of applying this metric to the different genotypes is described in the next sections.

We might expect to see a relationship between the mRNA gradients of Slit1 and Slit2 and the orientations/curvatures of axons in the wildtype. My premise is that this would be the result of the causality between the slit protein gradients and the interpretation of that gradient by the growth cone. If this is true then this relationship would diminish/disappear in the knockouts. The quantification of the axon orientations and curvatures as well as the quantification of the gradients allow this to be fully investigated for the first time. I shall now go through each genotype and describe what I observed.

5.2.1 $Slit1^{+/+};Slit2^{+/+}$

Figure 5.6 shows this analysis for the embryos of genotype $Slit1^{+/+};Slit2^{+/+}$. Figures 5.6A and B show the mean direction and curvatures (blue and green respectively) for wildtype axons overlaid onto the intensity pattern of the averaged in situ pattern for Slit1 (5.6A) and Slit2 (5.6B), with these mRNA gradients denoted by red arrows. The key for these diagrams is shown in Figure 5.5, and higher resolution versions of these diagrams are shown in Appendix C.

These images give an interesting overview of the data I have collected. There is quite a striking difference between the number of axons entering regions of high Slit1 mRNA expression (Figure 5.6A) and the number of axons entering regions of high Slit2 mRNA expression (Figure 5.6B), with the latter showing an appreciable avoidance from such regions that are not observed in the former. Colormetric in situs are not perfect indicators of the absolute levels of mRNA or indeed where the proteins actually end up, but this does give some further support to the notion that Slit2 plays a more important role in axon guidance at the optic chiasm than Slit1.

But perhaps surprisingly the area where axons are making the biggest turns, indi-

cated by large green arrows around (0.5,-0.1) in universal co-ordinates, is anti-parallel to the Slit2 gradient at that point (Figure 5.6B). This is the opposite of what might be expected if Slit2 is acting as a repulsive guidance cue.

In Figures 5.6C and D I have plotted the circular histogram of the axon directions and curvatures. It can be seen that the spread of axon directions across the chiasm are constrained to the interval $\pm 30^{\circ}$ to the horizontal (Figure 5.6C). These axons made both right and left turns as they crossed the chiasm, the spread of which can be seen in Figure 5.6, with a slight bias towards a left in this region.

Panels 5.6E and F show the mean angular differences across the chiasm between the axon directions and the mRNA gradients of Slit1 and Slit2 respectively. Each red arrow represents the mean from a different embryo (for reference I have plotted a blue arrow at 0° as this angle represents no difference between the mRNA gradient and axon direction). The spread of these data is represented by the three black arrows which represent the mean and 95% confidence interval of red arrows (note that in some of these plots only one black arrow is plotted, this is because the 95% confidence is greater than 360° and is therefore undefined). It is observed that the mean angular difference between the direction and mRNA gradients of Slit1 is clustered around 210°, nearly anti-parallel to Slit1 and for Slit2 the angular difference is clustered around 50°, almost the opposite direction to Slit1. To test this result for significance the Rayleigh test was used which calculates the probability of observing the distribution of angles given that they came from a circular uniform distribution. This gave p-values of 0.13 and 0.04 for Slit1 and Slit2 respectively. Which is just significant at the 5% level for Slit2. As the mean value of the angular difference was found to lie between $[\pm 90^{\circ}]$ this supports the notion that Slit2 is acting as a repulsive cue.

Panels 5.6G and H apply the same analysis for the axon curvatures and the mRNA gradients of Slit1 and Slit2. Here there is a much larger spread and the p-values from the Rayleigh test were found to be 0.53 and 0.52 respectively. This indicates that there is no consistent relationship between the axon curvatures and the mRNA gradients of

Slit1 and Slit2 across the optic chiasm between samples.

This analysis has given some interesting results. The visualisation of the mRNA gradients and the in situ intensities overlaid with the mean axon directions and curvatures gave a unique visual representation of the spatial relationship between these variables which was not previously possible from separate in situ/DiI images. But thanks to the development of novel analytical tools this has been possible.

However, when these data were further probed for a consistent angular difference across the chiasm between the axon directions/curvatures and the mRNA gradients across different embryos, significance was only found for the angular difference between direction and Slit2 mRNA gradient. Ideally it would have been possible to measure both axon directions and protein/mRNA gradients in the same samples which may have yielded completely different results.

For comparison I shall now present the same analysis for the different Slit1 and Slit2 knockouts, but the results of the mean angular difference metric are hard to interpret as there was a fairly weak relationship for wildtype, so looking for a change in this relationship in the knockouts is perhaps a limited exercise.

5.2.2 $Slit1^{+/-};Slit2^{+/+}$

Figure 5.7 shows this same analysis for embryos of genotype $Slit1^{+/-};Slit2^{+/+}$. As was observed in the previous chapter the behaviour of axons of this genotype was very similar to wildtype, we see the regions axons enter with respect to the mRNA expression of Slit1 and Slit2 is equally similar to wildtype. Note that the expression patterns used here are the ones measured in wildtype mice, so presumably the $Slit1^{+/-};Slit2^{+/+}$ knockout has lower levels of Slit1 expression in this region, but despite this the axons appear to behave in a similar manner in this region (as was observed in the previous chapter). In line with this similarity to wildtype Figures 5.7 C and D are very similar to wildtype.

There was a significant (at the 5% level) result in the mean angular difference

across the chiasm between the axon directions and mRNA gradient of both Slit1 and Slit2 across samples (Figure 5.7E and F). The distribution and mean angle of the differences across samples was similar to wildtype and suggests again that the mean angular difference between axon direction and Slit1 is around 230° and with Slit2 is around 40°. However, there was no consistent mean angular difference between axon curvatures and the slit mRNA gradients (Figures 5.7 F-H). As in the wildtype the spread of angular differences is large.

5.2.3 $Slit1^{-/-};Slit2^{+/+}$

Here we see something that does look slightly different from wildtype. As can be seen in Figure 5.8B, more axons are entering a regions of high Slit2 than was observed in wildtype. In addition, the distribution of curvatures appears more balanced between left and right turns across the chiasm (Figure 5.8D), but given the randomness of the curvature directions in the posterior portion of the image caution should be applied.

Similar mean angular differences between axon direction and Slit1/Slit2 mRNA gradient as was observed in wildtype. In particular it is interesting that this relationship with respect to Slit1 should remain the same after complete removal of this gene. Again this supports the hypothesis that this may not be the more important of the two genes at this stage of development at the optic chiasm.

Again there was a large spread in the mean angular differences between curvature and mRNA gradient for the case of Slit1, but we see a more concentrated distribution in the case of Slit2 which is found to be significant at the 5% level. Here we observe that the gradient and curvatures are roughly aligned which is what would be expected if Slit2 was acting to repel axons.

5.2.4 $Slit1^{+/+};Slit2^{+/-}$

Again as previously observed in the last chapter the axon behaviours of this genotype appears to very similar to wildtype. Panels 5.9 A-D appear almost indistinguishable. In 5.9H we see that the mean angular difference difference between the mRNA gradient of Slit2 and the axon curvatures is significant across samples at the 5% level. Although here we do not see the same level of correlation with respect to direction (5.9E and F) as we did for the other genotypes.

5.2.5 $Slit1^{+/+};Slit2^{-/-}$

In Figure 5.10B there is a clear increase in the number of axons entering higher regions of Slit2 expression. In addition there appears to be a smaller range of orientations of the axons across the chiasm Figure 5.10C compared with wildtype, and the distribution of curvatures appears to have shifted to the opposite direction 5.10D.

Again there appears to be mixed results when it comes calculating the mean angular differences between the axon directions/curvatures and the mRNA gradients. Here we find significance for the mean angular difference between the Slit2 mRNA gradient and the axon direction (Figure 5.10F). This again is slightly confusing as the correlation has increased despite knocking out that gene.

5.2.6 $Slit1^{+/-};Slit2^{+/-}$

Figure 5.11 shows the overlaid axon directions and curvatures onto the mRNA gradients of Slit1 and Slit2 (A and B), here the axons appear to take a much tighter turn at the midline than in the wildtype. In C and D the histograms of the axon directions and curvatures are similar to those found in the wildtype. Presumably due to the low n-number for this genotype (3 samples) none of the mean angular differences were found to have significance.

5.2.7 $Slit1^{-/-};Slit2^{+/-}$

Figures 5.12 A and B show that the overall spread of axons over the chiasm regions appears to have increased compared to wildype, but that axons still avoid the region of high Slit2 expression in B as they did in the $Slit1^{+/+};Slit2^{+/-}$ genotype.

Looking at the mean angular differences across the chiasm between mRNA gradient and axon directions/curvatures we again see greater correlation with respect to the direction than with respect to the curvature. Interestingly these correlations are centred around 200° for the Slit1 gradient and 30° for the Slit2 gradient, very similar to wildtype. This is interesting as only one copy of Slit2 is present in this animal (and none of Slit1) and despite this there is little variation from wildtype with respect to both axon directions/curvatures and also there relationship with the slit gradients.

5.2.8 $Slit1^{-/-};Slit2^{-/-}$

As studied in the previous chapter the spread of axons is much higher in the wildtype than in the this $Slit1^{-/-};Slit2^{-/-}$ mutant and we see far more axons entering the regions where there would normally be high Slit2 expression (Figure 5.13B). We also see a larger spread of axon directions as we also noted in the previous chapter (Figure 5.13C).

Most confusingly there appears to be the highest degree of correlation with respect to the mean angular differences between the mRNA gradients and the axon directions/curvatures. We find significance in all four tests: 5.13E-H. This is very counter-intuitive as these genes are no longer expressed so it would have been expected that as genes were knocked out the mean angular difference would either become uncorrelated and/or for the mean angular difference to change from wildtype. However, none of these things were seen, yet there clearly is a difference in the axon behaviours of these various genotypes as was demonstrated in the previous chapter. It is suggested that this metric is perhaps too crude and that this is more a measure of variability of

axon directions/curvatures within a genotype than a measure of any ubiquitous angular relationship between the gradient and axon directions/curvatures across the optic chiasm.

5.3 Spatial analysis of the gradient/curvature parity at the optic chiasm

Having looked at the relationship between the different vector fields averaged over the whole optic chiasm, I now look at how this relationship may change across the extent of the chiasm. At each point in the chiasm I calculated the cosine of the angle between the curvature and the gradient ($\cos\theta$ in Figure 5.14). $\cos\theta$ will be 1 for two vectors exactly parallel, -1 for vectors exactly anti-parallel or 0 for vectors that are perpendicular.

I refer to this metric as the parity between the curvature and the gradient. The result of calculating the parity between curvature and gradient across the chiasm is shown in Figures 5.15 and 5.16, for Slit1 and Slit2 respectively. Figure 5.15A, shows this metric for wildtype. There are well defined areas of the chiasm where the two vectors fields are parallel (positive regions/warm colours) to each other and areas where they are anti-parallel (negative regions/cool colours). In particular there appears to be an area along the midline, in the posterior part of the chiasm (around (0.5,-0.2) in universal co-ordinates), where the curvature of the axons appear to be parallel to the gradient, an effect that begins to be reversed in the heterozygous knockout of Slit1 (Figure 5.15B), and is almost completely obliterated in the complete knockout of Slit1 (Figure 5.15C). The same trend is observed in Figures 5.15D-E as Slit1 is removed from the heterozygous knockout of Slit2. This suggests the role of Slit1 may be to turn axons in an anterior direction at this point in the chiasm. This may be the reason I did not detect a phenotype in the previous section in the case of the Slit1 knockout, because the effect is confined to a small area of the chiasm. In addition, both the

$Slit1^{+/+};Slit2^{-/-}$ and $Slit1^{-/-};Slit2^{-/-}$ knockouts (Figures 5.15G and H) appear to have a far more complex relation between the gradient and curvature, suggesting the axons are turning in random directions without ordered outside influence.

In the case of the gradient of Slit2 (Figure 5.16) there is an even more striking reversal of the parity of the curvature and the gradient. In the wildtype chiasm (Figure 5.16A), we see a roughly anti-parallel, parallel, anti-parallel change across the image. This is completely reversed in the $Slit1^{+/+};Slit2^{-/-}$, and is disrupted further still in the case of the double knockout. These effects are presumably the result of the lack of the Slit2, causing the axons to turn in the opposite direction than was found in the wildtype.

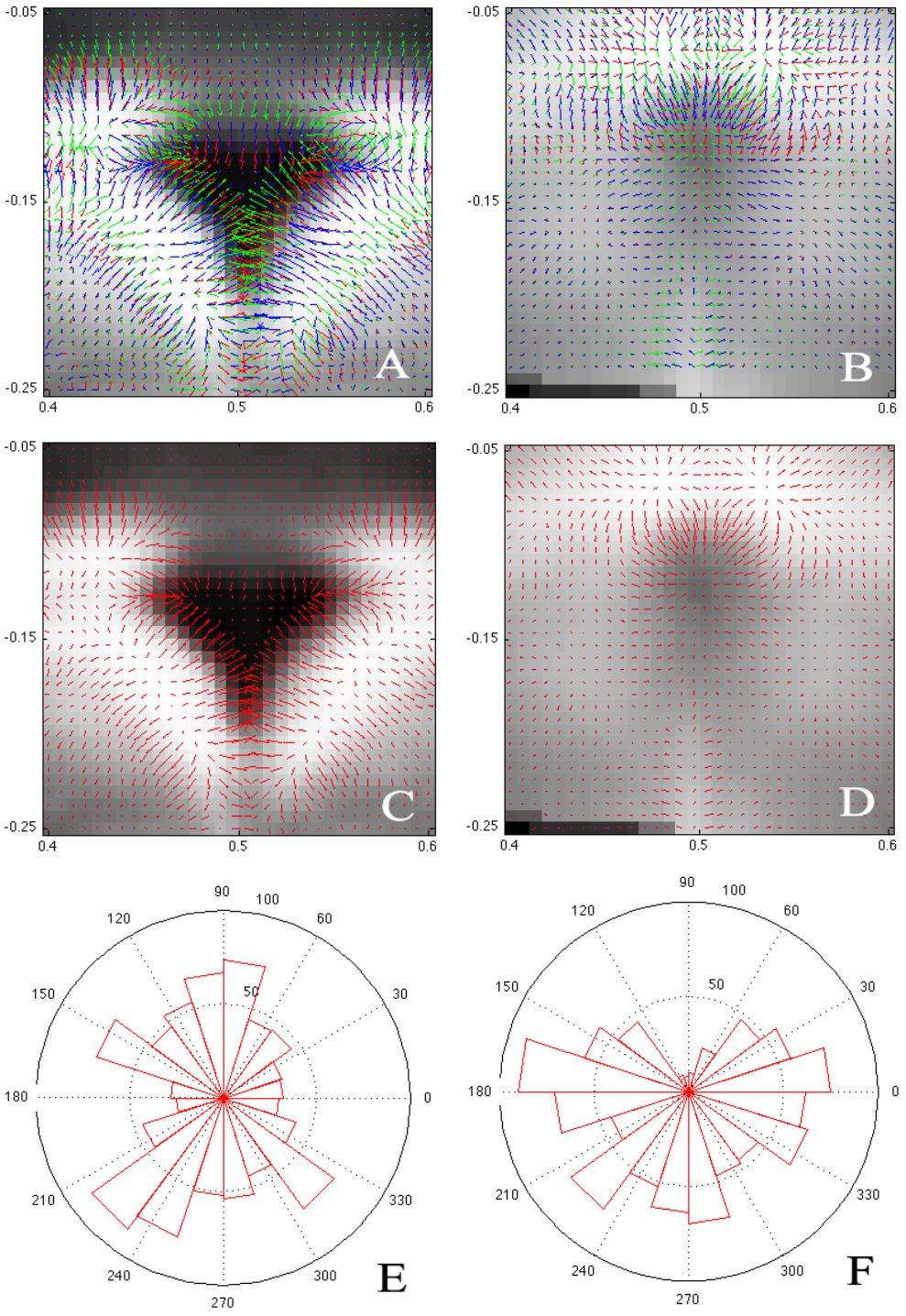

Figure 5.4: The gradient of Slit1 and Slit2 as derived from in situ hybridisation. A and B show the overlaid gradients from Slit1 and Slit2 respectively, from each of three samples for both Slit1 and Slit2. Each arrow colour represents the gradient from a different in situ sample, and the underlying image in each is the average pixel intensity over all samples at each grid point. C and D show the averaged gradient of Slit1 and Slit2 respectively. E and F show the circular histogram of the direction of the gradient across the chiasm for Slit1 and Slit2 respectively.

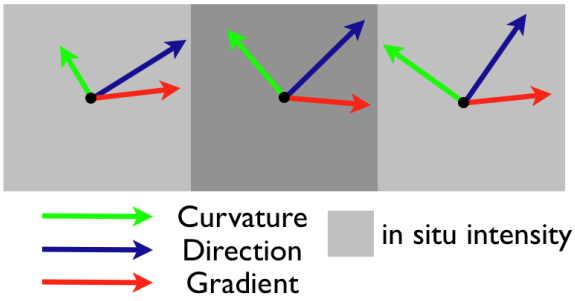

Figure 5.5: Key for Figures 5.6 to 5.13.

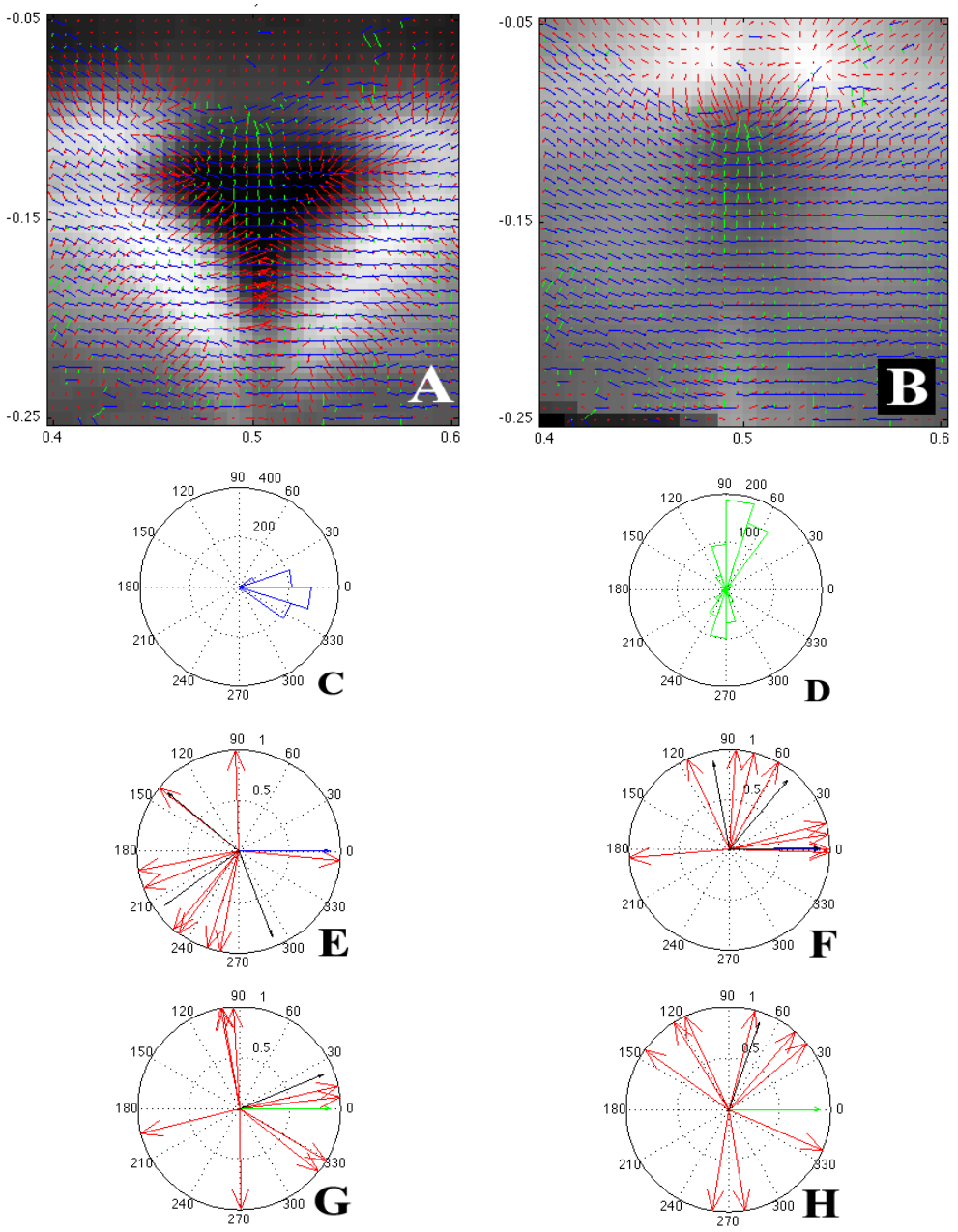

Figure 5.6: A and B: Overlaying the directional (blue) and curvature (green) vector fields of $Slit1^{+/+}$;$Slit2^{+/+}$ axons onto the mRNA gradient (red) of Slit1 and Slit2 respectively. C and D: Histograms of direction and curvature respectively. E and F: Mean angular difference across image between the mRNA gradients of Slit1 (E) and Slit2 (F) and axon directions for each embryo (red arrows). Direction plotted at 0° (blue arrow) for reference. The mean over all samples and 95% confidence intervals is denoted by the black arrows. Rayleigh test for significant difference from uniform distribution gave p-values of: p = 0.13 for Slit1, p = 0.04 for Slit2. G and H: Mean angular difference across image between mRNA gradient and axon curvatures for each embryo. Curvature always plotted at 0° (blue arrow) for reference. Rayleigh test gave p-values of: p = 0.53 for Slit1, p = 0.52 for Slit2.

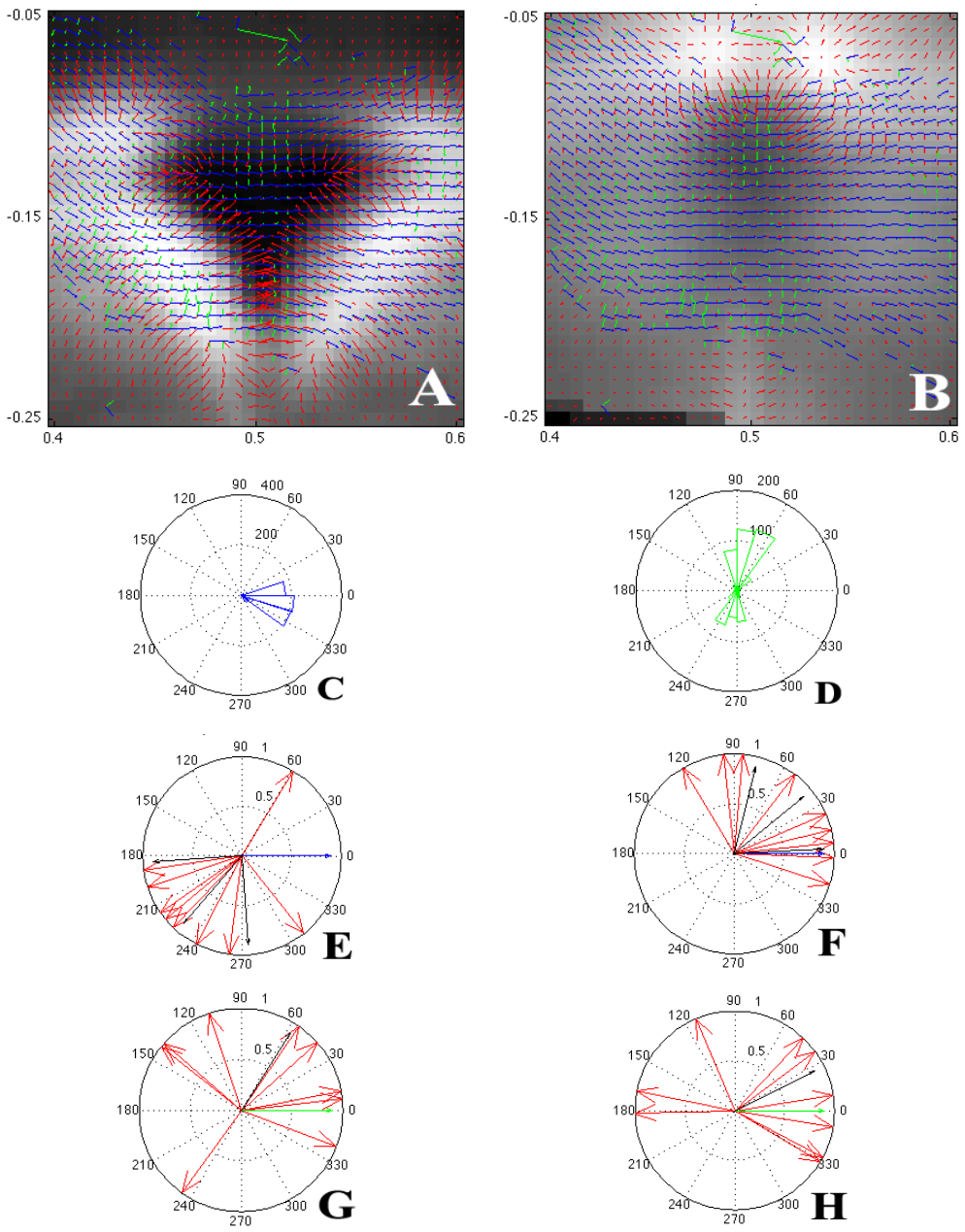

Figure 5.7: A and B: Overlaying the directional (blue) and curvature (green) vector fields of $Slit1^{+/-}$;$Slit2^{+/+}$ axons onto the mRNA gradient (red) of Slit1 and Slit2 respectively. C and D: Histograms of direction and curvature respectively. E and F: Mean angular difference across image between the mRNA gradients of Slit1 (E) and Slit2 (F) and axon directions for each embryo (red arrows). Direction plotted at 0° (blue arrow) for reference. The mean over all samples and 95 % confidence intervals is denoted by the black arrows. Rayleigh test for significant difference from uniform distribution gave p-values of: p = 0.03 for Slit1, p = 0.008 for Slit2. G and H: Mean angular difference across image between mRNA gradient and axon curvatures for each embryo. Curvature always plotted at 0° (blue arrow) for reference. Rayleigh test gave p-values of: p = 0.30 for Slit1, p = 0.33 for Slit2.

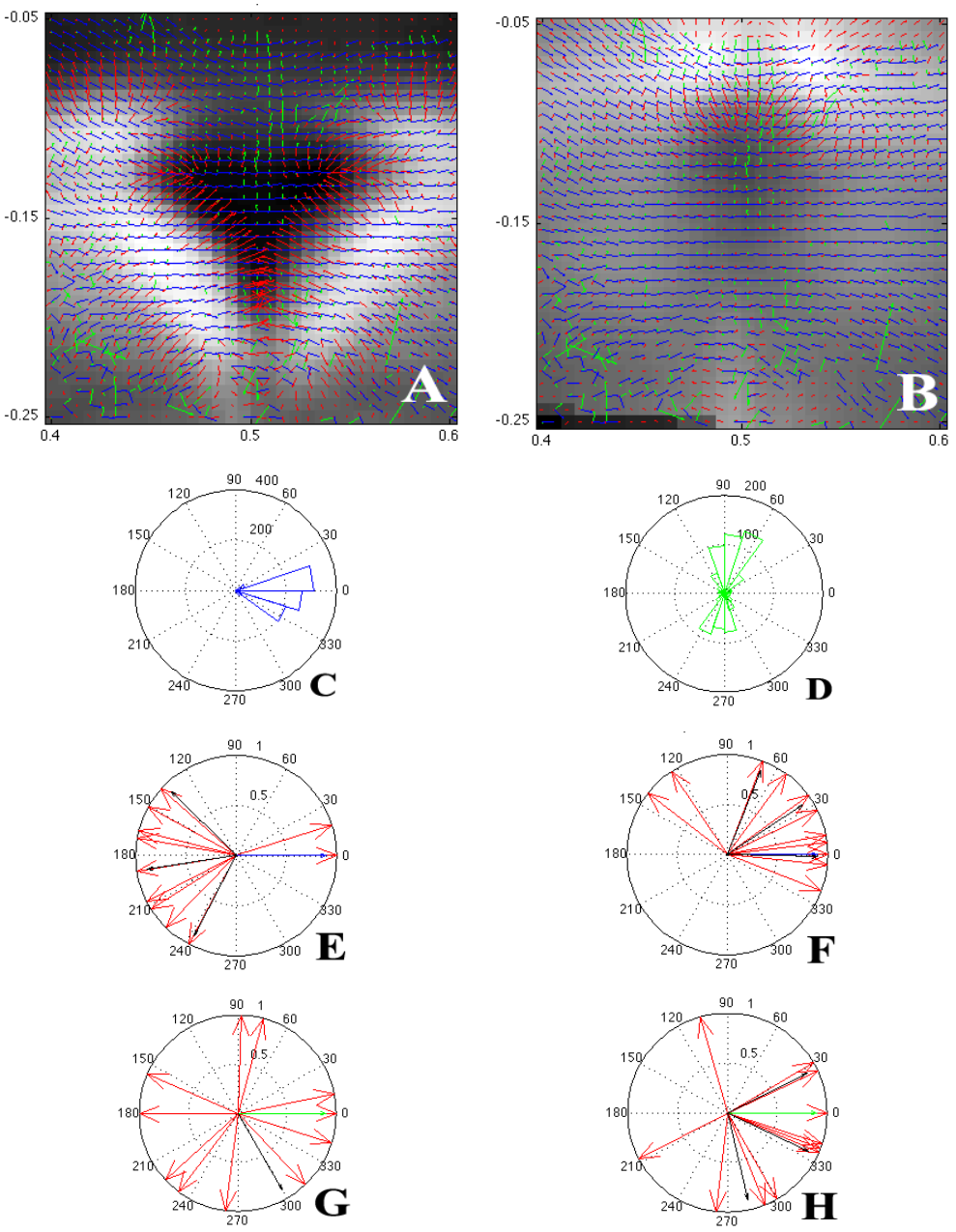

Figure 5.8: A and B: Overlaying the directional (blue) and curvature (green) vector fields of $Slit1^{-/-};Slit2^{+/+}$ axons onto the mRNA gradient (red) of Slit1 and Slit2 respectively. C and D: Histograms of direction and curvature respectively. E and F: Mean angular difference across image between the mRNA gradients of Slit1 (E) and Slit2 (F) and axon directions for each embryo (red arrows). Direction plotted at 0° (blue arrow) for reference. The mean over all samples and 95 % confidence intervals is denoted by the black arrows. Rayleigh test for significant difference from uniform distribution gave p-values of: p = 0.06 for Slit1, p = 0.004 for Slit2. G and H: Mean angular difference across image between mRNA gradient and axon curvatures for each embryo. Curvature always plotted at 0° (blue arrow) for reference. Rayleigh test gave p-values of: p = 0.90 for Slit1, p = 0.04 for Slit2.

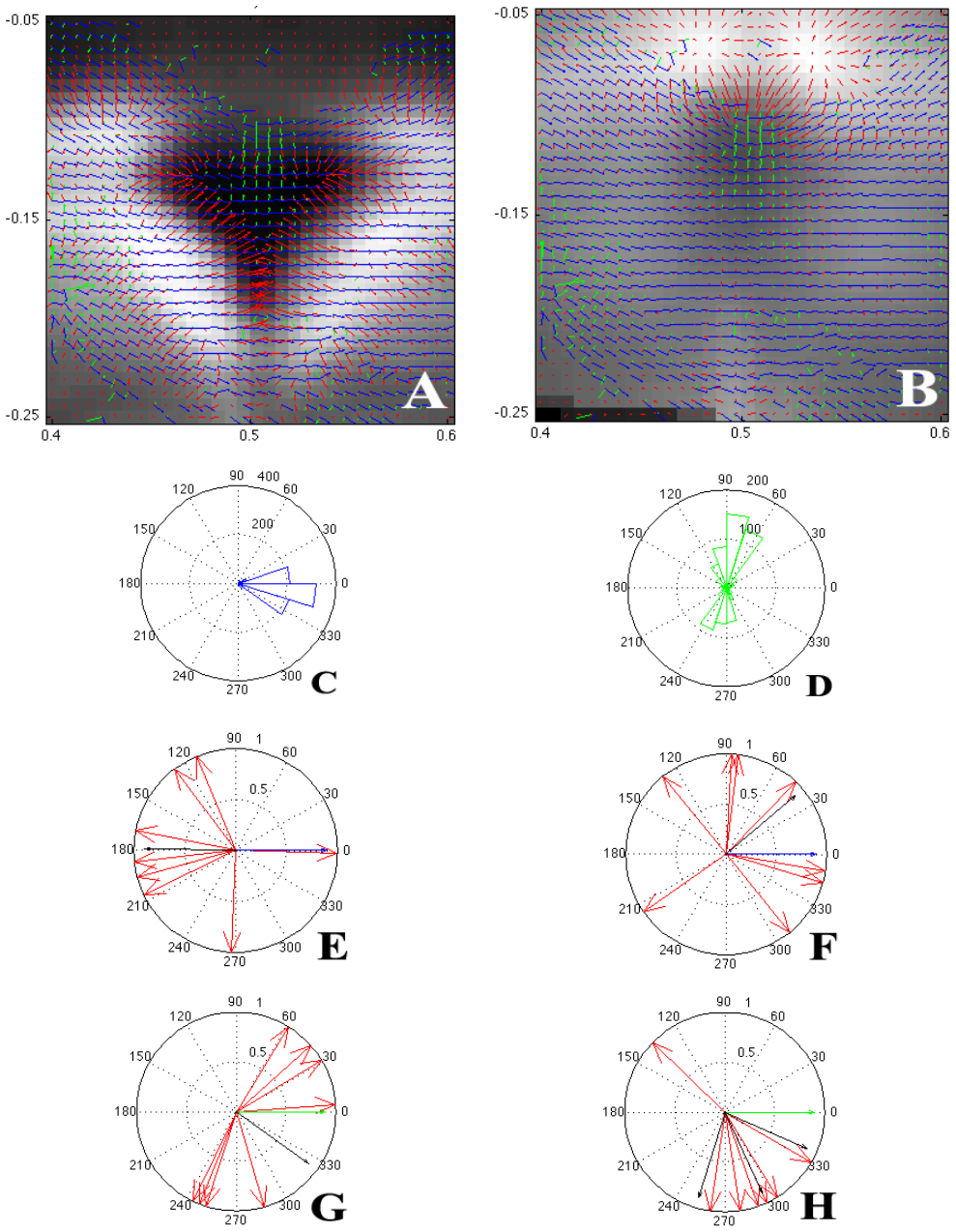

Figure 5.9: A and B: Overlaying the directional (blue) and curvature (green) vector fields of $Slit1^{+/+}$;$Slit2^{+/-}$ axons onto the mRNA gradient (red) of Slit1 and Slit2 respectively. C and D: Histograms of direction and curvature respectively. E and F: Mean angular difference across image between the mRNA gradients of Slit1 (E) and Slit2 (F) and axon directions for each embryo (red arrows). Direction plotted at 0° (blue arrow) for reference. The mean over all samples and 95 % confidence intervals is denoted by the black arrows. Rayleigh test for significant difference from uniform distribution gave p-values of: p = 0.15 for Slit1, p = 0.44 for Slit2. G and H: Mean angular difference across image between mRNA gradient and axon curvatures for each embryo. Curvature always plotted at 0° (blue arrow) for reference. Rayleigh test gave p-values of: p = 0.38 for Slit1, p = 0.02 for Slit2.

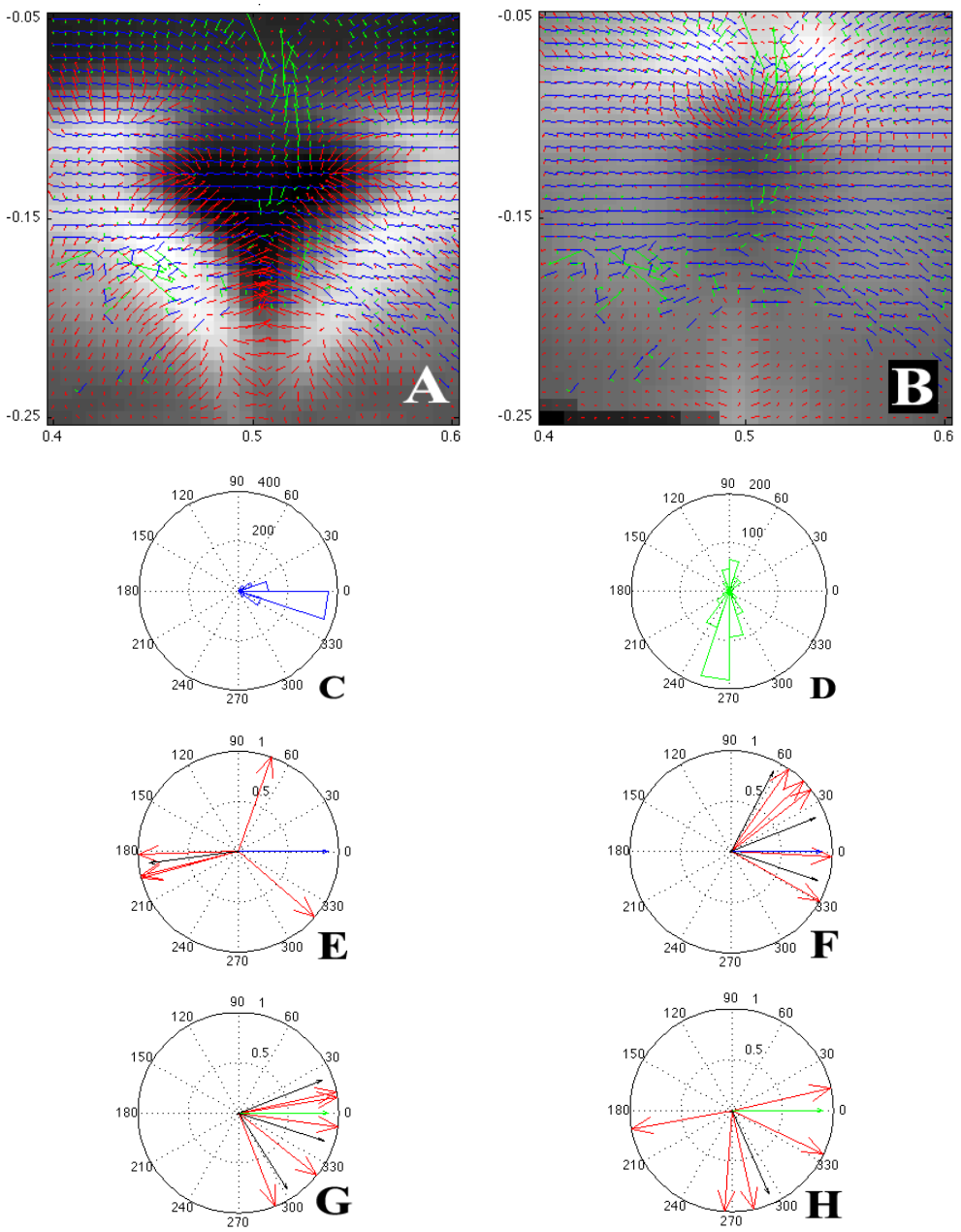

Figure 5.10: A and B: Overlaying the directional (blue) and curvature (green) vector fields of $Slit1^{+/+};Slit2^{-/-}$ axons onto the mRNA gradient (red) of Slit1 and Slit2 respectively. C and D: Histograms of direction and curvature respectively. E and F: Mean angular difference across image between the mRNA gradients of Slit1 (E) and Slit2 (F) and axon directions for each embryo (red arrows). Direction plotted at 0° (blue arrow) for reference. The mean over all samples and 95 % confidence intervals is denoted by the black arrows. Rayleigh test for significant difference from uniform distribution gave p-values of: p = 0.52 for Slit1, p = 0.02 for Slit2. G and H: Mean angular difference across image between mRNA gradient and axon curvatures for each embryo. Curvature always plotted at 0° (blue arrow) for reference. Rayleigh test gave p-values of: p = 0.02 for Slit1, p = 0.27 for Slit2.

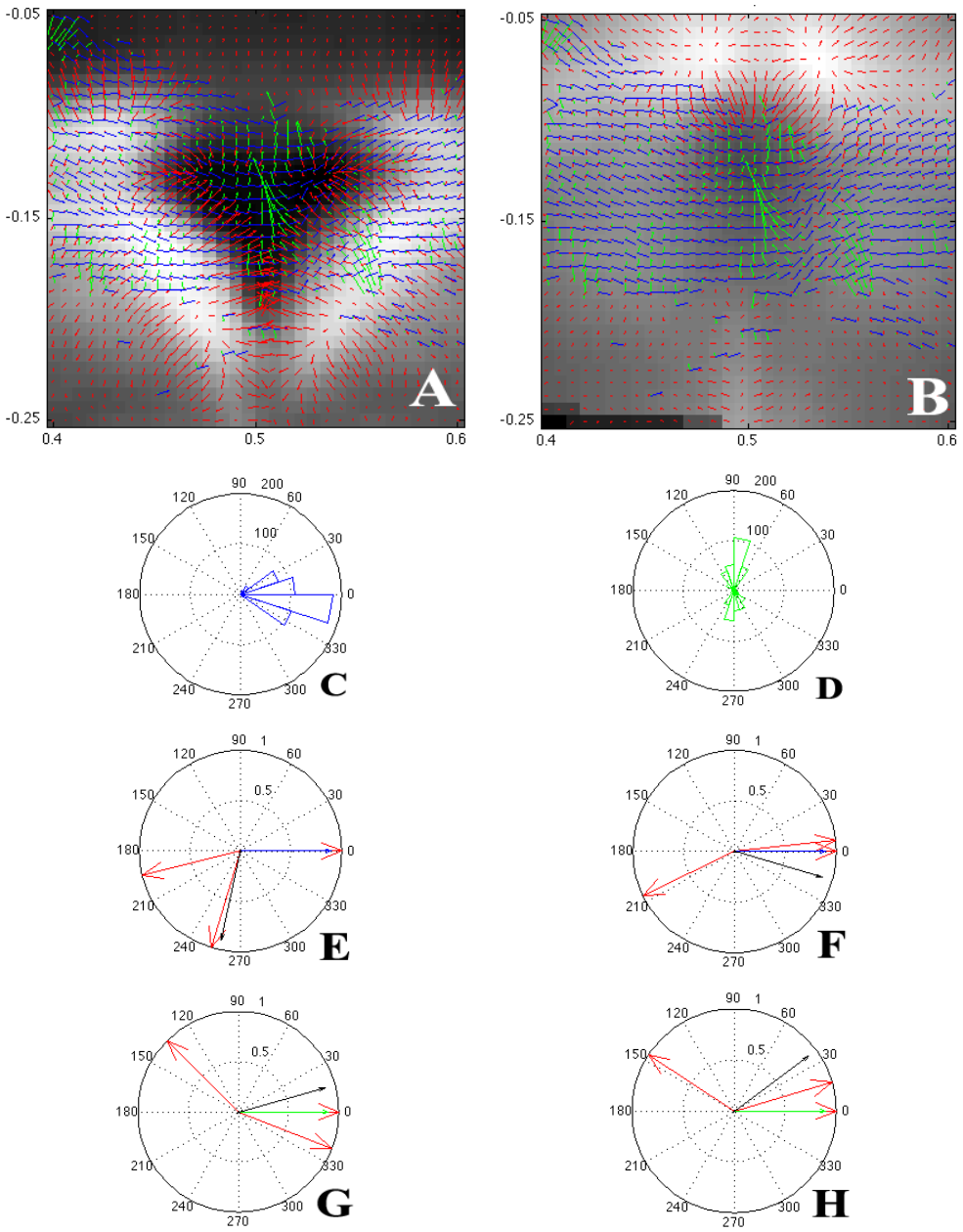

Figure 5.11: A and B: Overlaying the directional (blue) and curvature (green) vector fields of $Slit1^{+/-}$;$Slit2^{+/-}$ axons onto the mRNA gradient (red) of Slit1 and Slit2 respectively. C and D: Histograms of direction and curvature respectively. E and F: Mean angular difference across image between the mRNA gradients of Slit1 (E) and Slit2 (F) and axon directions for each embryo (red arrows). Direction plotted at 0° (blue arrow) for reference. The mean over all samples and 95 % confidence intervals is denoted by the black arrows. Rayleigh test for significant difference from uniform distribution gave p-values of: p = 0.64 for Slit1, p = 0.68 for Slit2. G and H: Mean angular difference across image between mRNA gradient and axon curvatures for each embryo. Curvature always plotted at 0° (blue arrow) for reference. Rayleigh test gave p-values of: p = 0.62 for Slit1, p = 0.56 for Slit2.

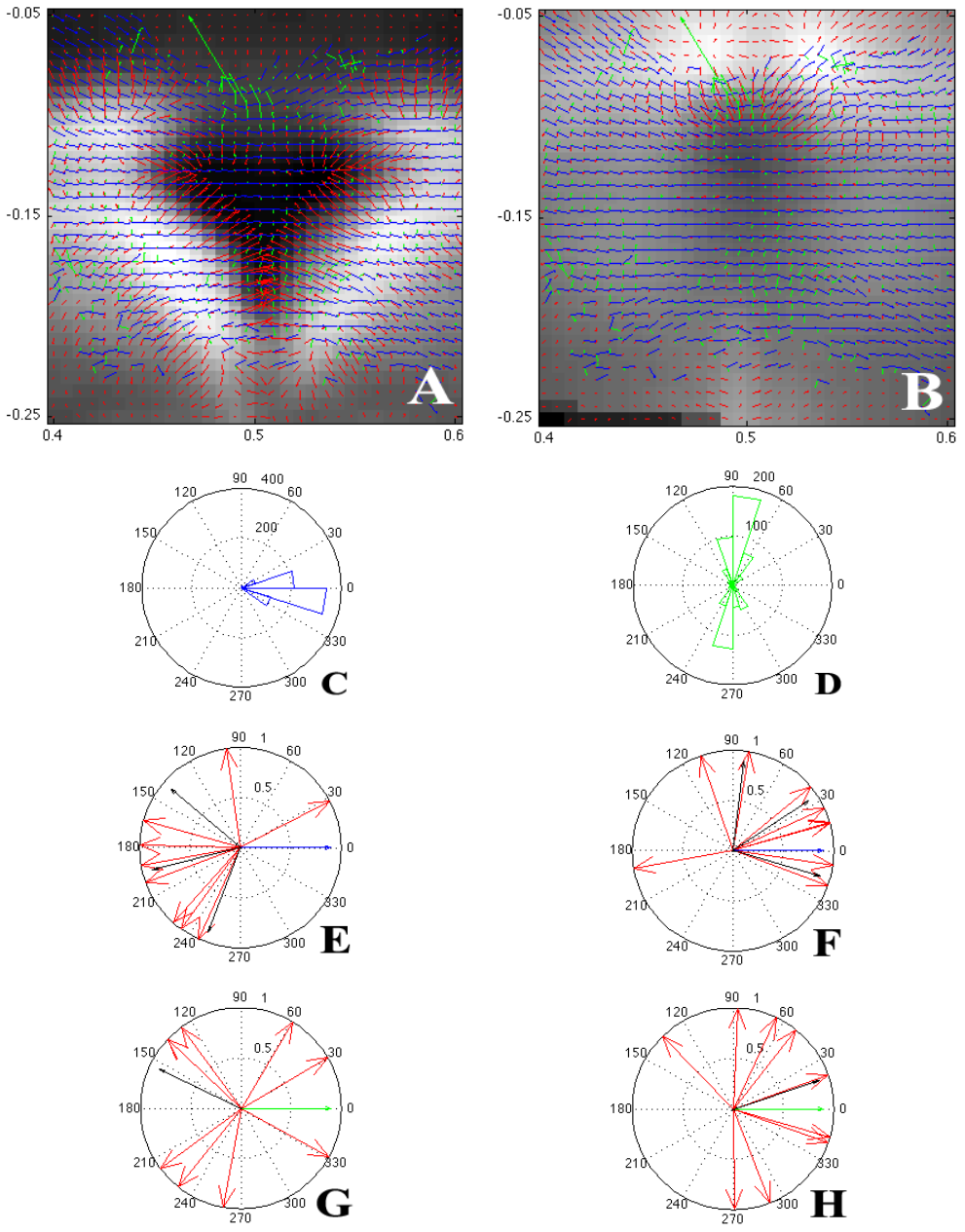

Figure 5.12: A and B: Overlaying the directional (blue) and curvature (green) vector fields of $Slit1^{-/-}$;$Slit2^{+/-}$ axons onto the mRNA gradient (red) of Slit1 and Slit2 respectively. C and D: Histograms of direction and curvature respectively. E and F: Mean angular difference across image between the mRNA gradients of Slit1 (E) and Slit2 (F) and axon directions for each embryo (red arrows). Direction plotted at 0° (blue arrow) for reference. The mean over all samples and 95 % confidence intervals is denoted by the black arrows. Rayleigh test for significant difference from uniform distribution gave p-values of: p = 0.06 for Slit1, p = 0.04 for Slit2. G and H: Mean angular difference across image between mRNA gradient and axon curvatures for each embryo. Curvature always plotted at 0° (blue arrow) for reference. Rayleigh test gave p-values of: p = 0.77 for Slit1, p = 0.20 for Slit2.

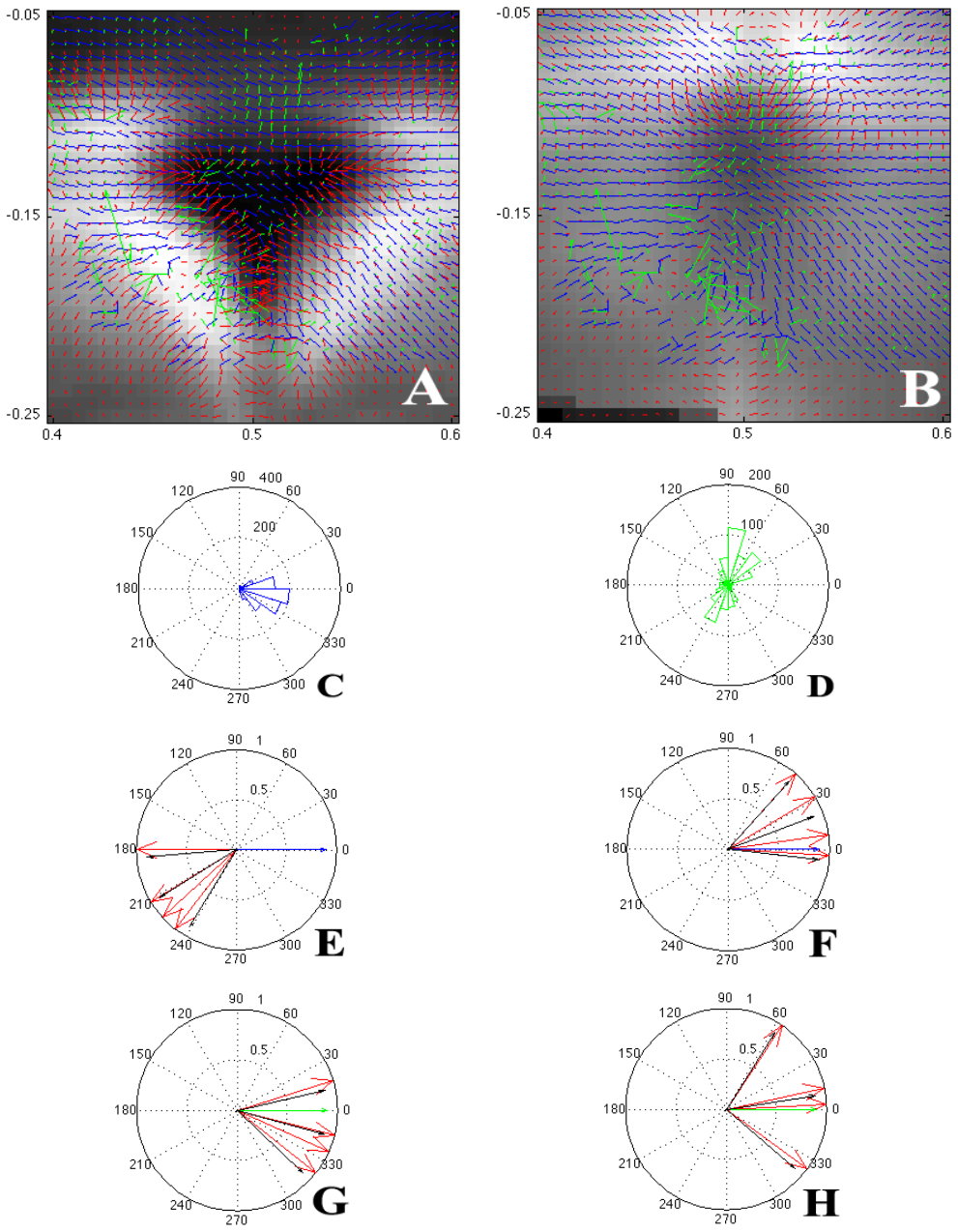

Figure 5.13: A and B: Overlaying the directional (blue) and curvature (green) vector fields of $Slit1^{-/-}$;$Slit2^{-/-}$ axons onto the mRNA gradient (red) of Slit1 and Slit2 respectively. C and D: Histograms of direction and curvature respectively. E and F: Mean angular difference across image between the mRNA gradients of Slit1 (E) and Slit2 (F) and axon directions for each embryo (red arrows). Direction plotted at 0° (blue arrow) for reference. The mean over all samples and 95 % confidence intervals is denoted by the black arrows. Rayleigh test for significant difference from uniform distribution gave p-values of: p = 0.02 for Slit1, p = 0.02 for Slit2. G and H: Mean angular difference across image between mRNA gradient and axon curvatures for each embryo. Curvature always plotted at 0° (blue arrow) for reference. Rayleigh test gave p-values of: p = 0.02 for Slit1, p = 0.05 for Slit2.

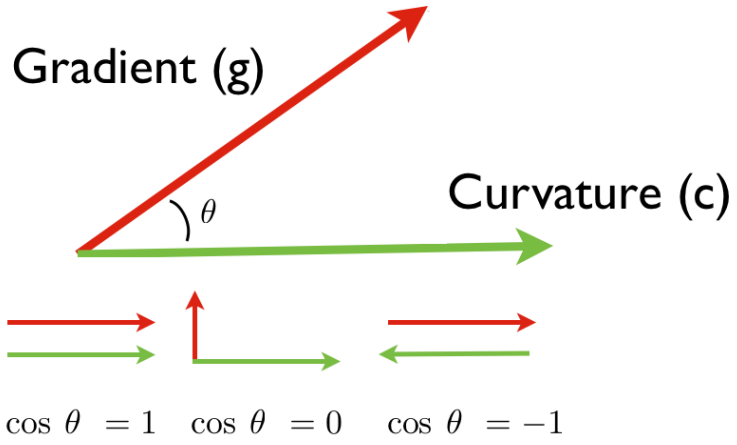

Figure 5.14: Relation between gradient and curvature. The cosine of the angle between the two vectors represents either parallel vectors ($\cos\theta = 1$), anti-parallel ($\cos\theta = -1$) or perpendicularity ($\cos\theta = 0$)

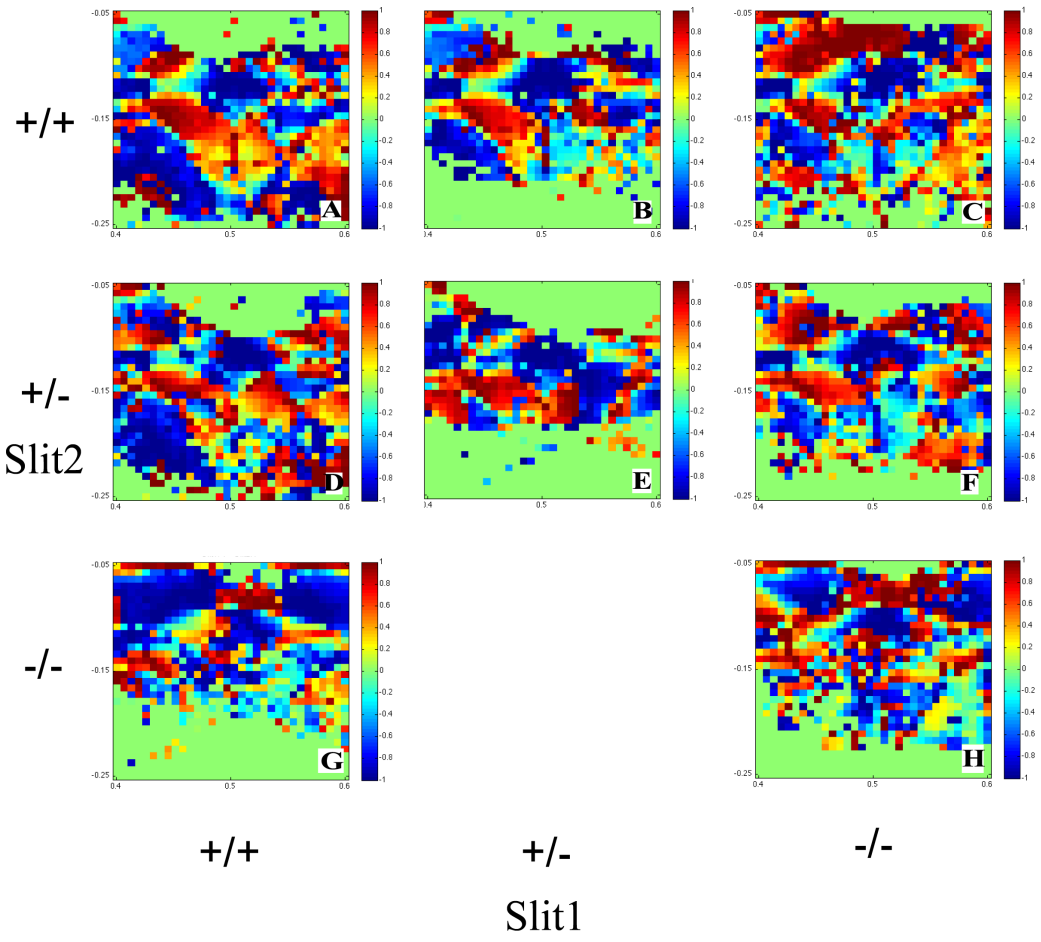

Figure 5.15: Spatial distribution of the cosine of the angle between the gradient of Slit1 and the direction of curvature of the axons (1 means parallel, 0 perpendicular, -1 anti-parallel). This demonstrates that Slit1 may have a dual affect on axon growth, with spatial dependence.

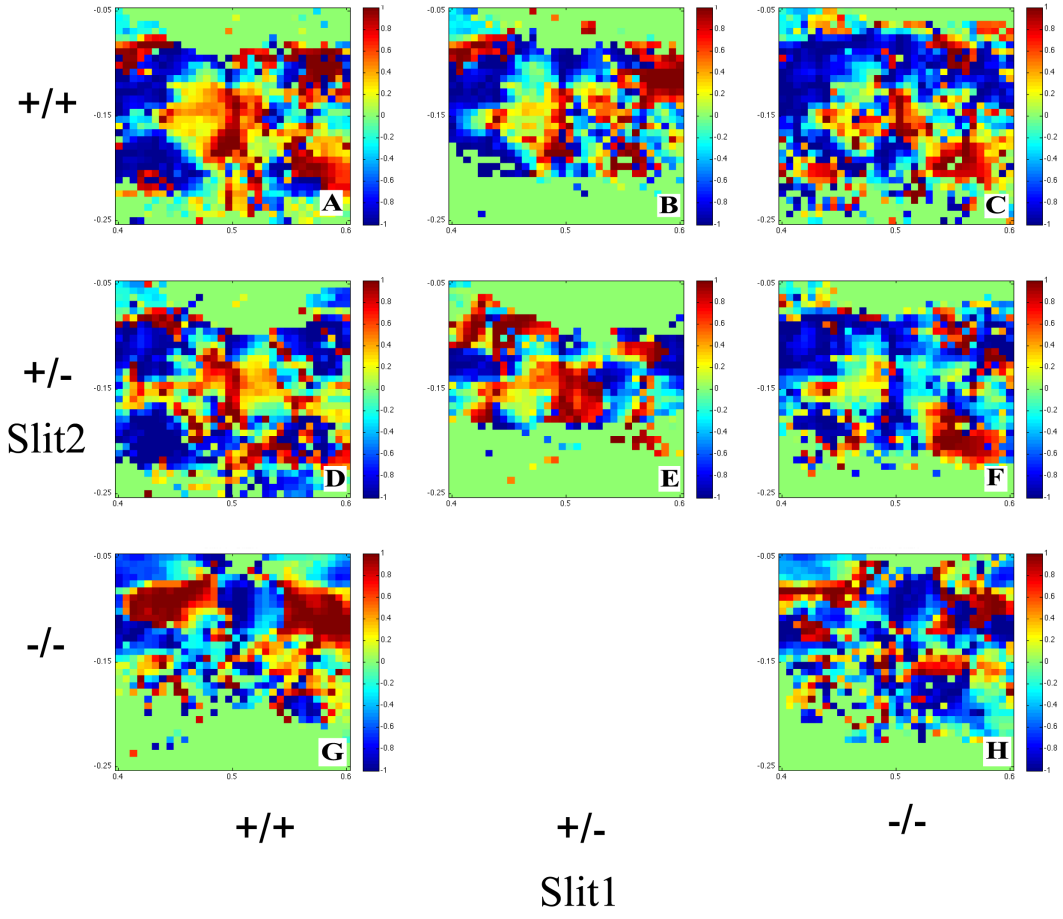

Figure 5.16: Spatial distribution of the cosine between Slit2 and the curvature of the axons (1 means parallel, 0 perpendicular, -1 anti-parallel). This demonstrates that Slit2 may have a dual affect on axon growth, with spatial dependence.

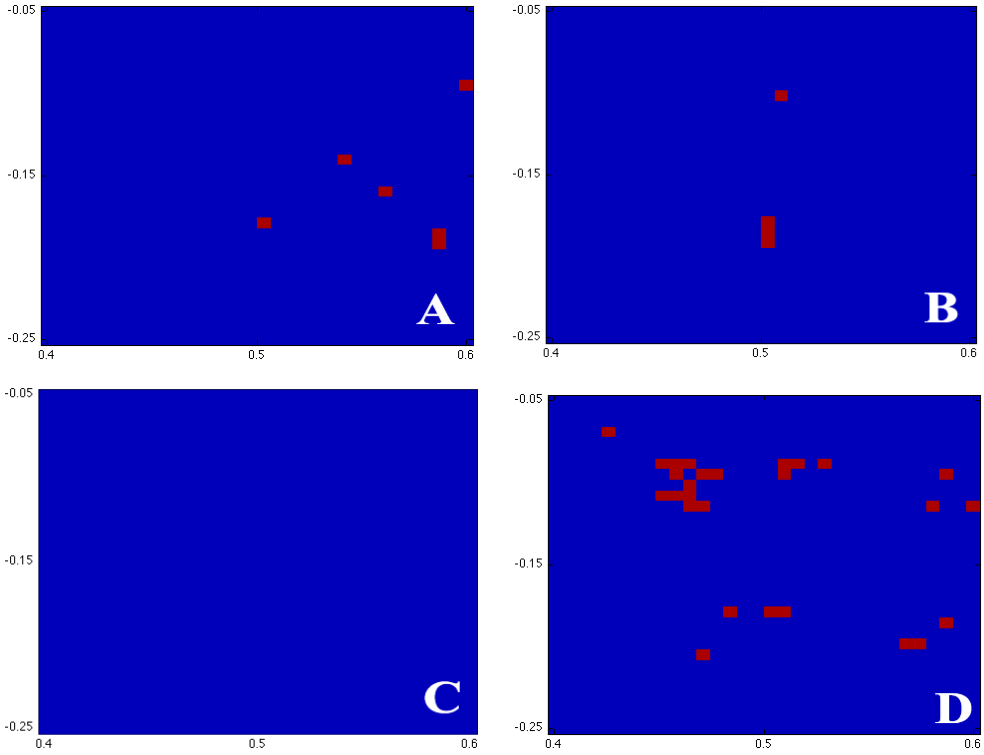

Figure 5.17: Areas of the chiasm whose gradient/curvature parity alter significantly from wildtype using the FDR technique with $\alpha = 0.05$ to control false positives, red indicates significance. A and B heterozygous and homozygous knockout of Slit1 respectively. C and D heterozygous and homozygous knockout of Slit2 respectively.

To test if there are significant differences across the optic chiasm in the parity of the gradient/curvature a students t-test was performed, and false positives were controlled for by using FDR as in the previous chapter. The results for the knockouts of just one of the genes is shown in Figure 5.17 ($\alpha = 0.05$). The regions that are deemed significant in the $Slit1^{+/-};Slit2^{+/+}$ and $Slit1^{-/-};Slit2^{+/+}$ appear to occur sporadically across the image, with no clear pattern or clustering. In the $Slit1^{+/+};Slit2^{+/-}$ (Figure 5.17C) no region of the optic chiasm shows significance from wildtype, but in the $Slit1^{+/+};Slit2^{-/-}$ (Figure 5.17D) there appears to be a clustered region close to the steepest part of the Slit2 gradient (around (0.25,-0.1) in universal co-ordinates) where the curvature-gradient parity does change significantly from wildtype, indicating again this key area of slit-dependent axon guidance at the optic chiasm.

5.4 Comparing mutant/wildtype axon curvature differences with the gradients of Slit1 and Slit2

I now look at the difference in the curvatures between the wildtype and mutants, and compare it with the gradient. As described in Chapter 2, it is my hypothesis that this change in curvature should be due to the reduced action of the gradient of the respective guidance cue in the knockout embryo. This suggests that this difference in curvature should align with the gradient if it is a negative cue, or should be anti-parallel if it is a positive cue. The hypothesis is that the vectors will be aligned and their relatives magnitudes consistently in proportion, with the constant of proportionality indicative of the strength of that guidance cue. I will first test if the vector are aligned by comparing the angles. I shall then test if there is a proportionality relationship between the vectors by comparing their magnitudes.

5.4.1 Comparing the angles between the gradient and curvature difference.

In this section I compare the angle between the Slit1/Slit2 mRNA gradients and curvature changes from wildtype. The change in curvature is denoted by $C_{+/+} - C_{-/-}$ and the gradient by G. The relation between these vectors is shown schematically in Figure 5.18. These results are shown in Figure 5.19. Although we might have expected the difference in curvature and the gradient to line up (i.e. the mean to be centred on 0°, as in Figure 5.18), here there are mixed results, such as an apparent bimodal distribution in the case of $Slit1^{+/-}; Slit2^{+/+}$ (Figure 5.19A), with 2/3 of the embryos doing as predicted and the other 1/3 doing the direct opposite and a uniform distribution in the case of the full knockout $Slit1^{-/-}; Slit2^{+/+}$ (Figure 5.19B). Neither showed significance at the 5% level. In the $Slit1^{+/+}; Slit2^{+/-}$ knockout there was significance at the 5% level (Figure 5.19C), and a large number of embryos did lie close to zero degrees as expected. However, in the complete knockout of Slit2 (Figure 5.19D) a mixed result was observed, although I only generated 5 embryos of this genotype so finding significance was always unlikely.

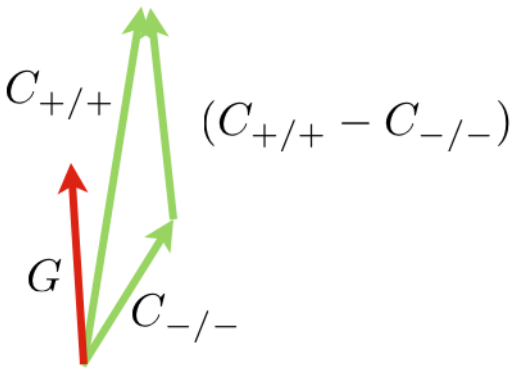

Figure 5.18: This schematic diagram shows the predicted relationship between the vectors $C_{+/+}$, $C_{-/-}$ and the gradient G

5.4.2 Looking at the relationship between the magnitude of trajectory curvature difference and the gradient.

In this section I investigate the hypothesis that the difference in the curvatures between wildtype and mutant will be proportional to the missing gradient that would have presumably caused such a change. Figure 5.20 shows the proportional relationship is not there as expected; instead the relationship appears to be somewhat random. This is another indicator that there is no simple relationship between the mRNA gradients of the slits and the change in curvature due to the departure of the slit gradient in the knockout. Looking at the norm of the residuals from linear regression, in each case it is very close to zero, indicating there is neither positive nor negative correlation between the two.

5.5 Examining the product of axon number and In Situ intensity across genotypes

In light of the mixed evidence obtained regarding the relationship between the gradient of the Slits and the directional/curvature vector fields of the axons, I applied a very simple metric to see if I could use the expression patterns of Slit1 and Slit2 to explain the knockout phenotype seen in the previous chapter. I calculated the following metric:

$$k = \frac{\sum_{\mathbf{grid}}[N_{\text{axons}} \times I_{\text{InSitu}}]}{\sum_{\mathbf{grid}}[N_{\text{axons}}]} \tag{5.1}$$

Where N_{axons} is the number of axons per grid square and I_{InSitu} is the intensity of the In Situ at that point. The metric k then represents a measure of the relative proportion of axons that are entering regions of high Slit expression. We expect this value to be higher for the knockout case, where the underlying Slit is no longer present.

The result of this metric is shown in Figures 5.21 and 5.22 comparing knockout chiasms with wildtype. Figure 5.21 shows that both the $Slit1^{+/+};Slit2^{-/-}$ and the

$Slit1^{-/-};Slit2^{-/-}$ have significantly higher axon density in ares of high Slit1 expression than wildtype. Figure 5.22 shows that only $Slit1^{+/+};Slit2^{-/-}$ has significantly lower axon density in high regions of Slit2 expression. This is perhaps counter-intuitive as I might have expected that there would be higher axon density in regions that should have had high Slit2 expression in the knockout of the Slit2 gene.

These results do not paint a clear picture of the spatial functional role of the slits at the optic chiasm. The reason no simple conclusions can be made may be due to measuring the gradient of the mRNA expression of the slits and not the actual protein gradient. Another reason may be tissue distortion. As can be seen in Figure 5.23 there is a marked difference in the eye width between embryos that were used for DiI experiments and those used for in situs. This difference is probably as a result of the different tissue processing steps in the two protocols. This may have resulted in inaccuracies, although these were controlled for by aligning each sample to a universal grid.

5.6 Chapter Summary

In this chapter I have used in situ hybridisation in order to visualise the expression pattern of Slit1 and Slit2 and from this I have calculated the mRNA gradient across the optic chiasm. I have averaged and aligned this gradient data onto a universal grid in order to compare with the axon directions and curvatures of the wildtype and knockout mice. The idea is that the phenotypic difference seen in the previous chapter may be explained by the mRNA gradients of Slit1 and Slit2.

I first looked at the mean angular difference between the axon directions/curvatures and the mRNA gradient across the chiasm. This gave weak results for wildtype but confusingly gave stronger results for some of the knockouts. I then looked at the spatial change in the parity between axon direction/curvature and the gradient across the chiasm. This revealed some sporadic significant differences from wildtype but

none that had a simple interpretation.

The curvature difference between wildtype and knockout was compared with the mRNA gradient and both the angle and magnitude. The distribution of angles were not any different from a uniform distribution and the magnitudes of these vectors were uncorrelated.

Finally a metric was created to measure the tendency for axons to enter regions of high slit expression compared with wildtype. It was found that in the $Slit1^{+/+};Slit2^{-/-}$ and $Slit1^{-/-};Slit2^{-/-}$ mutants axons proportionally entered regions of high Slit1 expression and in the $Slit1^{+/+};Slit2^{-/-}$ mutant a greater proportion of axons avoided regions of high Slit2 expression.

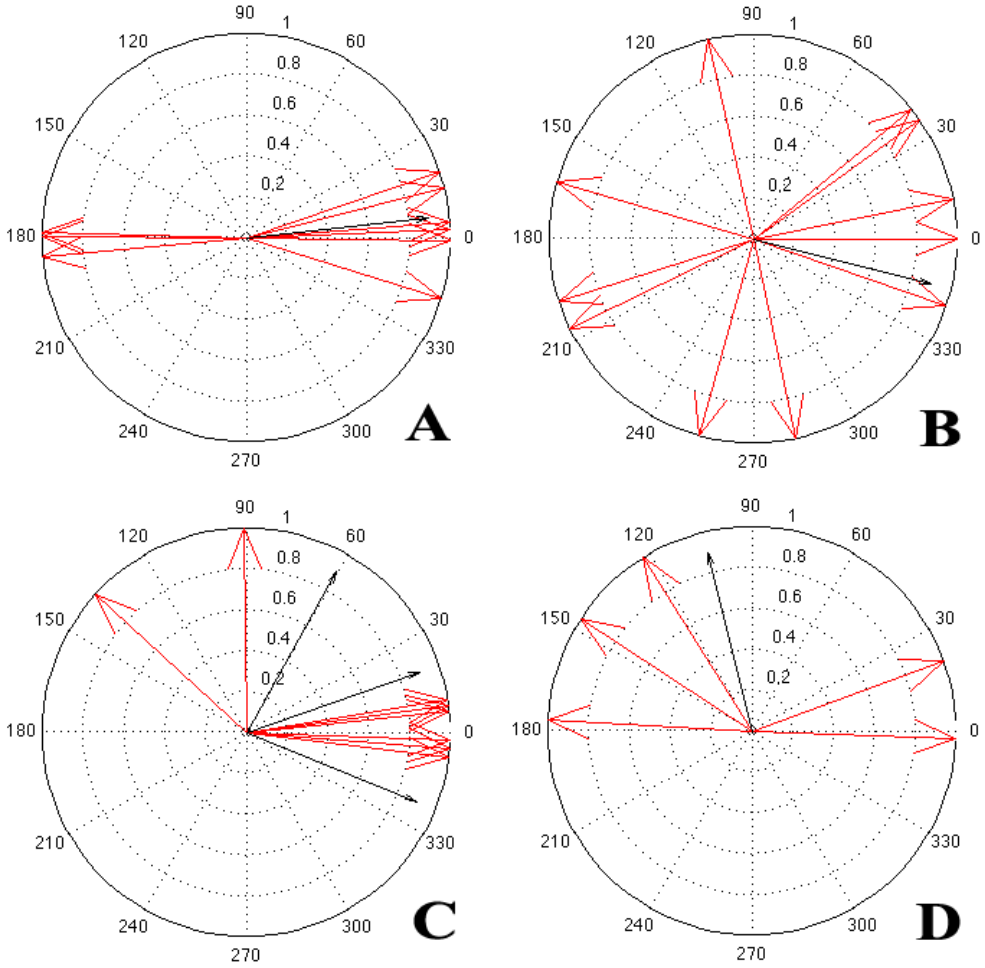

Figure 5.19: Circular histogram of the mean angle differences between axon curvature change ($C_{+/+} - C_{-/-}$) and the gradient across the image. Each red arrow represents a different DiI sample, the black arrows represent the mean and 95% confidence interval. After applying the Rayleigh test for significant difference from a uniform distribution, only $Slit1^{+/+}; Slit2^{+/-}$ (C) was significant at the 5% level (p=0.017). A: $Slit1^{+/-}; Slit2^{+/+}$, B: $Slit1^{-/-}; Slit2^{+/+}$, C: $Slit1^{+/+}; Slit2^{+/-}$, D: $Slit1^{+/+}; Slit2^{-/-}$.

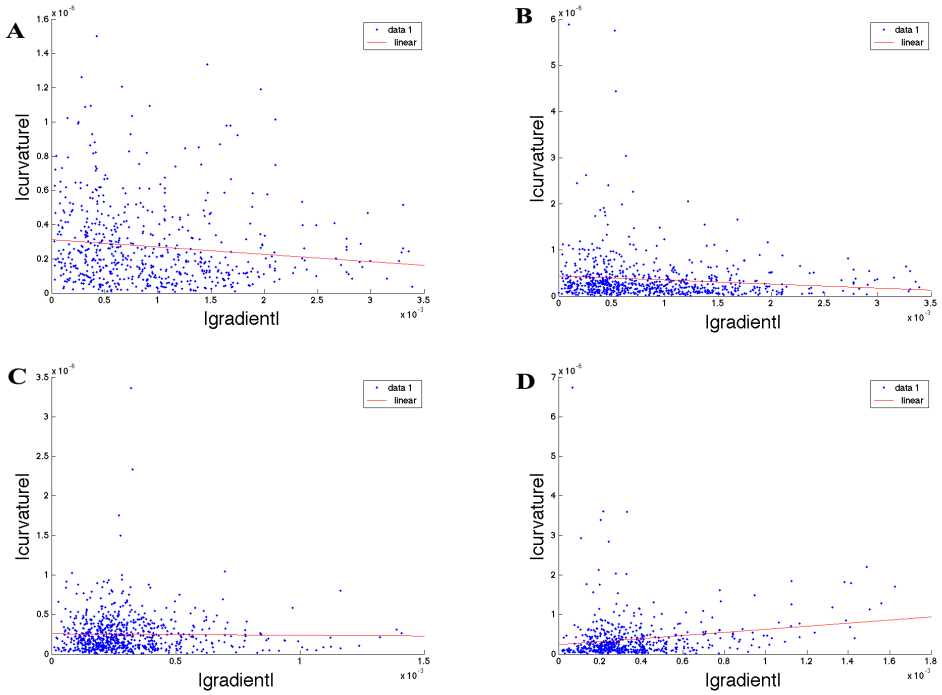

Figure 5.20: These figures compare the magnitude of the mRNA gradient with the magnitude of the curvature differences across the optic chiasm. In no case is the predicted proportional relationship seen. A: $Slit1^{+/-}; Slit2^{+/+}$, B: $Slit1^{-/-}; Slit2^{+/+}$, C: $Slit1^{+/+}; Slit2^{+/-}$, D: $Slit1^{+/+}; Slit2^{-/-}$.

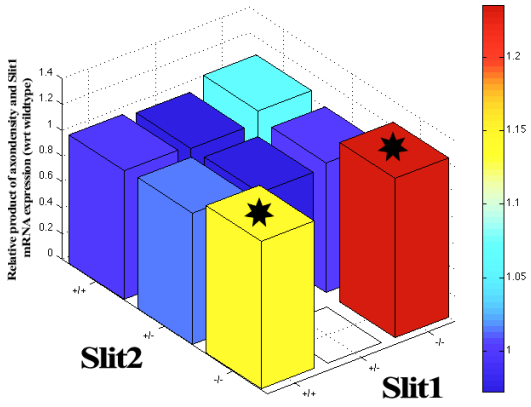

Figure 5.21: The relative product of axon number and Slit1 with respect to wildtype. It seems the same percentage of axons enter the Slit1 region in both the wildtype and mutants. $Slit1^{+/+};Slit2^{-/-}$ significantly higher than wildtype at the 5% level (p = 0.02), $Slit1^{-/-};Slit2^{-/-}$ significantly higher than wt at the 1 % level (p = 0.003).

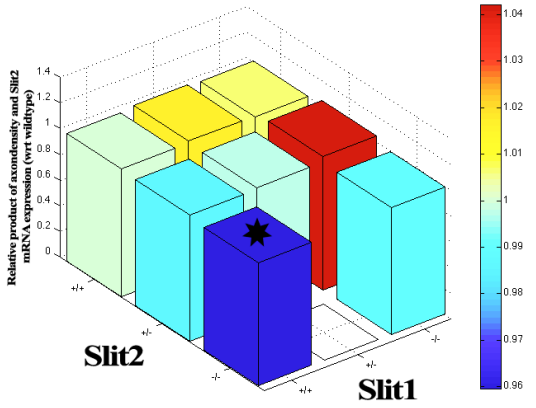

Figure 5.22: The relative product of axon number and Slit2 with respect to wildtype. It seems the same percentage of axons enter the Slit2 region in both the wildtype and mutants. $Slit1^{+/+};Slit2^{-/-}$ significantly lower than wildtype at the 1 % level (p = 0.008).

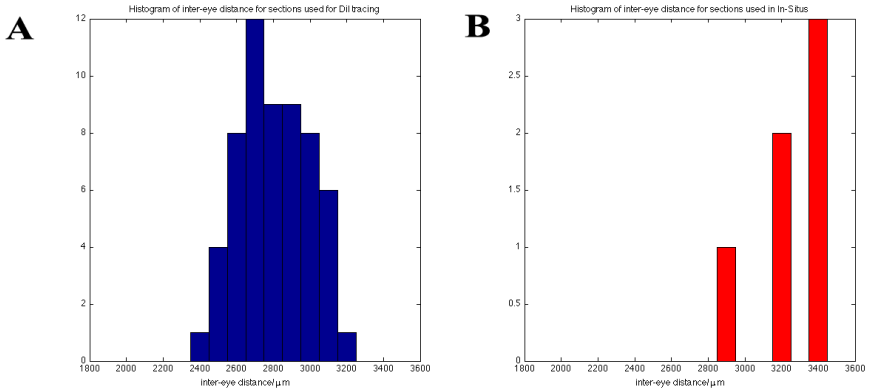

Figure 5.23: Histograms of inter-eye distance for DiI data (left) and In Situ data (right). It appears that for the In Situ data the typical head size is slightly larger than for the DiI samples.

Chapter 6

Conclusions

In this chapter the findings of this thesis are brought together. I give a brief summary of the overall conclusions as well as the future direction this work can be continued in.

6.1 Thesis Summary

This thesis has demonstrated the first spatial quantification of axon trajectories and significance testing for the localisation of these changes in terms of axon density and axon orientation. By using 2nd derivative Gaussian steerable filters, a method has been tailored to measure the axon directions and curvatures automatically from a static image. This method is universal and can be applied to extracting these quantities from any static image of axon trajectories. In addition a method was developed to align multiple samples onto a universal grid, constrained by landmarks within the tissue.

It was found that there were significant differences in the both the axon density and axon orientations compared to wildtype in the case of $Slit1^{+/+};Slit2^{-/-}$ and $Slit1^{-/-};Slit2^{-/-}$, but no other combination of knockout generated (the knockout $Slit1^{+/-};Slit2^{-/-}$ was not generated) showed statistically significant differences from wildtype. This is the first such quantification of its kind.

The mechanism behind these results was investigated by comparing the mean angular difference between mRNA gradients of Slit1 and Slit2 with the directions and

orientations across the optic chiasm. It appears that in the wildtype on average axon direction and gradient of Slit1 were roughly anti-parallel and the converse was true with respect to Slit2. However this relationship did not appear to be dependent on the embryos genotype.

In addition I looked at the spatial relationship of the gradient/direction and gradient/curvature parity. Again I found sporadic areas of significance, but nothing that could easily be interpreted.

6.2 Discussion

In the previous chapter I showed how it is possible to quantify the mRNA gradient of a guidance cue using colormetric in situ hybridisation and process these images using MATLAB. This gradient was aligned to a universal grid in the same manner that the orientation and curvature vector fields were in the previous section. This enabled the spatial relationship between the gradient to be investigated both in the case of the wildtype and knockouts of Slit1 and Slit2. For the first time it has been possible to take a number of expression patterns representing the gradients of a guidance cue, average and align those images to a universal grid and overlay wildtype/knockout axon orientations and curvatures also averaged from a number of samples. This allows a unique view that was not previously possible and nicely showed that the region axons entered in the Slit2 knockouts was exactly where high Slit2 expression occurred in the wildtype.

The mean directional difference between the gradient and the curvature and orientation was assessed across the image. It was found that there was only significant mean angular difference between the mRNA gradient of Slit2 and the axon direction across the optic chiasm in the wildtype, but no other combination. Somewhat confusingly some of the knockouts showed greater correlation between these variables. This had not been expected given how weak the effect was in wildtype. It is reasonable

to conclude that the metric we were using was perhaps too simple, and that across the chiasm a complex relationship between the mRNA gradients and the axon direction/curvatures is present. One reason for this may be that there are many guidance cues acting at the optic chiasm and that the effect of the slits is small compared to all these other cues and so any relationship that may be present between the gradients and axon directions/curvatures is drowned out. Another point is that this measure is tested for significance from a uniform circular distribution, and given that this is compared with the same gradient for each sample, this is perhaps more a measure of variability within a genotype. This brings into question the validity of combining a number of DiI images separately and then conducting a number of in situs and combining them all at the end. For this reason the significant effects in this measure found in some of the knockouts I believe are down to the lower variability in these genotypes.

Ideally an experiment would be conducted that would measure both the gradient (ideally the protein gradient) and axon trajectories in the same preparation. But this is significantly more complicated that the protocols I have followed so it was important to try the simplest methods first before ruling them out. In any case these computational methods I have developed are universal and can be applied to a wide range of similar problems with little alteration.

I then looked at the spatial relationship between the gradient and curvatures of the axons in terms of their relative directions (parallel, anti-parallel or perpendicular). Although this was useful for visualising interesting spatial differences in the relationship between these vector fields, few significant differences were found between wildtype and knockouts of Slit1 and Slit2, and these differences appeared to occur sporadically across the chiasm.

Next the difference in curvature between wildtype and knockout was calculated. This quantity is indicative of some underlying change in the forces acting on the axons as the result of removing the gradient of a guidance cue. This should overcome the problem of finding a relationship between axon directions/curvatures and mRNA

gradients when multiple guidance cues are acting at the chiasm at once, as this is the difference between wildtype and knockout and therefore the result of a single guidance cue. This curvature difference was compared with the mRNA gradients of Slit1 and Slit2. For the case of the $Slit1^{+/+};Slit2^{-/-}$ and the mRNA gradient of Slit2, the angular difference was deemed significant at the 5% level. However, angular significance was not found for the full knockout of Slit2, although this may have been down to the low n-number (5). Neither of the Slit1 knockouts ($Slit1^{+/-};Slit2^{+/+}$, $Slit1^{-/-};Slit2^{+/+}$) showed significance in the angle between the curvature difference form wildtype and the mRNA gradient of Slit1. However, when the magnitude of the curvature difference vectors and the mRNA gradient vectors were compared, no significance was found in any of the knockouts. This suggests again that the gradient of Slit2 is more important than the gradient of Slit1 and it is the direction of the gradient as opposed to the steepness that plays a more important part in instructing axon navigation.

Although this is an interesting finding, several assumptions were made: I was measuring the mRNA gradient and not the protein gradient, and the gradient and direction/curvature information came from different samples. We were also looking for a simple proportionality relationship and this may be inappropriate and perhaps something more complex is going on for which a more complex mathematical model may be appropriate. Another point to consider is that at no point was the concentration of robo receptors quantified which act to translate the slit code, so it may be the case that different levels of slit expression may be interpreted differently across the chiasm depending of robo expression. This is another key thing that could be measured in the future and included in this analysis.

Finally I looked at the product of relative mRNA expression (absolute levels cannot be obtained from colormetric in situs) and axon density across the chiasm as a percentage of the total axon density. This is in order to test the hypothesis that this metric would be higher in the case of the slit knockouts, as axons are believed to more readily

enter these regions in the absence of slit if it's acting as a repulsive cue. It was found that this metric with respect to Slit1 expression was higher for $Slit1^{+/+};Slit2^{-/-}$ and $Slit1^{-/-};Slit2^{-/-}$ knockouts than for wildtype but that the metric with respect to Slit2 expression for the $Slit1^{-/-};Slit2^{-/-}$ knockout was lower than wildtype. The reason for this counter-intuitive result is perhaps that although more axons enter the (formerly) high regions of Slit2 expression in the double knockout, there is also far more wandering over the whole chiasm (into areas of low Slit2 expression), so as a percentage this actually goes down. No other combination of Slit expression pattern/knockout showed significance. This again gives an interesting and novel overview of the spatial relationship between the slit expression and the axonal coverage of the chiasm.

Going back to the analysis of the Chapter 4, it looks as though the methods developed there have been the most successful. This really shows a powerful demonstration of the algorithm developed in Chapter 3. Both as a visualisation tool for comparing the direction and curvature vector fields, but also as a method that allows for precise comparison between embryos of different genotype. My method has repeated the findings in Plump et al. (2002), but it was originally reported that the $Slit1^{+/+};Slit2^{-/-}$ had no differences from wildtype. However, in this study I have shown statistically that there is a shift in the position of the optic chiasm. The reason this was perhaps not reported initially was because a universal grid was not used. However, in this study I did not observe an ectopic chiasm in the manner that was observed in the original paper (Plump et al., 2002). The reason for this may be related to my use of thick vibratome sections as opposed to using whole mounts. In any case there is still further investigation needed in order to fully understand slit-mediated axon guidance at the mouse optic chiasm.

Perhaps one of the weaknesses of the algorithm is its failure to detect a difference between the $Slit1^{+/+}Slit2^{-/-}$ and the $Slit1^{-/-}Slit2^{-/-}$ phenotypes. This does not appear to be a problem with the tracing part of the algorithm, as from visual inspection the tracing appeared to have taken place successfully. This may instead be to do with

the FDR method, which may be too stringent and removed some true positives. Additionally there may be a more sophisticated way in which to compare the vector fields from two different sets of samples.

The conclusion that Slit2 that plays a bigger role in guiding axons at the mouse optic chiasm than Slit1 is echoed in Conway et al. (2011) which reports a similar finding in mouse forebrain commissure development.

It is hoped that this method will become a standard tool in the study of axon guidance, in particular it is the first algorithm that can measure and visualise the curvature of the axon trajectories, a currently overlooked property of the axon tract.

6.3 Future Work

The methods developed in this thesis provide an important set of tools for quantifying spatial data in axon guidance that have been tried and tested on an important area of axon guidance. Although the combination of in situ and DiI data was less successful than the direct comparison of the axon directions/curvatures of different genotypes, it was important to see how far I could take this analysis using standard lab protocols. In future it would be desirable to use a method of measuring both axon trajectories and molecular gradients in the same preparation, that also allows accurate quantification. This could be done, for example, by combining LacZ staining with anti-neurofilament immunos, such as those performed in Pratt et al. (2006), although this method stains axons from both eyes, making it impossible to distinguish which eye the axons come from.

Another application of these analytical techniques would be for high-throughput studies where automation is critical. For example an experiment using serial block-face microscopy to image an embryo with endogenously expressed axonal marker such as GFP could be analysed using my method to automatically determine the 2D axonal direction/curvature vector fields and automatically compare these vector fields to high-

light exact areas of statistical differences. Once these areas have been highlighted they could be investigated in much greater depth using more traditional molecular biological techniques.

There is still lots of scope for further research in quantification and phenomenological modelling in axon guidance, what I have demonstrated in this thesis is the feasibility of such methods as well as their analytical power in a model system.

Appendix A

2D Steerable filter code

```
%for no = 50:58

%% Read in actual files...
clear all
no = 32;
structLoadName = '/Users/matthewdown/Documents/MATLAB/Results/ChiasmData.mat'; %location of data info
load(structLoadName);

sample = XO(no).name;
filename = strcat('/Users/matthewdown/Documents/MATLAB/Data/',sample ,'.tif');
%alignfilename = strcat('/Users/matthewdown/Documents/MATLAB/Align/',
%sample, '.mat');  %We'll just use the data from the XO structure!

Alx = XO(no).Alx;   %Alignment Info
Aly = XO(no).Aly;
Pow = XO(no).power;   %Power of lens used for certain Image

info = imfinfo(filename,'tiff');
A = imread(filename);

testfun = double(A)+1;

filtersize = 8.0;   %Filter size in pixels
smoothsize = 130;    %Size of Gaussian smoothing

%% Applies Steerable Filters
```

```
[g0x g0y g0z g1x g1y g1z g2x g2y g2z] = GaussianDerivatives3D(filtersize);

tic

N = 4/(filtersize)^4;
Rxx = -N*conv2(conv2(testfun, g2x, 'same'), g0y, 'same');
Rxy = -N*conv2(conv2(testfun, g1x, 'same'), g1y, 'same');
Ryy = -N*conv2(conv2(testfun, g0x, 'same'), g2y, 'same');

Rg = N*conv2(conv2(testfun, g0x, 'same'), g0y, 'same');
Gmax = 0.5*atan2(2*Rxy,(Ryy-Rxx));
%This is the angle that gives the maximal response from the filter

Rmax = Rxx/2+Ryy/2+(Rxx/2-Ryy/2).*cos(2*Gmax)-Rxy.*sin(2*Gmax);
%This is the value of the maximal response

Rmax = Rmax./Rg;
%Dividing the steerable filter response by the gaussian responee. This calculation is
optional but gives better results often

GX = cos(Gmax); GY = -sin(Gmax);  %negative y-axis due to image 0,0 being top left
clear Rxx Rxy Ryy Rg
toc

%% Applies non-maximum suppression (removes filter responses that aren't on a ridge)
tic
MaxGrid = nms(testfun, Gmax); %Non - maximum suppression

xs = size(testfun, 1); ys = size(testfun, 2);
IT = 2*median(testfun(:));  %Image Threshold
RT = 2*median(Rmax(:));

T = (testfun>IT).*(Rmax>RT).*MaxGrid;
toc;

%% Smooth out data before applying curvature

tic
[GXS GYS TS] = smooth180(Gmax, T, smoothsize);
toc;

%% Calculates Curvature
```

```
C = curl(GXS, GYS);
CX = -GYS.*C; CY = GXS.*C;

%%
Mag = sqrt(CX.^2 + CY.^2);
T = T.*(Mag<0.05);
ind = find(T);
dwnsmpl = 150; %choose downsample level to plot
ind = ind(1:dwnsmpl:end);
[X Y] = meshgrid(1:ys, 1:xs);

imagesc(testfun); hold on; quiver(X(ind), Y(ind), GXS(ind), GYS(ind), 'r');
quiver(X(ind), Y(ind), CX(ind), CY(ind));

title(strcat('sample: ', XO(no).name, ' Slit1: ', XO(no).slit1, ' Slit2 ', XO(no).slit2));

axis off; colormap(gray); axis equal;



%% Only run this code at the very end(!)

savename = strcat('/Users/matthewdown/Documents/MATLAB/Results/smooth method/', sample, '.mat');

X = X(ind); Y = Y(ind); GXS = GXS(ind); GYS = GYS(ind);
CX = CX(ind); CY = CY(ind);

[CX CY GXS GYS X Y] = alignment(X, Y, CX, CY, GXS, GYS, Alx, Aly, Pow);

save(savename, 'X', 'Y', 'GXS', 'GYS', 'CX', 'CY', 'A');

%end
```

Appendix B

Experimental methodology

In this chapter I detail the experimental methods used in the lab.

B.1 Breeding

Knockout mice for the DiI experiments were derived from the same line as used in Plump et al. (2002), the mice were crossed with wildtype C57/Bl6 mice in order to expand the colony. In order to generate high numbers of the double mutant ($Slit1^{-/-}Slit2^{-/-}$), $Slit1^{-/-}Slit2^{+/-}$ mice were crossed with each other. Other embryo genotypes were generated from crossing various intermediate knockouts.

B.2 DiI tract tracing

For the DiI axon tracing, the standard protocol was followed detailed here:

- E13.5 Embryo heads were fixed at 4C in 4% paraformaldehyde in PBS overnight.
- The lens of the right eye was removed and the optic cup was dried using blotting paper before 1,1-dioctadecyl-3,3,3,3-tetramethyl-indocarbocyanine perchlorate (DiI) crystals were packed into the optic cup.

- Heads were returned to 4%paraformaldehyde in PBS in the dark at room temperature for 2/3 weeks to allow tracers to diffuse along axons.

- The heads were then horizontally sectioned at 150μm using a Leica Microsystems (Wetzlar, Germany) vibratome, and mounted in 9:1 glycerol to PBS.

- Images were taken on a Zeiss (Oberkochen, Germany) Axiovert confocal LSM 510 microscope, with a 40X primary objective, utilising the tile scan function to obtain sufficient coverage of the optic chiasm. The 543nm laser was used for excitation and collected the emission was collected from 565-615nm. A maximum intensity projection was then created for further analysis.

- For each section, the corresponding bright-field image was taken both with white light and epifluorescence for alignment purposes.

B.3 Genotyping embryos using PCR

DiI injections were performed as described in the previous section. In addition it was necessary to genotype the animals to determine their genetic background. This was the genotyping protocol I used:

- Tissue lysis: Dilute proteinase K to 200μg/ml in 1 x extraction buffer (10mM Tris pH9, 50mM KCl, 1.5mM MgCl2, 0.1% Triton X 100). Add 100μl per tissue sample.

- Incubate at 55°C in shaking water bath 3hr.

- Proteinase K inactivation: Heat tubes at 95°C, 15min on PCR block. Centrifuge 13,000rpm, 2min. Use $1-2\mu$l for PCR

- Make up 10μM primer mix: 10μl WT F + 10μl WT R +10μl mutant R + 70μl ddH_20, Where:

  - Slit1 WT F = AAG ATG CCT CCT CTG ACT TC
  - Slit 1 WT R = ACC CTT AGC TTC TAC CAA CC
  - Slit 1 mutant R = AGG TTT CTC GAG CGT CAT AG

- Make master mix (Water: 14.3μl, 5x promega green buffer: 4.0μl, Primer mix 10μM: 0.4μl, 10mM dNTPs: 0.2μl, GoTaq $5u/\mu$l: 0.15μl), scale up by the number of samples.

- Add 1-2 μl of lysate to 19μl of master mix and cycle in a PCR machine as follows:

  - 95°C 3min $\times$1
  - 95°C 30s
  - 60°C 40s
  - 72°C 50s $\times$30
  - 72°C 5min

- Run reactant on 1 % mini gel at around 80V

B.4 In Situ hybridisation

In situ protocol was followed as in Erskine et al. (2000).

B.4.1 Alignment and Image analysis

In terms of image alignment and scaling, the same method was used as described in the previous section. The images were post-processed in Adobe Photoshop CS3 using the spot heal tool to remove marks from air bubbles, converted to monochrome, and blurred using the gaussian blur. In order to determine the 2D expression levels, the images were first converted to monochrome and levels of high expression were

defined as being the areas where the intensity of the image was the lowest (i.e. where the colormetic stain blocked light the most). So the images were inverted such that the intensity at each point was converted to the maximum level of expression minus this value (i.e. $I(x,y) \rightarrow I_{\max} - I(x,y)$). As colormetric In Situs are unreliable measures of the absolute levels of mRNA, the peak levels of expression were compared across images and were found to be remarkably similar, further supporting our justification of using this method to determine the gradient.

Appendix C

Overlay of gradients, direction and curvature.

In this appendix I present high resolution images of all the vector fields overlaid on top of one another.

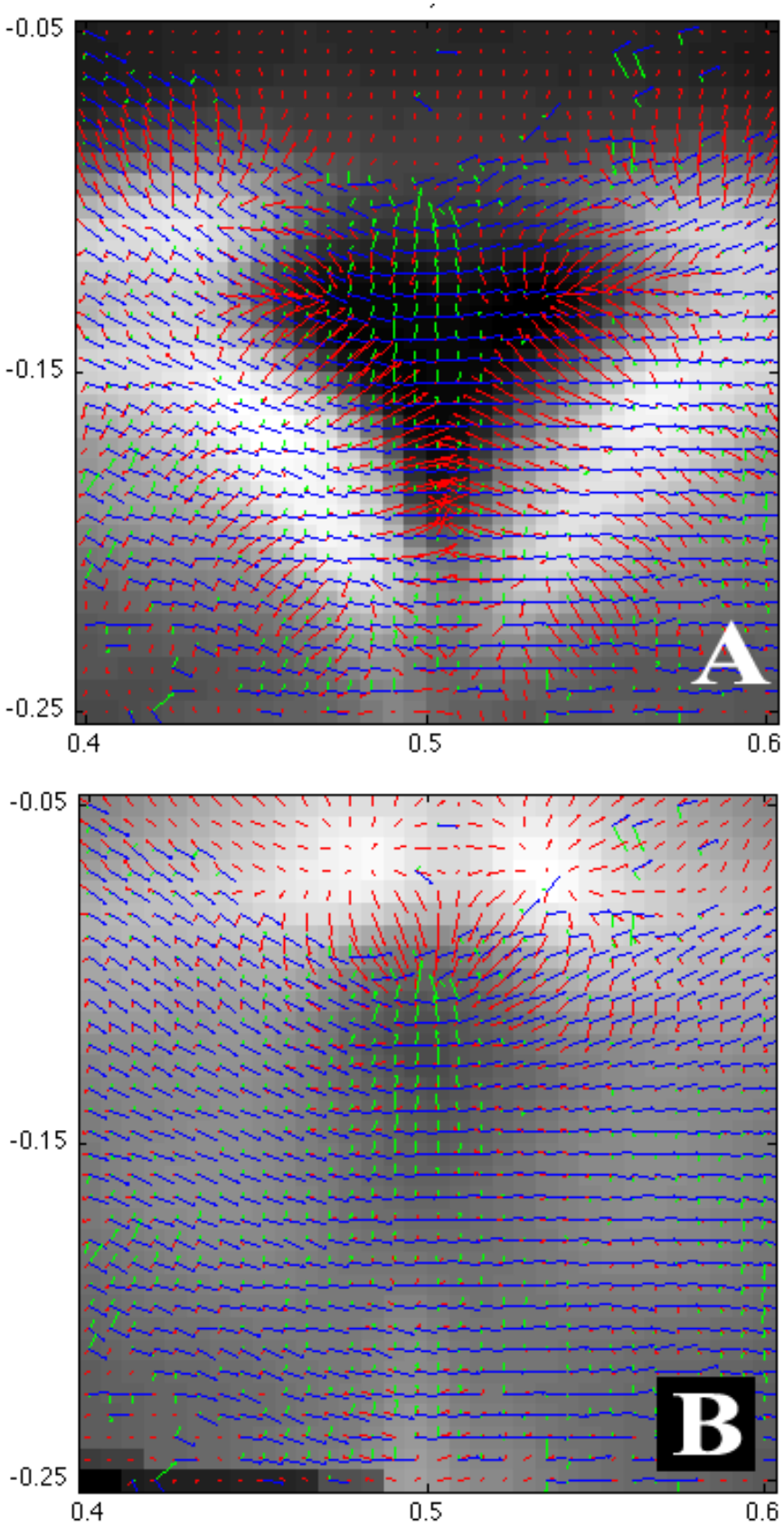

Figure C.1: High res images of the Slit1 +/+ Slit2 +/+ vectors fields overlaid onto the gradient of Slit1 and Slit2 respectively.

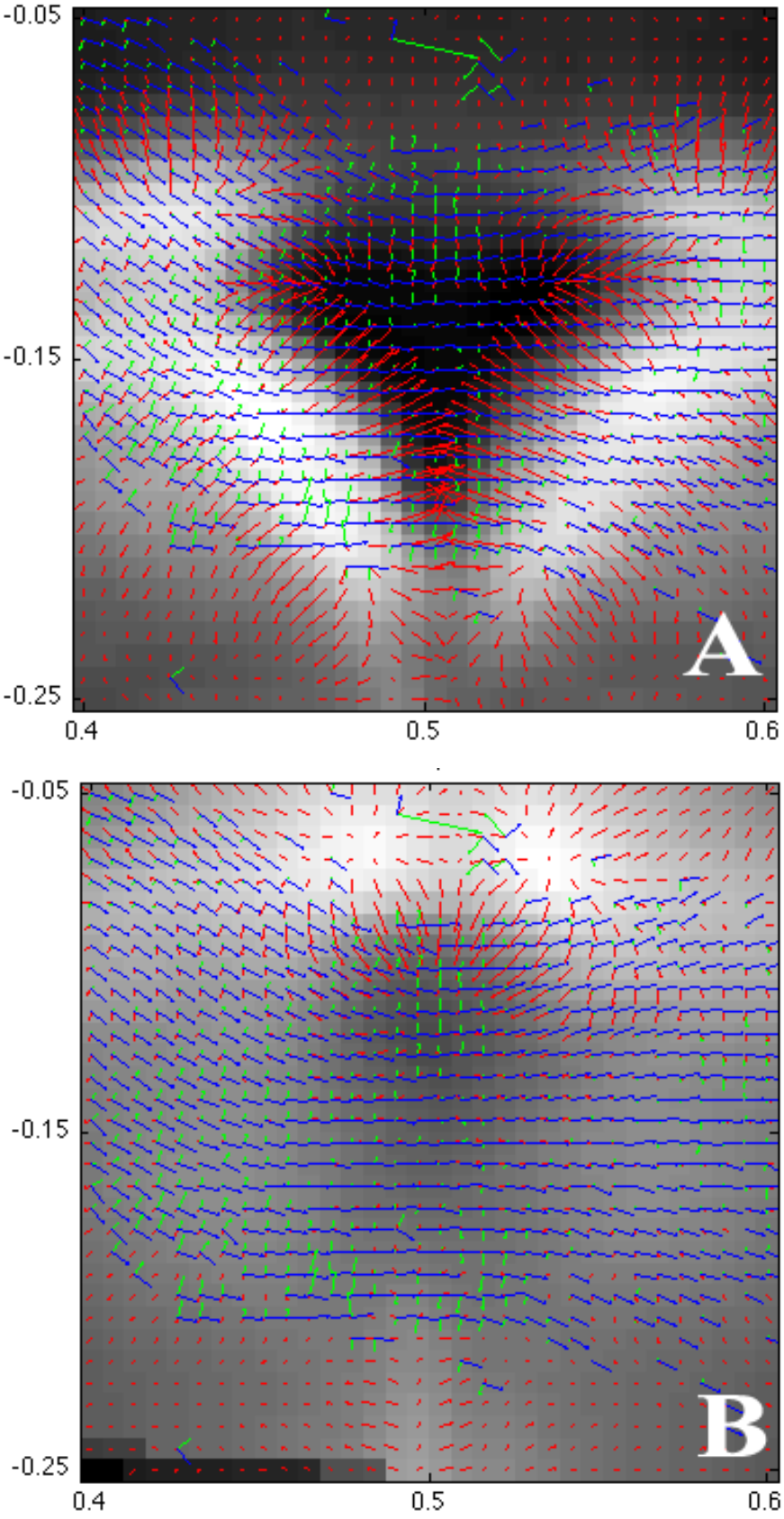

Figure C.2: High res images of the Slit1 +/- Slit2 +/+ vectors fields overlaid onto the gradient of Slit1 and Slit2 respectively.

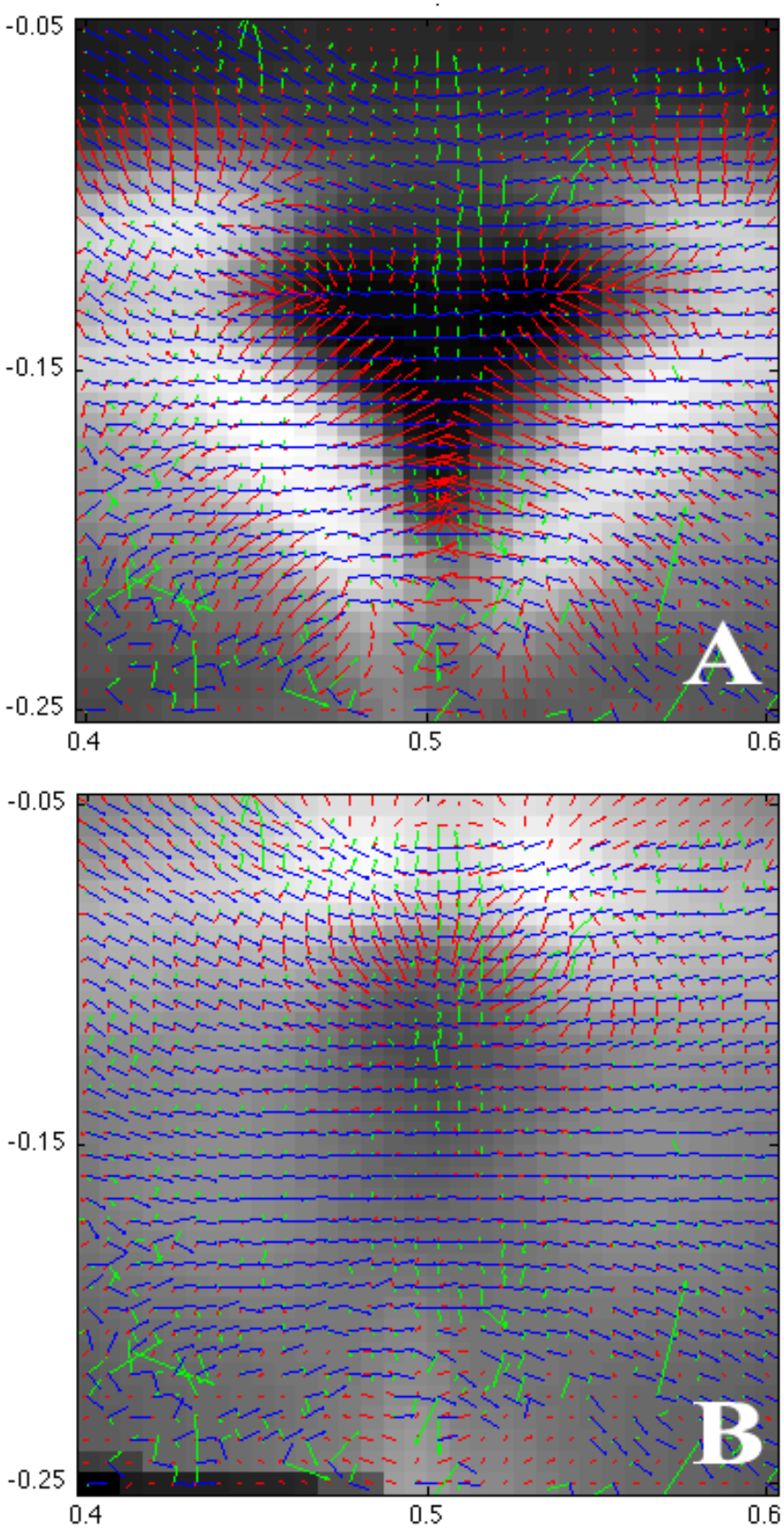

Figure C.3: High res images of the Slit1 -/- Slit2 +/+ vectors fields overlaid onto the gradient of Slit1 and Slit2 respectively.

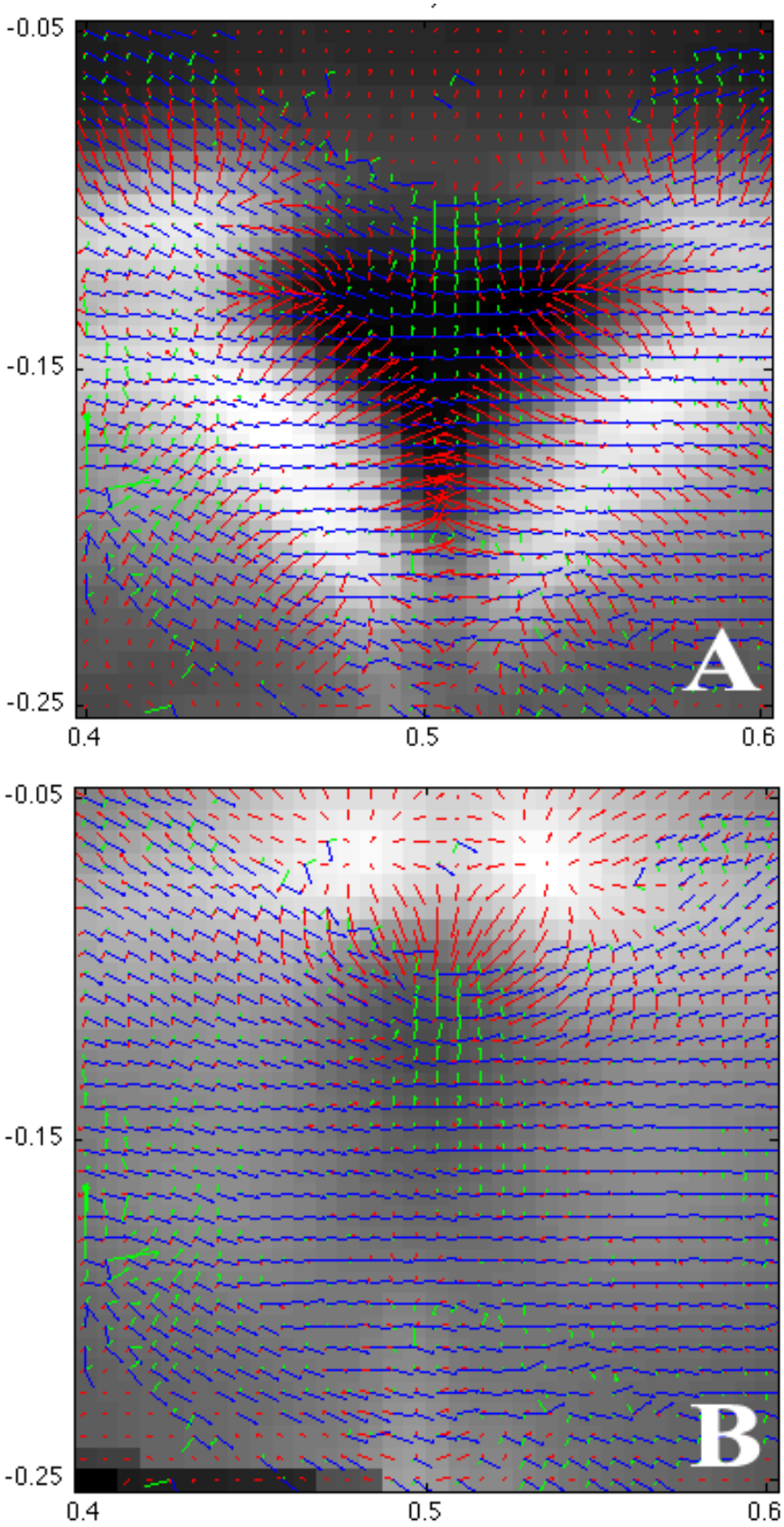

Figure C.4: High res images of the Slit1 +/+ Slit2 +/- vectors fields overlaid onto the gradient of Slit1 and Slit2 respectively.

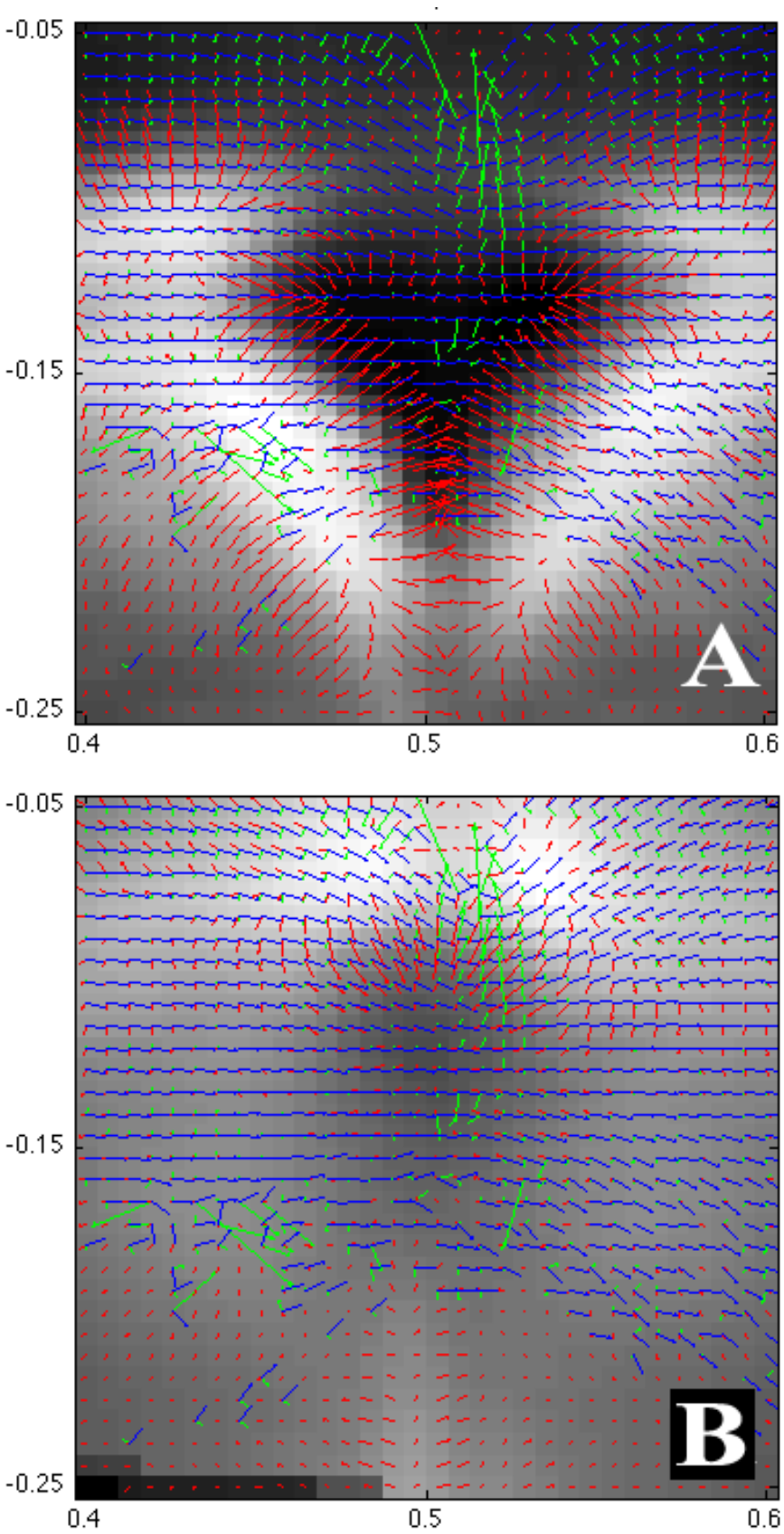

Figure C.5: High res images of the Slit1 +/+ Slit2 -/- vectors fields overlaid onto the gradient of Slit1 and Slit2 respectively.

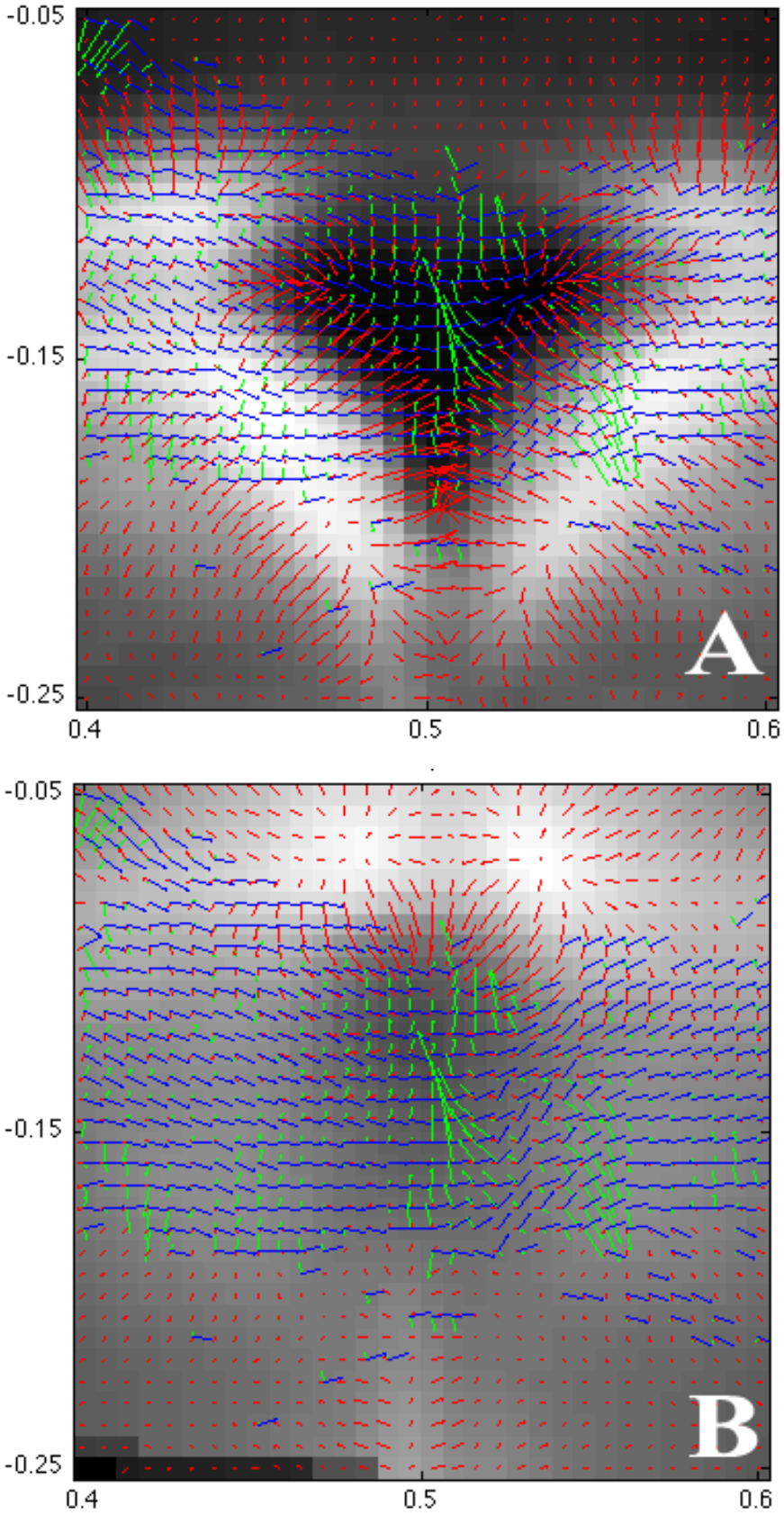

Figure C.6: High res images of the Slit1 +/- Slit2 +/- vectors fields overlaid onto the gradient of Slit1 and Slit2 respectively.

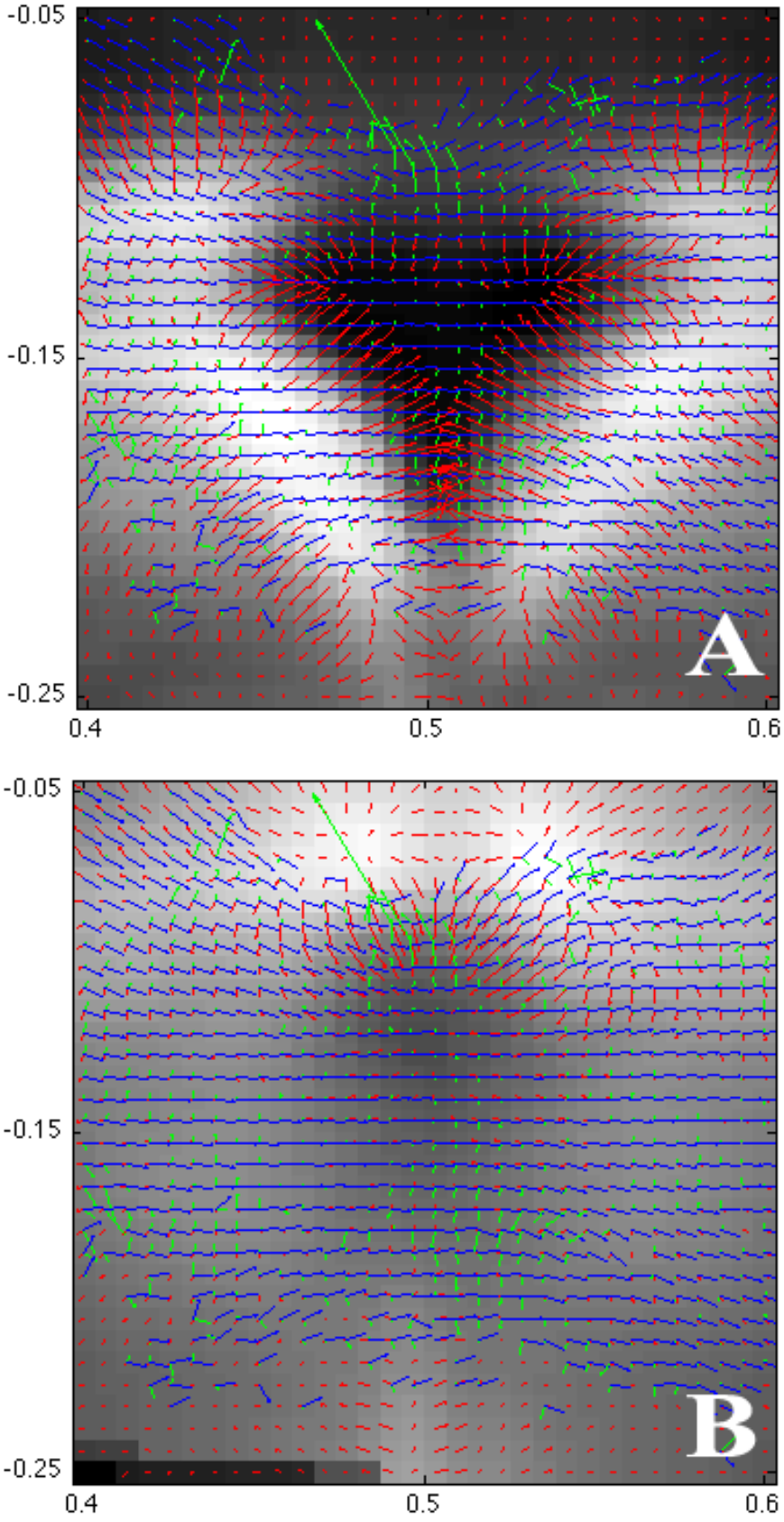

Figure C.7: High res images of the Slit1 -/- Slit2 +/- vectors fields overlaid onto the gradient of Slit1 and Slit2 respectively.

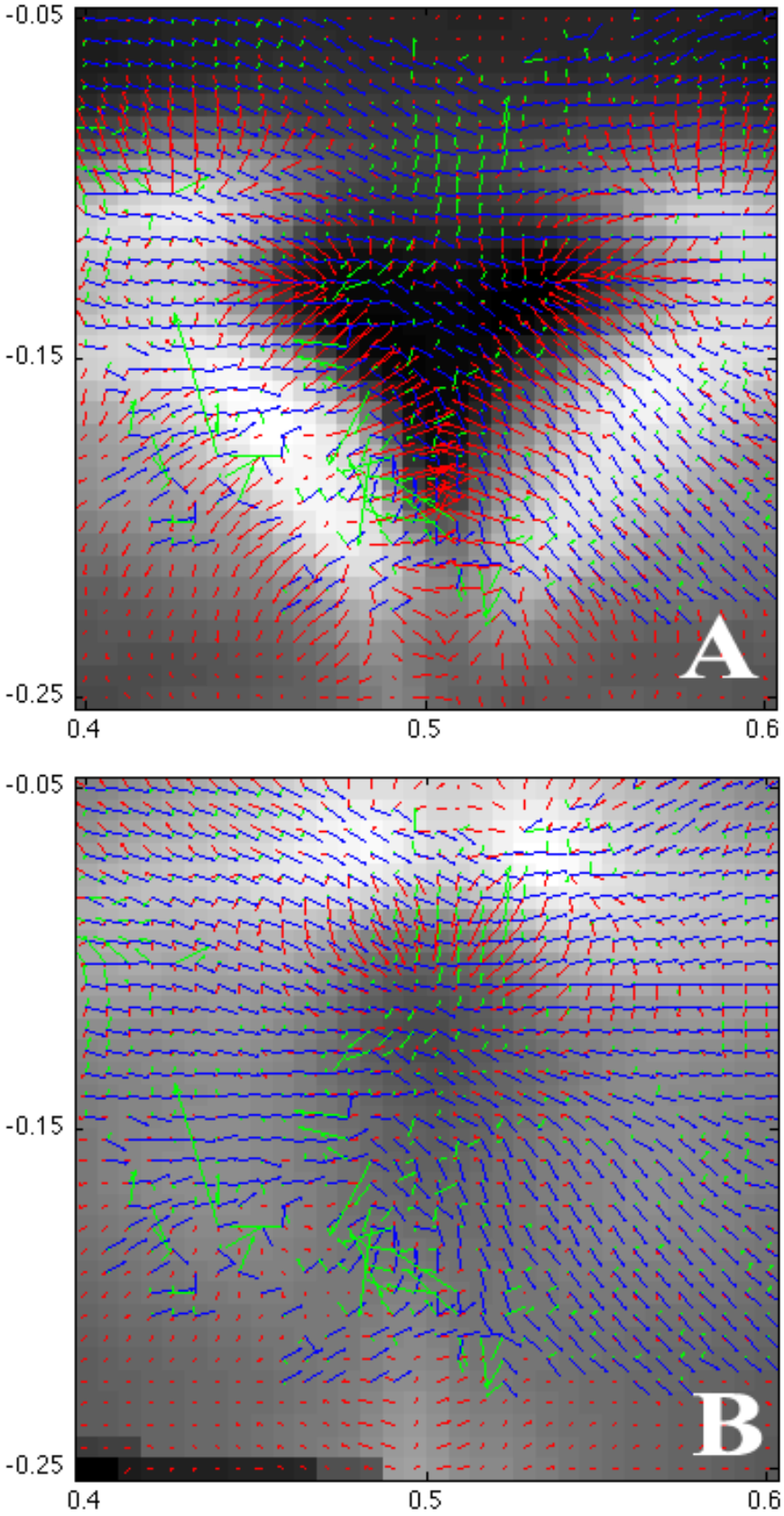

Figure C.8: High res images of the Slit1 -/- Slit2 -/- vectors fields overlaid onto the gradient of Slit1 and Slit2 respectively.

Bibliography

Aguet, F., Jacob, M., and Unser, M. (2005). Three-dimensional feature detection using optimal steerable filters. In *ICIP (2)*, pages 1158–1161.

Bao, Z.-Z. (2008). Intraretinal projection of retinal ganglion cell axons as a model system for studying axon navigation. *Brain Res*, 1192:165–77.

Benjamini, Y. and Hochberg, Y. (1995). Controlling the false discovery rate - a practical and powerful approach to multiple testing. *Journal of the Royal Statistical Society Series B-Methodological*, 57(1):289–300.

Berg, H. C. and Purcell, E. M. (1977). Physics of chemoreception. *Biophys J*, 20(2):193–219.

Buettner, H. (1995). Computer-simulation of nerve growth cone filopodial dynamics for visualization and analysis. *Cell Motility and the Cytoskeleton*, 32:187–204.

Butler, S. J. and Tear, G. (2007). Getting axons onto the right path: the role of transcription factors in axon guidance. *Development*, 134(3):439–48.

Charron, F., Stein, E., Jeong, J., McMahon, A. P., and Tessier-Lavigne, M. (2003). The morphogen sonic hedgehog is an axonal chemoattractant that collaborates with netrin-1 in midline axon guidance. *Cell*, 113(1):11–23.

Conway, C. D., Howe, K. M., Nettleton, N. K., Price, D. J., Mason, J. O., and Pratt, T. (2011). Heparan sulfate sugar modifications mediate the functions of slits and

other factors needed for mouse forebrain commissure development. *J Neurosci*, 31(6):1955–70.

Deiner, M. S., Kennedy, T. E., Fazeli, A., Serafini, T., Tessier-Lavigne, M., and Sretavan, D. W. (1997). Netrin-1 and dcc mediate axon guidance locally at the optic disc: loss of function leads to optic nerve hypoplasia. *Neuron*, 19(3):575–89.

Dickson, B. J. (2002). Molecular mechanisms of axon guidance. *Science*, 298(5600):1959–1964.

Down, M. (2007). The role of the gradient of heparan sulphate 6 sulphotransferase 1 (hs6st1) in the guidance of contralateral retinal ganglion cell projections in the mouse optic chiasm. Msc neuroinformatics, University of Edinburgh, 5 Forrest Hill, Edinburgh, EH1 2QL.

Dräger, U. C. (1985). Birth dates of retinal ganglion cells giving rise to the crossed and uncrossed optic projections in the mouse. *Proc R Soc Lond B Biol Sci*, 224(1234):57–77.

Dunlop, S. A., Tee, L. B., Lund, R. D., and Beazley, L. D. (1997). Development of primary visual projections occurs entirely postnatally in the fat-tailed dunnart, a marsupial mouse, sminthopsis crassicaudata. *J Comp Neurol*, 384(1):26–40.

Dunn, O. (1961). Multiple comparisons among means. *Journal of the American Statistical Association*, 56(293):52–&.

Erskine, L. and Herrera, E. (2007). The retinal ganglion cell axon's journey: Insights into molecular mechanisms of axon guidance. *Dev Biol*, 308(1):1–14.

Erskine, L., Williams, S. E., Brose, K., Kidd, T., Rachel, R. A., Goodman, C. S., Tessier-Lavigne, M., and Mason, C. A. (2000). Retinal ganglion cell axon guidance in the mouse optic chiasm: expression and function of robos and slits. *J Neurosci*, 20(13):4975–4982.

Fan, X., Labrador, J. P., Hing, H., and Bashaw, G. J. (2003). Slit stimulation recruits dock and pak to the roundabout receptor and increases rac activity to regulate axon repulsion at the cns midline. *Neuron*, 40(1):113–27.

Freeman, W. T. and Adelson, E. H. (1991). The design and use of steerable filters. *IEEE Trans. Pattern Anal. Mach. Intell.*, 13(9):891–906.

Gabor, D. (1946). Theory of communication. *J. Inst. Electr. Eng. 24, 891-910*.

Godement, P., Wang, L. C., and Mason, C. A. (1994). Retinal axon divergence in the optic chiasm: dynamics of growth cone behavior at the midline. *J Neurosci*, 14(11 Pt 2):7024–39.

Goodhill, G. J. (1997). Diffusion in axon guidance. *Eur J Neurosci*, 9(7):1414–1421.

Goodhill, G. J. (2003). A theoretical model of axon guidance by the robo code. *Neural Comput*, 15(3):549–64.

Goodhill, G. J., Gu, M., and Urbach, J. S. (2004). Predicting axonal response to molecular gradients with a computational model of filopodial dynamics. *Neural Comput*, 16(11):2221–43.

Goodhill, G. J. and Urbach, J. S. (1999). Theoretical analysis of gradient detection by growth cones. *J Neurobiol*, 41(2):230–41.

Guo-Hua Li, C.-D. Q. and Wang, L.-W. (1995). Computer model of growth cone behavior and neuronal morphogenesis. *Journal of Theoretical Biology*, 174:381–389.

Hochberg, Y. and Tamhane, A. C. (1987). *Multiple comparison procedures*. John Wiley & Sons, Inc.

Holt, C. E. and Dickson, B. J. (2005). Sugar codes for axons? *Neuron*, 46(2):169–172.

Inatani, M., Irie, F., Plump, A. S., Tessier-Lavigne, M., and Yamaguchi, Y. (2003). Mammalian brain morphogenesis and midline axon guidance require heparan sulfate. *Science*, 302(5647):1044–1046.

Kidd, T., Bland, K. S., and Goodman, C. S. (1999). Slit is the midline repellent for the robo receptor in drosophila. *Cell*, 96(6):785–94.

Kolpak, A., Zhang, J., and Bao, Z.-Z. (2005). Sonic hedgehog has a dual effect on the growth of retinal ganglion axons depending on its concentration. *J Neurosci*, 25(13):3432–3441.

Krottje, J. K. and van Ooyen, A. (2007). A mathematical framework for modeling axon guidance. *Bulletin of Mathematical Biology*, 69:3–31.

Mason, C. and Erskine, L. (2000). Growth cone form, behavior, and interactions in vivo: retinal axon pathfinding as a model. *J Neurobiol*, 44(2):260–70.

Mason, C. A. and Wang, L. C. (1997). Growth cone form is behavior-specific and, consequently, position-specific along the retinal axon pathway. *J Neurosci*, 17(3):1086–100.

Ming, G., Song, H., Berninger, B., Inagaki, N., Tessier-Lavigne, M., and Poo, M. (1999). Phospholipase c-gamma and phosphoinositide 3-kinase mediate cytoplasmic signaling in nerve growth cone guidance. *Neuron*, 23(1):139–48.

Morlot, C., Thielens, N. M., Ravelli, R. B. G., Hemrika, W., Romijn, R. A., Gros, P., Cusack, S., and McCarthy, A. A. (2007). Structural insights into the Slit-robo complex. *Proc Natl Acad Sci U S A*, 104(38):14923–8.

Mortimer, D., Feldner, J., Vaughan, T., Vetter, I., Pujic, Z., Rosoff, W. J., Burrage, K., Dayan, P., Richards, L. J., and Goodhill, G. J. (2009). Bayesian model predicts the response of axons to molecular gradients. *Proc Natl Acad Sci U S A*, 106(25):10296–301.

Mortimer, D., Pujic, Z., Vaughan, T., Thompson, A. W., Feldner, J., Vetter, I., and Goodhill, G. J. (2010). Axon guidance by growth-rate modulation. *Proc Natl Acad Sci U S A*, 107(11):5202–7.

Oster, S. F., Bodeker, M. O., He, F., and Sretavan, D. W. (2003). Invariant sema5a inhibition serves an ensheathing function during optic nerve development. *Development*, 130(4):775–784.

Plas, D. T., Lopez, J. E., and Crair, M. C. (2005). Pretarget sorting of retinocollicular axons in the mouse. *J Comp Neurol*, 491(4):305–19.

Plump, A. S., Erskine, L., Sabatier, C., Brose, K., Epstein, C. J., Goodman, C. S., Mason, C. A., and Tessier-Lavigne, M. (2002). Slit1 and slit2 cooperate to prevent premature midline crossing of retinal axons in the mouse visual system. *Neuron*, 33(2):219–232.

Pratt, T., Conway, C. D., Tian, N. M. M.-L., Price, D. J., and Mason, J. O. (2006). Heparan sulphation patterns generated by specific heparan sulfotransferase enzymes direct distinct aspects of retinal axon guidance at the optic chiasm. *J Neurosci*, 26(26):6911–6923.

Pratt, T., Tian, N. M. M.-L., Simpson, T. I., Mason, J. O., and Price, D. J. (2004). The winged helix transcription factor foxg1 facilitates retinal ganglion cell axon crossing of the ventral midline in the mouse. *Development*, 131(15):3773–3784.

Pujic, Z., Giacomantonio, C. E., Unni, D., Rosoff, W. J., and Goodhill, G. J. (2008). Analysis of the growth cone turning assay for studying axon guidance. *J Neurosci Methods*, 170(2):220–8.

Robinson, S. R. and Dreher, B. (1990). The visual pathways of eutherian mammals and marsupials develop according to a common timetable. *Brain Behav Evol*, 36(4):177–95.

Rosoff, W. J., Urbach, J. S., Esrick, M. A., McAllister, R. G., Richards, L. J., and Goodhill, G. J. (2004). A new chemotaxis assay shows the extreme sensitivity of axons to molecular gradients. *Nat Neurosci*, 7(6):678–82.

Rothberg, J. M. and Artavanis-Tsakonas, S. (1992). Modularity of the slit protein. characterization of a conserved carboxy-terminal sequence in secreted proteins and a motif implicated in extracellular protein interactions. *J Mol Biol*, 227(2):367–70.

Rothberg, J. M., Hartley, D. A., Walther, Z., and Artavanis-Tsakonas, S. (1988). slit: an egf-homologous locus of d. melanogaster involved in the development of the embryonic central nervous system. *Cell*, 55(6):1047–59.

Sakai, J. A. and Halloran, M. C. (2006). Semaphorin 3d guides laterality of retinal ganglion cell projections in zebrafish. *Development*, 133(6):1035–1044.

Seeger, M., Tear, G., Ferres-Marco, D., and Goodman, C. S. (1993). Mutations affecting growth cone guidance in drosophila: genes necessary for guidance toward or away from the midline. *Neuron*, 10(3):409–26.

Sretavan, D. W. and Reichardt, L. F. (1993). Time-lapse video analysis of retinal ganglion cell axon pathfinding at the mammalian optic chiasm: growth cone guidance using intrinsic chiasm cues. *Neuron*, 10(4):761–77.

Thompson, H., Andrews, W., Parnavelas, J. G., and Erskine, L. (2009). Robo2 is required for slit-mediated intraretinal axon guidance. *Dev Biol*, 335(2):418–26.

Torres, M., Gomez-Pardo, E., and Gruss, P. (1996). Pax2 contributes to inner ear patterning and optic nerve trajectory. *Development*, 122(11):3381–3391.

Trousse, F., Marti, E., Gruss, P., Torres, M., and Bovolenta, P. (2001). Control of retinal ganglion cell axon growth: a new role for sonic hedgehog. *Development*, 128(20):3927–3936.

Van Veen, M. P. and Van Pelt, J. (1994). Neuritic growth rate described by modeling microtubule dynamics. *Bull Math Biol*, 56(2):249–73.

Wen, Z. and Zheng, J. Q. (2006). Directional guidance of nerve growth cones. *Curr Opin Neurobiol*, 16(1):52–58.

Williams, S. E., Grumet, M., Colman, D. R., Henkemeyer, M., Mason, C. A., and Sakurai, T. (2006). A role for nr-cam in the patterning of binocular visual pathways. *Neuron*, 50(4):535–547.

Williams, S. E., Mann, F., Erskine, L., Sakurai, T., Wei, S., Rossi, D. J., Gale, N. W., Holt, C. E., Mason, C. A., and Henkemeyer, M. (2003). Ephrin-b2 and ephb1 mediate retinal axon divergence at the optic chiasm. *Neuron*, 39(6):919–935.

Ypsilanti, A. R., Zagar, Y., and Chédotal, A. (2010). Moving away from the midline: new developments for slit and robo. *Development*, 137(12):1939–52.